UNIVERSITY OF CALIFORNIA, SAN DIEGO

Geodetic Imaging of the Earthquake Cycle

A dissertation submitted in partial satisfaction of the
requirements for the degree
Doctor of Philosophy

in

Earth Sciences

by

Xiaopeng Tong

Committee in charge:

David T. Sandwell, Chair
Yehuda Bock
Kevin Brown
Yuri Fialko
Xanthippi Markenscoff
Peter Shearer

2013

Copyright
Xiaopeng Tong, 2013
All rights reserved.

The dissertation of Xiaopeng Tong is approved, and it is acceptable in quality and form for publication on microfilm and electronically:

_____

_____

_____

_____

_____

_____
Chair

University of California, San Diego

2013

DEDICATION

EPIGRAPH

TABLE OF CONTENTS

LIST OF FIGURES

LIST OF TABLES

ACKNOWLEDGEMENTS

VITA

2007	Bachelor of Science, Geophysics, Peking University, Beijing, China
2008-2013	Research Assistant, Scripps Institution of Oceanography, University of California, San Diego, U.S.A.
2009	Teaching Assistant, Scripps Institution of Oceanography, University of California, San Diego, U.S.A.
2013	Doctor of Philosophy, Geophysics, Scripps Institution of Oceanography, University of California, San Diego, U.S.A.

PUBLICATIONS

Tong, X., D. Sandwell and B. Smith-Konter, "High resolution interseismic velocity data along the San Andreas fault from GPS and InSAR", *Journal of Geophysical Research*, 118, doi:10.1029/2012JB009442, 2013

Kaneko, Y., Y. Fialko, D. T. Sandwell, **X. Tong**, and M. Furuya, "Interseismic deformation and creep along the central section of the North Anatolian fault (Turkey): InSAR observations and implications for rate-and-state friction properties", *Journal of Geophysical Research*, doi:10.1029/2012JB009661, 2013

Sandwell, D., R. Mellors, **X. Tong**, M. Wei and P. Wessel, "Open radar interferometry software for mapping surface deformation" , *Eos Trans. AGU*, 92(28), doi:10.1029/2011EO280002, 2011

Luttrell, K., **X. Tong**, D. Sandwell, B. Brooks, and M. Bevis, "Estimates of stress drop and crustal tectonic stress from the 27 February 2010 Maule, Chile, earthquake: Implications for fault strength", *Journal of Geophysical Research*, v.116, B11401, 13 PP., doi:10.1029/2011JB008509, 2011

Pollitz, F., B. Brooks, **X. Tong**, M. G. Bevis, J. H. Foster, R. Brgmann, R. Smalley Jr., C. Vigny, A. Socquet, J.-C. Ruegg, J. C. S. Barrientos, H. Parra, J. C. Baez Soto, S. Cimbaro, and M. Blanco, "Coseismic slip distribution of the February 27, 2010 Mw 8.8 Maule, Chile earthquake", *Geophysical Research Lettters*, v.38, L09309, doi:10.1029/2011GL047065, 2011

Lorito, S., F. Romano, S. Atzori, **X. Tong**, A. Avallone, J. McCloskey, M. Cocco, E. Boschi and A. Piatanesi, "Limited overlap between the seismic gap and coseismic slip of the great 2010 Chile earthquake", *Nature Geoscience*, 4, 173-177, doi:10.1038/ngeo1073, 2011

Tong, X., D. Sandwell, K. Luttrell, B. Brooks, M. Bevis, M. Shimada, J. Foster, R. Smalley Jr., H. Parra, J. C. Bez Soto, M. Blanco, E. Kendrick, J. Genrich, and D. J. Caccamise II, "The 2010 Maule, Chile earthquake: Downdip rupture limit revealed by space geodesy", *Geophysical Research Letters*, v.37, L24311, doi:10.1029/2010GL045805, 2010

Tong, X., D. T. Sandwell, Y. Fialko, "Coseismic slip model of the 2008 Wenchuan earthquake derived from joint inversion of InSAR, GPS and field data", *Journal of Geophysical Research*, v.115, B04314, doi:10.1029/2009JB006625, 2010

ABSTRACT OF THE DISSERTATION

Geodetic Imaging of the Earthquake Cycle

by

Xiaopeng Tong

Doctor of Philosophy in Earth Sciences

University of California, San Diego, 2013

David T. Sandwell, Chair

In this dissertation I use Interferometric Synthetic Aperture Radar (InSAR) and Global Positioning System (GPS) to recover cm-level crustal deformation caused by earthquake cycle processes. The studied areas span three different types of tectonic boundaries: a continental thrust earthquake (M7.9 Wenchuan, China) at the eastern margin of the Tibet plateau, a mega-thrust earthquake (M8.8 Maule, Chile) at the Chile subduction zone, and the inter-seismic deformation of the San Andreas Fault System (SAF). A new L-band radar onboard a Japanese satellite ALOS allows us to image high-resolution surface deformation in vegetated areas, which is not possible with older C-band radar systems. In particular, both the Wenchuan and Maule InSAR analyses involved L-band ScanSAR interferometry which had not been attempted prior to this research. Moreover by contributing

to the construction of a new InSAR processing software GMTSAR, I was able to optimize the code for my applications. Automatic processing programs are developed to integrate a large InSAR dataset with a dense GPS network over the entire SAF. The integration approach features combining the long-wavelength deformation from GPS with the short-wavelength deformation from InSAR through a physical model.

The recovered fine-scale surface deformation from InSAR and GPS lead us to better understand the underlying earthquake cycle processes. The geodetic slip inversion reveals that the Wenchuan earthquake occurred on two parallel thrust faults with an imbricate geometry. The co-seismic deformation is dominated by thrust on the shallow-dipping fault then changed to right-lateral strike-slip motion northward. The fault slip of the Wenchuan earthquake is maximum near the surface and decreases with depth. The co-seismic slip model of the Maule earthquake constrains the down-dip extent of the fault slip to be at 45 km depth, similar to the Moho. This model resolves accurately the spatial distribution of high-slip areas, so called "asperity", which can be compared to the spatial pattern of the inter-seismic coupling. In constructing the viscoelastic earthquake cycle model of the SAF, the InSAR observation put tighter constraints on the creep rates of the creeping section of SAF and the faults in northern California. In particular the creeping section is found to be slipping slower than the long-term slip rate by a few mm/yr. This high-resolution deformation model will refine the moment accumulation rates and shear strain rates along the creeping faults, which are not well resolved by previous models using GPS alone.

Chapter 1

Introduction

Plate tectonic is an extremely successful theory to describe the motions of the plates over the surface of the Earth. Far from the plate boundaries the motions are steady and well described by a uniform velocity vector. However, the edges of the plates sometimes undergo stick-slip motions which are responsible for earthquakes. Most earthquakes are small, non-destructive and can be treated as point sources of seismic radiation. Major earthquakes occur much less frequently but they are responsible for most of the seismic energy release and seismic hazard. For those large earthquakes a point source description is no longer adequate. A proper understanding of these events requires careful characterizing their geometric, kinematic and dynamic properties with both seismic and geodetic constraints.

Seismic moment quantifies the energy release of an earthquake. It is defined as $M = \mu s A$, where μ is the shear modulus of the rock material, s is the average slip of the earthquake, A is the average area of the fault plane where the slip occurred (Figure 1.1). Similarly seismic moment accumulation rate quantifies the increasing earthquake potential of a fault. It is defined as $\dot{M} = \mu v d$, where $\dot{M}$ is the seismic moment accumulation rate per unit length of the fault, v is the long term slip rate of the fault, d is the locking depth of the fault. The locking depth d controls the cross sectional area of the zone of elastic energy accumulation, and it generally extends from the earth surface down to 10 to 20 km depth, confined by the brittle part of the plate. The seismic potential of a major earthquake is approximately evaluated as $\dot{M}t$, where t the time elapsed since the last major event

(Figure 1.1).

Faults come in three types: normal, thrust, and strike-slip. In this dissertation I use tools of space geodesy, in particular, Global Positioning System (GPS) and Interferometric Synthetic Aperture Radar (InSAR) to measure seismic moment release of the thrust faults (both continental thrust and mega-thrust at subduction zone) and moment accumulation of a strike-slip fault.

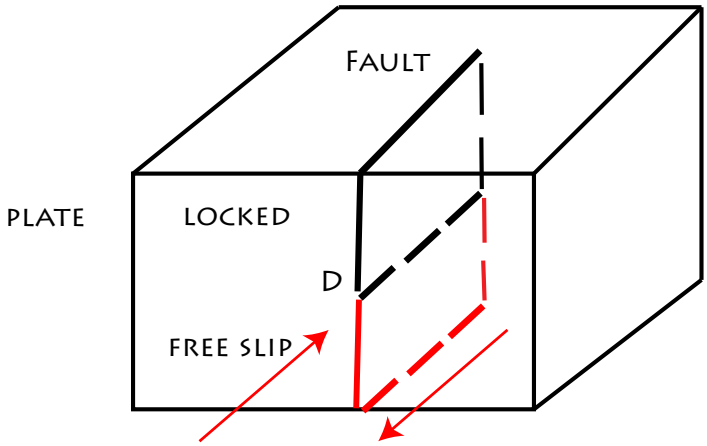

Figure 1.1: A cross-section of a vertical strike-slip fault in the elastic plate. The fault is locked from the surface down to the locking depth D. The deeper section of the fault is freely slipping driven by tectonic force. The earthquakes occur in the upper locked portion of the fault and the seismic moment is related to the rupture area of the fault.

1.1 Outline of the dissertation

This dissertation consists of five chapters. The first chapter is an introduction to the studied problems and approaches. The second chapter is a study using InSAR and limited GPS data to characterize the co-seismic deformation caused by a major intra-plate thrust event, Mw 7.9 Wenchuan earthquake. The third chapter is a study on the co-seismic slip of the Mw8.8 megathrust over Maule, Chile

using InSAR and limited GPS data. The fourth chapter is a study to integrate InSAR and GPS measurements to derive a high-resolution inter-seismic velocity field along the entire San Andreas Fault system where there are 750 high accuracy continuous GPS data available. In the fifth chapter I use this newly derived velocity field, along with GPS data, to improve the 3-dimensional visco-elastic deformation model along the San Andreas Fault system (Figure 1.2). One of the new aspects of my dissertation is to develop software tools needed to analyze InSAR data from a new Japanese L-band satellite called ALOS-1. The longer wavelength of the new L-band system (23.6 cm) with respect to the older C-band (5.6 cm) has enabled the construction of long time-span interferograms in vegetated areas. Moreover by contributing to the construction of a new software tool called GMTSAR, I was able to optimize the code for my applications. In particular, both the Wenchuan and Maule Chile InSAR analyses involved L-band ScanSAR interferometry which had not been attempted prior to this research. These ScanSAR interferograms provided a second look direction that was essential for constructing the slip models of the earthquakes.

1.2 Earthquake cycle study

1.2.1 Continental thrust - Mw 7.9 Wenchuan earthquake

Since India plate collided into Asia plate 45-65 Ma ago the crust between the India and Asia is shortened and thickened, making Tibet plateau one of the largest plateau in the world. The mountain building process leads to complex faulting within and around the plateau. M7.9 Wenchuan earthquake, a manifestation of these active faults, occurred at Longman Shan thrust belt between the eastern margin of the Tibet plateau and the Sichuan basin. In general the lithosphere dynamics in Longman Shan thrust belts (LST) are not well studied. The elastic thickness of LST based on gravity data ranges from 7 km to 36 km (*Fielding and McKenzie*, 2012; *Jiang and Jin*, 2005; *Jordan and Watts*, 2005). In particular the fault slip rate estimate based on geology and geodesy differ markedly (*Chen and*

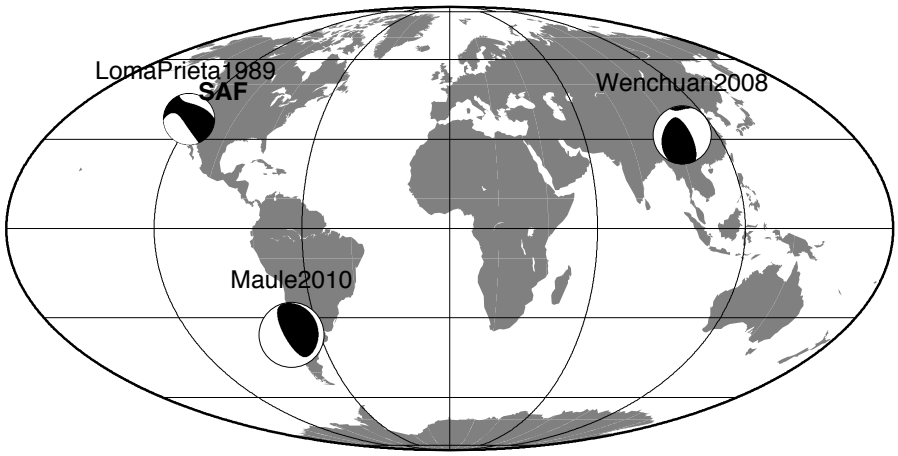

Figure 1.2: A map showing the studied regions: Wenchuan earthquake in China, Maule earthquake in Chile, the San Andreas Fault (SAF) in California, U.S.. The beach balls illustrate the differing styles of earthquake rupture in the three areas. The Wenchuan earthquake is thrust fault with right-lateral strike-slip. The Maule event is dominantly thrust fault with a shallow dip. The Loma Prieta earthquake is right-lateral strike-slip with thrust component.

Wilson, 1996; *Densmore et al.*, 2007; *Meade*, 2007; *Thatcher*, 2007; *Burchfiel et al.*, 2008; *Loveless and Meade*, 2011; *Chen et al.*, 2000). The on-going debate about the lower crust flow beneath Eastern Tibet is elusive (*Hubbard and Shaw*, 2009; *Royden et al.*, 2008). Nonetheless the LST was taken as an oblique thrust fault with low slip-rate (a few mm/yr) and long recurrence interval (5,000 to 10,000 years) so the Wenchuan earthquake is an unexpected event. This devastating event shows us not to under-estimate the earthquake hazards of the faults that are in similar tectonic settings. Studying the co-seismic and post-seismic relaxation process provide new insight on the stress regime of the LST (*Medina Luna and Hetland*, 2012; *Tong et al.*, 2010a) and rheological parameters beneath the Eastern Tibet (*Huang and Burgmann*, 2012).

1.2.2 Subduction zone megathrust - Mw8.8 megathrust Maule, Chile

The subduction zone is the convergent plate boundary where the dense and cold oceanic lithosphere thrust underneath the buoyant continental lithosphere. Along the Chile subduction zone the oceanic Nazca plate is seismically coupled with the over-riding South America plate at the plate interface. The degree of coupling is an important parameter and they vary from 0 (no coupling) to 1 (fully coupled). There are two different ways to estimate this coupling coefficient either using seismic moment released over a long period of time or geodetic data during the strain accumulation period (*Scholz and Campos*, 2012; *Chlieh et al.*, 2004; *Brooks et al.*, 2003; *Moreno et al.*, 2011). For example the spatially distribution of interseismic locking of the subduction zone near Japan are derived using GPS velocity data (*Loveless and Meade*, 2010). In the long term the accumulated moment along the plate interface is released by mega-thrust earthquakes with a repeat interval of hundreds of years. The M8.8 Maule, Chile is studied using seismic, gravity, GPS, InSAR, and tsunami observations (*Lay et al.*, 2010; *Tong et al.*, 2010b; *Vigny et al.*, 2011; *Luttrell et al.*, 2011; *Lorito et al.*, 2011; *Pollitz et al.*, 2011; *Delouis et al.*, 2010; *Wang et al.*, 2012). The InSAR observation from ALOS-1 provided an excellent co-seismic deformation map in a timely manner as the GPS coverage is sparse in this region. Although the published slip models differ in details due to the non-uniqueness of the inversion, all the models recovered an enhanced slip area, so called "asperity", in the northern part of the epicenter. This enhanced slip can be compared with the inter-seismic coupling distribution determined by a GPS network. Previous comparison used preliminary slip models based on teleseismic data only is subjected to large uncertainties (*Moreno et al.*, 2010). The stress change caused by co-seismic slip possibly leads to a subsequent normal faulting event within the over-riding plate (*Ryder et al.*, 2012). The magnitude of the shear stress released by this event is similar to the tectonic stress required to balancing the mountain loading (*Luttrell et al.*, 2011). It is possible that the Maule event didn't release all the intersesmic moment, especially in the southern part of the rupture area. The co-seismic slip diminished at 40-50 km depth, probably

the zone of brittle-ductile transition. The post-seismic period following megathrust earthquakes often involve brittle creep along the velocity-strengthening region of the fault zone and the visco-elastic relaxation beneath the brittle part of the lithosphere (*Perfettini et al.*, 2005; *Shearer and Bürgmann*, 2010).

1.2.3 The San Andreas fault

The San Andreas Fault system is one of the most-studied transform systems because it is close to highly populated regions. In this section I will briefly review studies on the fault slip rates of the SAF and the block modeling approach.

The geodetic approach to constrain the fault slip rates of individual faults is through block modeling (*McCaffrey*, 2005; *Meade and Hager*, 2005). The surface of the earth is divided into rigid, rotating microplates, so called blocks, bounded by major faults. The deformation is described as block rotation and intersesmic locking of the faults in the elastic upper plate. The interseismic strain is commonly simulated using the back-slip approach. *McCaffrey* (2005) also included the uniform strain inside blocks to account for the internal deformation within the blocks. This block approach is applied to estimate fault slip rates worldwide where GPS network are dense (*Loveless and Meade*, 2011). There are several problems with this block modeling approach: first, the block boundaries are not well determined in many regions, leading to uncertainties in the slip rates estimates (*Aktug et al.*, 2009). Second, the interseismic locking doesnt account for the viscoelastic effect in the lower crust and upper mantle (*Nur and Mavko*, 1974; *Smith-Konter and Sandwell*, 2009), where the early stage of the interseismic locking can be different from the late stage.

GPS data are used in constraining the long term slip rate in Uniform California Earthquake Rupture Forecast version 3 (UCERF3). This geodetic slip rates are combined with the geological fault slip rates to evaluate seismic risk. In some regions, the density of GPS sites is not adequate for resolving the small-scale deformation which is mostly concentrated in the shallow crust. In this dissertation I use both the GPS and InSAR to better constrain the asperities and interseismic strain accumulation along the entire San Andreas Fault system. The following is

a brief review of how GPS and InSAR are used to study the earthquake cycle.

1.3 GPS basics

Global Positioning System (GPS) is a global navigation satellite system. Currently there are 32 GPS satellites orbiting around the earth, capable of providing navigation/position service on the ground or in space at accuracies ranging from 10s meters to sub-centimeter depending on the types of receiving devices and the observing modes.

The principal of position determination is based on the time delay measurements of the radio signals transmitted from the GPS satellites to receiving devices. With the observations from 4 or more simultaneously tracked GPS satellites (assuming their ephemerides known), a 3D position can be fixed in space at any given time. There are two types of measurements, known as "code" or "pseudo-range", and "phase" measurements. The former counts the Doppler shift of radio frequency in multiples of wavelength, and the latter measures the phase shift of radio frequency in fractional of wavelength, which increases the measurement accuracy significantly when combined with the "code" measurement. GPS is subject to many error sources, such as those related to satellite orbit dynamics influenced by the earth's gravity field, earth orientation parameters, solar radiation pressure, path delays caused by ionospheric and tropospheric effects, and satellite and receiver clock errors. With great efforts from geodetic science community, these errors have been carefully studied, leading to a full suite of methods/models to eliminate or mitigate their impacts.

Starting from 1990s high-precision GPS is used to reveal mm-level surface deformation in various geophysical problems: ranging from plate motions, earthquake source properties, inter-seismic strain accumulation, "slow-slip" events to inflation of volcanoes, dynamic ground motion and hydrological signals. In earth science, some applications require a dense spatial coverage of GPS to accurately reveal the spatial pattern of the deformation source at depth. That justifies the establishment of dense continuous GPS (CGPS) network.

Nowadays dense continuous GPS network are in operation in earthquake-prone countries such as the western United States and Japan. The Plate Boundary Observatory (PBO) constitutes of over 1000 continuous GPS sites mostly over western US. From this network, complemented by other CGPS networks, the users from academic, government, and industrial sectors can obtain extremely accurate daily GPS solutions processed by experts in the field. Campaign mode GPS can complement the spatial coverage of the existing GPS network. There is an on-going effort to upgrade the GPS stations to operate in real-time so that an earthquake early-warning system can be established. However the spatial coverage of the GPS network is very limited in other parts of the world such as Tibet, South America. Interferometric Synthetic Aperture Radar (InSAR) can provide dense spatial coverage of the surface deformation over remote areas thus is highly complementary to GPS observation.

1.4 InSAR

1.4.1 InSAR basics

Interferometric Synthetic Aperture Radar (InSAR) is an advanced remote sensing technique, which can map fine-scaled (10-20 meter) surface deformation over remote areas. Its high-spatial resolution coupled with wide coverage and remote sensing capabilities are complementary to GPS and other geodetic measurements. InSAR has successfully recovered a variety of surface deformation, which is not possible with any other geodetic method. An incomplete list of its applications includes: coseismic slip (*Elliott et al.*, 2012), aseismic fault creep over the creeping fault (*Ryder and Burgmann*, 2008), triggered surface fault creep accompanying the earthquakes (*Wei et al.*, 2009), block rotation during the Landers earthquake (*Peltzer et al.*, 1994), rifting event (*Sandwell et al.*, 2008), after-slip (*Barbot et al.*, 2009), poro-elastic response (*Fialko*, 2004), visco-elastic relaxation (*Pollitz et al.*, 2001), hydrological effect (*Wisely and Schmidt*, 2010), volcano deformation (*Pritchard and Simons*, 2002). There are several reviews on InSAR techniques and its application on geosciences (*Bürgmann et al.*, 2000; *Rosen et al.*,

2000; *Massonnet and Feigl*, 1998). In this section I will review briefly the basics of InSAR and recent developments in the InSAR time-series analysis.

Typically radar can provide 2-dimensional (along-track and across-track dimension) images of the earth by transmitting microwaves to the ground and receiving the back-scattered signal. Based on the diffraction theory in optics the conventional radar in low earth orbit can't distinguish ground features smaller than 50 km. Nevertheless Synthetic Aperture Radar (SAR) can image the surface with a pixel resolution of 10-20 meters. This increased resolution is achieved by complex processing techniques. Increasing the bandwidth of the radar pulse enhances the range resolution and the Doppler effect of the radar signal is used to differentiate the targets in along-track. After appropriate processing the radar images consist of two sets of information: the amplitude and the phase. The amplitude contains information about the reflectivity of the earth, which is controlled by the surface roughness and the dielectric constant of the target. The phase signal is usually not used as the phase change due to scatter on the ground is unpredictable.

InSAR combines the interferometric and the SAR techniques into a new powerful imaging tool to recover accurate digital elevation model (*Zebker et al.*, 1994; *Sandwell and Sichoix*, 2000; *Farr et al.*, 2007) and surface deformation (*Rosen et al.*, 2000). An interferogram is derived by taking the phase difference of two SAR images observed at different times. If the common phase change due to the scattering of the target are very similar for the two SAR images, a coherent phase signal containing the path delay effect between the ground and the antenna can be retrieved.

The resultant interferogram consists of the following signals and noises: 1) phase ramps due to the spherical geometry of the earth; 2) inaccurate orbit information; 3) topographic phase due to digital elevation model (DEM); 4) atmospheric and ionospheric delay; 5) surface displacement during the two SAR acquisition time. The ground displacement in the radar line-of-sight direction can be recovered by properly reducing the other phase components. The signal to noise ratio of the phase measurement is evaluated by the estimation of correlation.

The phase that ranges from $-\pi$ to π needs to be unwrapped to represent

continuous topography or surface deformation. This procedure is called "phase unwrapping" and it is an important step in the InSAR processing. There are two popular methods in phase unwrapping: the branch-cut method (*Goldstein et al.*, 1988) and the minimization method based on statistics (*Chen and Zebker*, 2002). And there are new approaches being proposed such as the phase unwrapping in 3-dimensions (*Hooper and Zebker*, 2007).

Similar to GPS, the detailed analysis on the InSAR phase data focused on resolving the temporal behavior of the surface deformation. For studying earthquakes, the ground motion can be analyzed using a single interferogram that spans the event. For the steady-state interseismic deformation, one can average multiple independent interferograms over long time period, a method termed "stacking" (*Sandwell and Price*, 1998). InSAR time series methods have been developed to monitor the non steady-state components of the surface deformation, such as the transient deformation, seasonal changes, and deformation of active volcanoes. Currently there are generally two types of InSAR time-series methods: the Small-Baseline Subset method and the Persistent Scatter method. The Small-Baseline Subset (SBAS) method uses the interferograms with small perpendicular baselines to minimize the noise due to baseline decorrelation. The approach solves for the incremental displacement at each SAR acquisition time and an error in the digital elevation model. This method has succeeded in areas like Los Angeles basin and Santa Clara valley where it recovered the seasonal variation of the surface related to groundwater pumping and recharge (*Lanari et al.*, 2004; *Schmidt and Bürgmann*, 2003). It is less useful for other regions where the coherence of the interferogram is degraded. Another type of method identifies point scatterers that are coherent over time regardless of the baseline limitation. The following procedure is to maximize the correlation by jointly estimating phase signal from the deformation, error in digital elevation model and atmospheric delay. This persistent scatterer method is used to monitor surface changes of buildings in urban areas (*Ferretti et al.*, 2001). However this method is less effective in areas where point scatterers are lacking so various techniques have been developed to overcome this difficulty.

Instead of exploiting the phase information, one can perform 2-dimensional

cross-correlation on any two Single Look Complex (SLC) images. This technique is termed speckle tracking or pixel tracking. The idea behind this technique is as follows: one takes a small piece of the images (64 by 64 pixels) and performs cross-correlation against the corresponding part in the other images. This yields the offset in both the across-track and along-track direction. The precision of the offset estimation can reach 1/10th or 1/20th of a pixel. This pixel tracking approach has been used to map detailed kinematics of the ice-flow over Antarctica (*Rignot*, 2008) and co-seismic displacement over major earthquakes (*Fialko et al.*, 2005). One major limitation of InSAR is that it only measures the surface displacement in radar line-of-sight direction. Thus its necessary to combine the radar line-of-sight displacement from ascending and descending orbits to reduce the ambiguities in 3-dimensional deformation (*Tong et al.*, 2010a,b). With the additional constraint from pixel tracking, one could reconstruct the 3-components of the ground deformation (*Wright et al.*, 2004; *Sandwell et al.*, 2008).

1.4.2 PALSAR from ALOS-1

There have been several SAR satellite missions that are dedicated to monitoring earth environmental changes: ERS1/2 and ENVISAT launched by European Space Agency and the ALOS-1 launched by Japanese Aerospace Exploration Agency. The ERS1 has operated from 1991 to 2000 for 9 years and the ERS2 has operated from 1995 to 2011 for 16 years. The ENVISAT satellite mission lasted from 2002 to 2012 for about 9 years. The ALOS-1 satellite was launched in early 2006 and lasted 5 years. The ERS1/2 and ENVISAT carries the SAR operated in C-band (5.6cm) while the radar onboard ALOS-1 is in L-band (23.6cm) (*Rosenqvist et al.*, 2007; *Shimada et al.*, 2010; *Sandwell et al.*, 2008). L-band radar can penetrate through the leafy canopy to the ground while C-band can be reflected at the top of the canopy. For this reason L-band radar is good at maintaining excellent temporal correlation over areas where vegetation has seasonal changes. The Phase Array L-band Synthetic Aperture Radar (PALSAR) can be operated in five different observation modes: Fine Beam Single polarization (FBS), Fine Beam Dual polarization (FBD), Polarimetric mode (POL), ScanSAR mode and

Direct Transmission mode (DT). The FBS has a bandwidth of 28 MHz and FBD has 14 MHZ so FBS has finer ranging resolution. The FBS and FBD have 34.3 deg off-nadir angle. The swath width of the fine beam mode is about 70 km. The radar can sweep through a much wider swath by steering the antenna electronically in the across-track direction. The wide-swath ScanSAR (350 km width) onboard ALOS-1 is operated in five-beam mode transmitting in 14 MHz bandwidth. A detailed description of ScanSAR and its application to earthquake studies is in Appendix A.

1.4.3 GMTSAR

I have worked on developing open source InSAR processing software GMTSAR (*Sandwell et al.*, 2011) with my advisor and others to facilitate community research using radar interferometry. This software divides the processing tasks (pre-processing, image co-registration, generating topographic phase, performing interferometry and projection) into different modules (C programs) and the different modules are connected with shell scripts. Currently it is capable to perform the following data processing automatically: two-pass interferometry, batch processing of a stack of images and stacking. It supports processing the SAR data from ERS, ENVIST and ALOS-1. I have also developed custom algorithms to process ScanSAR interferometry. In the near future this software will become part of the Generic Mapping Tool (GMT) (*Wessel and Smith*, 1995). More detailed information about this software can be found at http://topex.ucsd.edu/gmtsar.

References

Aktug, B., et al. (2009), Deformation of western Turkey from a combination of permanent and campaign GPS data: Limits to block-like behavior, *Journal of Geophysical Research*, *114*(B10), B10,404.

Barbot, S., Y. Fialko, and Y. Bock (2009), Postseismic deformation due to the Mw 6.0 2004 Parkfield earthquake: Stress-driven creep on a fault with spatially variable rate-and-state friction parameters, *Journal of Geophysical Research*, *114*(B7), B07,405.

Brooks, B. A., M. Bevis, R. Smalley Jr, E. Kendrick, R. Manceda, E. Lauria, R. Maturana, and M. Araujo (2003), Crustal motion in the southern Andes (26–36 s): Do the Andes behave like a microplate?, *Geochemistry Geophysics Geosystems*, *4*(10), 1085.

Burchfiel, B., et al. (2008), A geological and geophysical context for the Wenchuan earthquake of 12 May 2008, Sichuan, People's Republic of China, *GSA Today*.

Bürgmann, R., P. A. Rosen, and E. J. Fielding (2000), Synthetic aperture radar interferometry to measure earth's surface topography and its deformation, *Annual Review of Earth and Planetary Sciences*, *28*(1), 169–209.

Chen, C. W., and H. A. Zebker (2002), Phase unwrapping for large SAR interferograms: statistical segmentation and generalized network models, *Geoscience and Remote Sensing, IEEE Transactions on*, *40*(8), 1709–1719.

Chen, S. F., and C. J. Wilson (1996), Emplacement of the Longmen Shan thrust-nappe belt along the eastern margin of the Tibetan plateau, *Journal of Structural Geology*, *18*(4), 413–430.

Chen, Z., B. Burchfiel, Y. Liu, R. King, L. Royden, W. Tang, E. Wang, J. Zhao, and X. Zhang (2000), Global Positioning System measurements from eastern Tibet and their implications for India/Eurasia intercontinental deformation, *Journal of Geophysical Research*, *105*(B7), 16–215.

Chlieh, M., J. De Chabalier, J. Ruegg, R. Armijo, R. Dmowska, J. Campos, and K. Feigl (2004), Crustal deformation and fault slip during the seismic cycle in the north Chile subduction zone, from GPS and InSAR observations, *Geophysical Journal International*, *158*(2), 695–711.

Delouis, B., J.-M. Nocquet, and M. Vallée (2010), Slip distribution of the February 27, 2010 Mw= 8.8 Maule earthquake, central Chile, from static and high-rate GPS, InSAR, and broadband teleseismic data, *Geophysical Research Letters*, *37*(17), L17,305.

Densmore, A. L., M. A. Ellis, Y. Li, R. Zhou, G. S. Hancock, and N. Richardson (2007), Active tectonics of the Beichuan and Pengguan faults at the eastern margin of the Tibetan plateau, *Tectonics*, *26*(4), TC4005.

Elliott, J., E. Nissen, P. England, J. A. Jackson, S. Lamb, Z. Li, M. Oehlers, and B. Parsons (2012), Slip in the 2010–2011 Canterbury earthquakes, New Zealand, *Journal of Geophysical Research*, *117*(B3), B03,401.

Farr, T. G., P. A. Rosen, E. Caro, R. Crippen, R. Duren, S. Hensley, M. Kobrick, M. Paller, and E. R. et al. (2007), The shuttle radar topography mission, *Reviews of Geophysics*, *45*(2), doi:10.1029/2005RG000183.

Ferretti, A., C. Prati, and F. Rocca (2001), Permanent scatterers in SAR interferometry, *Geoscience and Remote Sensing, IEEE Transactions on*, *39*(1), 8–20.

Fialko, Y. (2004), Evidence of fluid-filled upper crust from observations of post-seismic deformation due to the 1992 Mw7. 3 landers earthquake, *Journal of geophysical research*, *109*(B8), B08,401.

Fialko, Y., D. Sandwell, M. Simons, and P. Rosen (2005), Three-dimensional deformation caused by the bam, iran, earthquake and the origin of shallow slip deficit, *Nature*, *435*(7040), 295–299.

Fielding, E. J., and D. McKenzie (2012), Lithospheric flexure in the Sichuan basin and Longmen shan at the eastern edge of Tibet, *Geophysical Research Letters*, *39*(9), L09,311.

Goldstein, R., H. Zebker, and C. Werner (1988), Satellite radar interferometry-two-dimensional phase unwrapping, *Radio Science*, *23*(4), 713–720.

Hooper, A., and H. A. Zebker (2007), Phase unwrapping in three dimensions with application to InSAR time series, *JOSA A*, *24*(9), 2737–2747.

Huang, M., and R. Burgmann (2012), Probing the deep rheology of Tibet constraints from 2008m_w7.9 Wenchuan, China earthquake, in *AGU Fall Meeting Abstracts*.

Hubbard, J., and J. H. Shaw (2009), Uplift of the Longmen shan and Tibetan plateau, and the 2008 Wenchuan (m= 7.9) earthquake, *Nature*, *458*(7235), 194–197.

Jiang, X., and Y. Jin (2005), Mapping the deep lithospheric structure beneath the eastern margin of the Tibetan plateau from gravity anomalies, *Journal of geophysical research*, *110*(B7), B07,407.

Jordan, T., and A. Watts (2005), Gravity anomalies, flexure and the elastic thickness structure of the India–Eurasia collisional system, *Earth and Planetary Science Letters*, *236*(3), 732–750.

Lanari, R., O. Mora, M. Manunta, J. J. Mallorquí, P. Berardino, and E. Sansosti (2004), A small-baseline approach for investigating deformations on full-resolution differential SAR interferograms, *Geoscience and Remote Sensing, IEEE Transactions on*, *42*(7), 1377–1386.

Lay, T., C. Ammon, H. Kanamori, K. Koper, O. Sufri, and A. Hutko (2010), Teleseismic inversion for rupture process of the 27 February 2010 Chile (Mw 8.8) earthquake, *Geophysical Research Letters*, *37*(13), L13,301.

Lorito, S., F. Romano, S. Atzori, X. Tong, A. Avallone, J. McCloskey, M. Cocco, E. Boschi, and A. Piatanesi (2011), Limited overlap between the seismic gap and coseismic slip of the great 2010 Chile earthquake, *Nature Geoscience*, *4*(3), 173–177.

Loveless, J., and B. Meade (2011), Partitioning of localized and diffuse deformation in the Tibetan plateau from joint inversions of geologic and geodetic observations, *Earth and Planetary Science Letters*, *303*(1), 11–24.

Loveless, J. P., and B. J. Meade (2010), Geodetic imaging of plate motions, slip rates, and partitioning of deformation in Japan, *Journal of Geophysical Research*, *115*(B2), B02,410.

Luttrell, K. M., X. Tong, D. T. Sandwell, B. A. Brooks, and M. G. Bevis (2011), Estimates of stress drop and crustal tectonic stress from the 27 February 2010 Maule, Chile, earthquake: Implications for fault strength, *Journal of Geophysical Research*, *116*(B11), B11,401.

Massonnet, D., and K. L. Feigl (1998), Radar interferometry and its application to changes in the earth's surface, *Reviews of geophysics*, *36*(4), 441–500.

McCaffrey, R. (2005), Block kinematics of the Pacific-north America plate boundary in the southwestern united states from inversion of GPS, seismological, and geologic data, *Journal of Geophysical Research-Solid Earth*, *110*(B07401), doi: 10.1029/2004jb003307.

Meade, B. J. (2007), Present-day kinematics at the India-Asia collision zone, *Geology*, *35*(1), 81–84.

Meade, B. J., and B. H. Hager (2005), Spatial localization of moment deficits in southern California, *Journal of Geophysical Research-Solid Earth*, *110*(B4), B04,402, doi:10.1029/2004JB003331.

Medina Luna, L., and E. A. Hetland (2012), Regional stresses inferred from coseismic slip models of the 2008 Mw 7.9 Wenchuan, China, earthquake, *Tectonophysics*.

Moreno, M., M. Rosenau, and O. Oncken (2010), 2010 Maule earthquake slip correlates with pre-seismic locking of andean subduction zone, *Nature*, *467*(7312), 198–202.

Moreno, M., et al. (2011), Heterogeneous plate locking in the south–central Chile subduction zone: Building up the next great earthquake, *Earth and Planetary Science Letters*, *305*(3), 413–424.

Nur, A., and G. Mavko (1974), Postseismic viscoelastic rebound, *Science*, *183*(4121), 204–206.

Peltzer, G., K. W. Hudnut, and K. L. Feigl (1994), Analysis of coseismic surface displacement gradients using radar interferometry: New insights into the Landers earthquake, *JOURNAL OF GEOPHYSICAL RESEARCH-ALL SERIES-*, *99*, 21–21.

Perfettini, H., J.-P. Avouac, and J.-C. Ruegg (2005), Geodetic displacements and aftershocks following the 2001 Mw= 8.4 Peru earthquake: Implications for the mechanics of the earthquake cycle along subduction zones, *Journal of Geophysical Research B*, *110*(B9), Art–No.

Pollitz, F. F., C. Wicks, and W. Thatcher (2001), Mantle flow beneath a continental strike-slip fault: Postseismic deformation after the 1999 Hector Mine earthquake, *Science*, *293*(5536), 1814–1818.

Pollitz, F. F., et al. (2011), Coseismic slip distribution of the February 27, 2010 Mw 8.8 Maule, Chile earthquake, *Geophysical Research Letters*, *38*(9), L09,309.

Pritchard, M. E., and M. Simons (2002), A satellite geodetic survey of large-scale deformation of volcanic centres in the central Andes, *Nature*, *418*(6894), 167–171.

Rignot, E. (2008), Changes in west Antarctic ice stream dynamics observed with ALOS PALSAR data, *Geophysical Research Letters*, *35*(12), L12,505.

Rosen, P. A., S. Hensley, I. R. Joughin, F. K. Li, S. N. Madsen, E. Rodriguez, and R. M. Goldstein (2000), Synthetic aperture radar interferometry, *Proceedings of the IEEE*, *88*(3), 333–382.

Rosenqvist, A., M. Shimada, N. Ito, and M. Watanabe (2007), ALOS PALSAR: A pathfinder mission for global-scale monitoring of the environment, *Geoscience and Remote Sensing, IEEE Transactions on*, *45*(11), 3307–3316.

Royden, L. H., B. C. Burchfiel, and R. D. van der Hilst (2008), The geological evolution of the Tibetan plateau, *science*, *321*(5892), 1054–1058.

Ryder, I., and R. Burgmann (2008), Spatial variations in slip deficit on the central San Andreas Fault from InSAR, *Geophysical Journal International*, *175*(3), 837–852, doi:10.1111/j.1365-246X.2008.03938.x.

Ryder, I., A. Rietbrock, K. Kelson, R. Bürgmann, M. Floyd, A. Socquet, C. Vigny, and D. Carrizo (2012), Large extensional aftershocks in the continental forearc triggered by the 2010 Maule earthquake, Chile, *Geophysical Journal International*.

Sandwell, D., R. Mellors, X. Tong, M. Wei, and P. Wessel (2011), Open radar interferometry software for mapping surface deformation, *Eos Trans. AGU*, *92*(28), 234, doi:10.1029/2011EO280002.

Sandwell, D. T., and E. J. Price (1998), Phase gradient approach to stacking interferograms, *Journal of Geophysical Research-Solid Earth*, *103*(B12), 30,183–30,204, doi:10.1029/1998JB900008.

Sandwell, D. T., and L. Sichoix (2000), Topographic phase recovery from stacked ERS interferometry and a low-resolution digital elevation model, *Journal of Geophysical Research-Solid Earth*, *105*(B12), 28,211–28,222.

Sandwell, D. T., D. Myer, R. Mellors, M. Shimada, B. Brooks, and J. Foster (2008), Accuracy and resolution of alos interferometry: Vector deformation maps of the Father's day intrusion at Kilauea, *Geoscience and Remote Sensing, IEEE Transactions on*, *46*(11), 3524–3534.

Schmidt, D. A., and R. Bürgmann (2003), Time-dependent land uplift and subsidence in the santa clara valley, California, from a large interferometric synthetic aperture radar data set, *J. geophys. Res*, *108*(B9), 2416.

Scholz, C. H., and J. Campos (2012), The seismic coupling of subduction zones revisited, *Journal of Geophysical Research*, *117*(B5), B05,310.

Shearer, P., and R. Bürgmann (2010), Lessons learned from the 2004 Sumatra-Andaman megathrust rupture, *Annual Review of Earth and Planetary Sciences*, *38*, 103–131.

Shimada, M., T. Tadono, and A. Rosenqvist (2010), Advanced land observing satellite (alos) and monitoring global environmental change, *Proceedings of the IEEE*, *98*(5), 780–799.

Smith-Konter, B., and D. Sandwell (2009), Stress evolution of the San Andreas fault system: Recurrence interval versus locking depth, *Geophysical Research Letters*, *36*(L13304), doi:10.1029/2009GL037235.

Thatcher, W. (2007), Microplate model for the present-day deformation of Tibet, *J. geophys. Res*, *112*(B01401), 1–13.

Tong, X., D. T. Sandwell, and Y. Fialko (2010a), Coseismic slip model of the 2008 Wenchuan earthquake derived from joint inversion of interferometric synthetic aperture radar, GPS, and field data, *Journal of Geophysical Research*, *115*(B4), B04,314.

Tong, X., et al. (2010b), The 2010 Maule, Chile earthquake: Downdip rupture limit revealed by space geodesy, *Geophysical Research Letters*, *37*(24), L24,311.

Vigny, C., et al. (2011), The 2010 Mw 8.8 Maule megathrust earthquake of central Chile, monitored by GPS, *Science*, *332*(6036), 1417–1421.

Wang, L., et al. (2012), Coseismic slip of the 2010 Mw 8.8 great Maule, Chile, earthquake quantified by the inversion of GRACE observations, *Earth and Planetary Science Letters*, *335*, 167–179.

Wei, M., D. Sandwell, and Y. Fialko (2009), A silent m(w) 4.7 slip event of october 2006 on the Superstition Hills fault, southern California, *Journal of Geophysical Research-Solid Earth*, *114*, B07,402, doi:10.1029/2008JB006135.

Wessel, P., and W. H. Smith (1995), New version of the Generic Mapping Tools released, *Eos Trans. AGU*, *76*(33), 329.

Wisely, B. A., and D. Schmidt (2010), Deciphering vertical deformation and poroelastic parameters in a tectonically active fault-bound aquifer using InSAR and well level data, san bernardino basin, California, *Geophysical Journal International*, *181*(3), 1185–1200, doi:10.1111/j.1365-246X.2010.04568.x.

Wright, T. J., B. E. Parsons, and Z. Lu (2004), Toward mapping surface deformation in three dimensions using InSAR, *Geophysical Research Letters*, *31*(1), L01,607.

Zebker, H. A., C. L. Werner, P. A. Rosen, and S. Hensley (1994), Accuracy of topographic maps derived from ERS-1 interferometric radar, *Geoscience and Remote Sensing, IEEE Transactions on*, *32*(4), 823–836.

Chapter 2

Coseismic slip model of the 2008 Wenchuan earthquake derived from joint inversion of InSAR, GPS and field data

We derived a coseismic slip model for the M7.9 2008 Wenchuan earthquake based on radar line-of-sight displacements from ALOS interferograms, GPS vectors, and geological field data. Available InSAR data provided a nearly complete coverage of the surface deformation along both ascending (fine beam mode) and descending orbits (ScanSAR to ScanSAR mode). The earthquake was modeled using 4 subfaults with variable geometry and dip to capture the simultaneous rupture of both the Beichuan and the Pengguan fault. Our model misfits show that the InSAR and GPS data are highly compatible; the combined inversion yields a 93% variance reduction. The best-fit model has fault planes that rotate from shallow dip in the south (35°) to nearly vertical dip toward the north (70° -90°). Our rupture model is complex with variations in both depth and rake along two major fault strands. In the southern segment of the Beichuan fault, the slip is

[0]This chapter is a reformatted version of a publication in *Journal of Geophysical Research*: Tong, X., D. T. Sandwell, Y. Fialko, "Coseismic slip model of the 2008 Wenchuan earthquake derived from joint inversion of InSAR, GPS and field data", v.115, B04314, doi:10.1029/2009JB006625, 2010

mostly thrust (< 13 m) and occurred principally in the upper 10 km of the crust; the rupture progressively transformed to right-lateral strike-slip as it propagated northeast (with maximum offsets of 7 m). Our model suggests that most of the moment release was limited to the shallow part of the crust (depth less than 10 km). We didnt find any "shallow slip deficit" in the slip-depth distribution of this mixed-mechanism earthquake. Aftershocks were primarily distributed below the section of the fault that ruptured coseismically.

2.1 Introduction

On May 12th 2008, a major (Mw 7.9) earthquake struck Wenchuan County, Sichuan Province in China. The causalities include approximately 70,000 dead and 374,000 injured. The rupture accompanying the event extended over 270 km toward the northeast along Longmen Shan thrust belt and is a result of the convergent tectonic movement between Tibetan Plateau and Sichuan Basin (Figure 2.1). The region of the earthquake is characterized by a 3 km topographic step across the rupture zone from the relatively flat lowlands of the Sichuan basin to the east to the rugged highlands of the Longmen Shan to the west (*Burchfiel et al.*, 2008).

The interseismic Global Positioning System (GPS) data collected between 1991 and 1998 reveal low shortening rate (< 3mm/yr) across Longmen Shan fault zone (*Chen et al.*, 2000). Geologic and geomorphologic observations suggest that the parallel Beichuan fault (also referred to as Yingxiu-Beichuan fault) and Pengguan faults are active and dominated by dextral-slip structures (*Kirby et al.*, 2003; *Densmore et al.*, 2007). The 2008 event started at the southern end of Beichuan fault at depth around 16 km (*Huang et al.*, 2008) and propagated toward northeast. Geological survey found that surface rupture occurred on two parallel fault strands: Beichuan fault (240-270 km) and Pengguan fault (70 km) (Figure 2.1). The survey established that the surface rupture is extensive with an average offset of 2 m. The maximum reported vertical throw is 6 m and the maximum horizontal offset is 4.9 m (*Liu-Zeng et al.*, 2009). There were 2706 events with a magnitude

above 2.0 following the mainshock by the end of July 8th 2008. Double difference relocation reveals that 95% of aftershocks were distributed over a depth interval of 10 to 20 km below the Earths surface (*Huang et al.*, 2008). The coseismic displacements due to the 2008 event were studied using Synthetic Aperture Radar (SAR) pixel-tracking method (*Kobayashi et al.*, 2009) as well as Interfeometric Synthetic Aperture Radar (InSAR) (*Hao et al.*, 2009). Although the measurement accuracy is limited, *Kobayashi et al.* (2009) demonstrated that the rupture involved both the Beichuan fault and the Pengguan fault, consistent with the decorrelation zone in radar interferograms (as discussed below) and the geological survey. Studies based on teleseismic and GPS observations respectively indicate that the coseismic motion involved both thrust and dextral slip components (*Ji and Hayes*, 2008; *Crustal Motion Observation Network of China Project*, 2008), but the spatial variation of the right-lateral strike-slip and dip-slip, along with the depth distribution of fault slip are not well constrained. The more recent InSAR analysis (*Hao et al.*, 2009) using 7 ascending tracks of ALOS PALSAR data revealed significant change in slip magnitude and direction along the rupture surface.

In this study, we integrate Interfeometric Synthetic Aperture Radar (InSAR) data collected by the ALOS satellite (both ascending and descending), Global Positioning System (GPS) data, geological field observations, along with Greens functions for an elastic half space (*Okada*, 1985) to derive a coseismic slip model for the Wenchuan earthquake. The model allows for spatially variable rake angles and illustrates relative contributions of the thrust and strike-slip motion in the deeper part of the fault, as well as the along-strike variability. The inferred slip distribution can be used as a constraint in time-dependent inversions using seismic data (*Hernandez et al.*, 1999; *Delouis et al.*, 2002), in studies of the coseismic stress changes (*King et al.*, 1994) and as an initial condition to drive models of postseismic relaxation (*Pollitz et al.*, 2000; *Hearn et al.*, 2002; *Fialko*, 2004; *Perfettini and Avouac*, 2007; *Barbot et al.*, 2009). The latter can be compared to the geodetic data collected after the earthquake to constrain the relaxation mechanisms, effective rheology, and provide insights into time-dependent stress transfer and future seismic hazard.

2.2 Data analysis

Rugged topography of the region combined with high rainfall and dense vegetation severely limits the correlation of C-band interferograms to only the flat lowland areas. In contrast, adequate interferometric correlation is maintained in the longer wavelength L-band SAR imagery provided by the PALSAR (Phase Array L-band Synthetic Aperture Radar) aboard the ALOS (Advanced Land Observation Satellite) satellite (*Rosenqvist et al.*, 2007). After the launch of ALOS by JAXA (Japanese Aerospace Exploration Agency) in January of 2006, a global background mission collected strip-mode SAR imagery approximately 4 times per year on ascending tracks and ScanSAR (Scanning Synthetic Aperture Radar) imagery 4 times per year on descending tracks. The improved correlation at L-band along with systematic pre-earthquake coverage enabled excellent coseismic InSAR coverage of the entire rupture zone. With the help of the Alaska Satellite Facility and JAXA, we assembled 78 scenes in FBS (Fine Beam Single polarization) and FBD (Fine Beam Dual polarization) mode from ascending orbit as well as 4 scenes in ScanSAR mode from descending orbit (*Tong et al.*, 2008). Topographic data, needed to perform the phase correction to the interferometry was provided by the SRTM-3 data (*Farr et al.*, 2007). The majority of void areas in the mountains have been filled from the best available alternative sources, including topographic maps, spot elevations on sketch maps and Landsat images [www.viewfinderpanoramas.org/dem3.html]. In addition to the InSAR data, we incorporated 109 GPS vectors (82 horizontal and 27 vertical) (*Crustal Motion Observation Network of China Project*, 2008) and geological field observations (*Liu-Zeng et al.*, 2009) as ground-truth constraints.

2.2.1 InSAR data processing

We used SIOSAR software to process ALOS PALSAR data (*Sandwell et al.*, 2008). We chose the SAR images from the available archive immediately following the earthquake as the repeat scenes, then search back in time to get the reference scenes with optimal baselines. The time span of the interferograms ranges from 46 days to 1.5 years; the latest one after the earthquake is on Jun 22, 2008, about 40

days after the main shock (Table 2.1). We assume coseismic signal dominates any postseismic response that may have occurred during interval between the mainshock and the first repeat acquisition on each track. The perpendicular baselines vary between 70 m and 844 m and the longer perpendicular baseline are more sensitive to topography. The short baselines along the ascending tracks help to reduce the topographic effect, which may obscure the surface deformation. The interferograms are processed frame by frame (6-8 frames per track) to improve image matching and keep file sizes manageable. Individually-processed interferograms mosaic seamlessly along the same track in either radar or geographic coordinates (Figure 2.2). A spatial Gaussian filter having a 0.5 gain at 300 m wavelength was applied to all the interferograms (*Sandwell et al.*, 2008). This cutoff wavelength is a compromise between greater smoothing for improved correlation in areas of extreme ground shaking and less smoothing to recover the high fringe rate caused by deformation near the rupture.

As well demonstrated by previous studies, more than one radar look direction is needed to provide reliable estimates of slip along a rupture (*Fialko et al.*, 2001; *Sandwell et al.*, 2002; *Simons et al.*, 2002; *Fialko*, 2004). In the case of ALOS, normal strip-mode interferometry is available on ascending orbits but along the descending orbits the only acquisitions are in the ScanSAR mode. We processed four ScanSAR scenes (track 124, frame 2950 and 3000) to provide additional line-of-sight (LOS) displacement measurements, though the long perpendicular baselines (657 844 m) along descending track led to complete decorrelation in the mountainous area (Figure 2.3). This is the first PALSAR ScanSAR to ScanSAR interferogram constructed by our group so we discuss the technical details of this development in Appendix A.

2.2.2 Interpretation of interferograms

Figure 2.2 and Figure 2.3 show the mosaics of 39 ascending and 2 descending radar interferograms in wrapped phase with a full coverage of 400 km by 400 km along the Longmen Shan fault zone. A zoom-in view of the interferogram illustrates dense phase fringes close to the rupture zone that document a complicated pattern

of surface deformation. The speckled area in the interferograms denotes regions of decorrelation. The red line is the surface rupture mapped by Jing Liu from the Chinese Academy of Sciences (*Liu-Zeng et al.*, 2009). The mapped faults align very well with the edge of the decorrelation near the fault zone: on east side of the faults, corresponding to the footwall, phase is recoverable all the way to the fault trace; on the west side, corresponding to the hanging wall, the signal is completely decorrelated. This is consistent with geologic and seismic observations showing that most of the ground shaking was concentrated on the hanging wall. While the lowland areas have good phase coherence, the phase recovery is less robust in the mountainous areas. Lower coherence on the hanging wall within 30 km of the fault zone is due to a combination of landsides, temporal decorrelation from vegetation, and inadequate topographic phase correction in the area of extreme relief. By directly counting the interferometric fringes and assuming zero displacement in the far field, we found that the peak LOS displacement in the ascending orbits is 99.4 cm on the hanging wall, -108.2 cm on the footwall; the peak LOS displacement in the descending orbits is -118.1 cm on the footwall.

2.2.3 Errors and trends in interferograms

We need to consider and mitigate the potential spurious contributions to the radar phase before interpreting it as coseismic surface displacements. There are several factors that prevent us from directly relating the interferogram to surface deformation signal (*Massonnet and Feigl*, 1998). The error sources come from the topographic phase correction, propagation effects due to the ionosphere and atmosphere, as well as orbital errors. The atmospheric propagation errors, mostly attributed to the tropospheric water vapor content, are small ($< 5cm$) compared to the deformation due to the earthquake. No good atmospheric model is available to correct for the propagation delays, and they are not considered further.

The topographic error is potentially important for this region because of the high elevation and rugged topography of the Longmen Shan coupled with the relatively long perpendicular baseline of ALOS. Artifact fringes introduced by the topography are directly proportional to the error in the elevation model. SRTM-3

has a spatial resolution of 90 m outside North America and the vertical accuracy varies from 5 m in relatively flat areas to perhaps as much as 50 m in extreme terrain such as the Longmen Shan where there are gaps in SRTM coverage. This topography error h maps into a LOS displacement error l according to the following formula

$$\frac{\partial l}{\partial h} = \frac{R_e B_{perp}}{\rho b sin\theta} \tag{2.1}$$

where R_e is the radius of the earth, B_{perp} is the perpendicular baseline, ρ is the range from the satellite to the topography, b is the orbital radius of the spacecraft, and θ is the look angle. Note that this error is independent of radar wavelength. Using parameters appropriate for PALSAR with a 34.3 ° look angle and a 400 m perpendicular baseline, the ratio of range change rate to height is 3.8×10^{-4}. Therefore a 50 m topography error produces a LOS error of 3.8 cm (a fraction of a fringe), which can have an effect on the interpretation of the interferograms especially near the rupture zone, where there are significant changes in elevation. Moreover several interferograms have baselines that are larger still and the baseline of the ScanSAR interferogram is from 657 to 844 m. In this case, the LOS errors due to topography are large enough to cause complete decorrelation of the interferograms in the highland area.

We suspect the clear stripe pattern in the northern part of the longer 475 track is associated with the ionospheric anomaly. Interestingly, this phase disturbances are more common on ascending orbits (10:30 PM) than on descending orbits (10:30 AM), which could be explained by the TEC decay in the nighttime. The plasma in the ionosphere can alter the refractive index and cause a frequency-dependent phase shift on microwave signals. The correspondent range shift is inversely proportional to the frequency thus it is 4 times larger at L-band than at C-band (*Meyer et al.*, 2006). We attempted, without much success, to account for the large-scale ionosphere effect using the TEC from Global Ionosphere Maps (`http://iono.jpl.nasa.gov/gim.html`) by removing a phase ramp from our interferograms with a single-layer model.

2.2.4 Extracting deformation from the phase data

As discussed above the large scale ionospheric and orbital errors produce phase ramps across the image that need to be removed before interpreting interferograms in terms of ground deformation. This trend estimation usually is performed after unwrapping the phase and simulaneously with model inversion. However, the decorrelation of the interferograms in mountains combined with shadowing and layover effect prevents a robust automatic phase unwrapping, especially in the areas of high phase gradient near the rupture (*Goldstein et al.*, 1988; *Goldstein and Werner*, 1998; *Zebker et al.*, 1994). In addition, much of the rupture zone is decorrelated so it is difficult to resolve the phase cycle ambiguity across the fault without counting fringes on adjacent swaths (Figure 2.2). The problem is complicated by the fact that different swaths have phase ramps that need to be estimated concurrently. To mitigate the unwrapping problems we digitize the fringes manually and converted them to displacement in the LOS direction. Each fringe represents 11.8 cm of LOS motion. Note that the spacing between fringes is inversely proportional to the local phase gradient so the digitized data will be naturally focused in areas of high displacement gradient (*Simons et al.*, 2002). Moreover, based on the a-posteriori misfit of the model to the data, we find that the RMS error is typically one fringe (11 cm) so digitizing at 1 fringe interval appears to be adequate.

We performed a two-stage digitization procedure to account for the ambiguity of phase steps across the fault and between neighboring swaths. Fringes furthest from the fault zone, representing the smallest LOS displacement were digitized first and we tracked toward the near-fault regions of very high phase gradient (Figure 2.2). We were able to count fringes in the partially decorrelated mountain region where automatic unwrapping scheme such as the Goldstein method doesn't work (*Goldstein et al.*, 1988; *Goldstein and Werner*, 1998; *Zebker et al.*, 1994). After generating a preliminary slip model with this digitized data set, we removed the model interferogram (projected into the range-dependent LOS) from each track and then flattend the residual phase by fitting a planar trend to the far-field signal (Table 2.1). This planar phase correction (utilizing 3 model parameters) applied

to each track dramatically improves the track-to-track continuity of fringes. These detrended interferograms were re-digitized and converted to the LOS displacement to form our final InSAR data set. It consists of 5738 digitized LOS displacements from two different look directions, 729 points from the descending track and 5009 points from the ascending tracks. Note that the spatial sampling of the digitizing along each fringe is finer than the fringe spacing so the data are not linearly independent. Figure 2.4 show significant and complex deformation along the strike of Longmen Shan fault zone. The spatial gradients of the LOS displacements in cross-fault direction reach at least 2×10^{-5} in interferograms from both the ascending and descending orbits. We complement the InSAR measurements with 109 GPS observations and geological scarp height measurements from filed studies to constrain the coseismic slip model over a wide range of length scales.

2.3 Inversion for the coseismic slip model

We used the geologically mapped surface rupture and aftershock distribution to approximate the earthquake fault with four planar subfaults with different strike and dip angles. We used a relationship between slip on a fault patch and surface displacement assuming a homogeneous elastic half-space approximation (*Okada*, 1985; *Fialko*, 2004). The fault was parameterized using 280 patches (560 strike- and dip- slip components). The forward matrix relating slip on each patch to the observations consists of both the Greens functions and smoothing matrix. The observation vectors d_{LOS} and d_{GPS} consist of the InSAR data, which are the LOS displacement from the ascending and descending tracks, and the GPS data with east-north-up displacement components. The model vectors m_{dip} and m_{strike} represent dip-slip and strike-slip components on discrete fault patches. The Greens functions for the full vector field are calculated given a prior fault parameterization, and are subsequently projected into LOS direction,

$$\begin{bmatrix} G_{LOS} \\ G_{GPS} \\ \lambda S \end{bmatrix} \times \begin{bmatrix} m_{dip} \\ m_{strike} \end{bmatrix} = \begin{bmatrix} d_{LOS} \\ d_{GPS} \\ 0 \end{bmatrix} \tag{2.2}$$

The regularization (smoothness) constraint minimizes the first derivative of slip as approximated by a finite difference quadrature (*Fialko*, 2004) (See Eq. (1.3)). Parameter λ in Eq. (1.2) is the weight of smoothing chosen based on a number of simulations to obtain the smoothest model that does not degrade the fit to the data.

$$S = \begin{pmatrix} 1 & -1 & 0 & 0 & \cdots \\ 0 & 1 & -1 & 0 & \cdots \\ \vdots & \vdots & \vdots & \ddots & \cdots \\ 0 & 0 & \cdots & 1 & -1 \end{pmatrix} \tag{2.3}$$

2.3.1 Model settings: fault geometry and parameters

The fault geometry is based on geological mapping of the surface rupture (*Liu-Zeng et al.*, 2009) and the relocation of aftershocks (*Huang et al.*, 2008). We use three rectangular fault segments to approximate the Beichuan fault and one segment to approximate the southern part of the Pengguan fault (also referred to as the Gian Xian-An Xian fault). Each segment is further discretized into slip patches. In the top row slip patches are 4 km long and 2 km wide. The width of the patches increases progressively with depth by a factor of 1.5 (Figure 2.5) to maintain a uniform model resolution. While the surface trace of the fault is straightforward to define based on field mapping and SAR data, the dip angles of the fault segments are more difficult to determine. After testing the sensitivity of the RMS of the residuals to the overall fault dip with help of a grid search method (Figure 2.6), we found that the available data are consistent with the fault dip within a wide range of 40° to 60° . We note that the seismicity is not localized on a narrow fault plane, which may reflect the complex fault geometry at depth in this region. To account for a possibility of a spatially variable dip angle, we solve for the dip angles of each segment separately using the grid search method (See

Figure 2.6 for details). The best-fit model has fault planes that rotate from shallow dip in the south (35°) to nearly vertical dip toward the north (70°). This result is in a general agreement with the relocated aftershocks. After several iterations, we fix the fault geometry before final inversion for slip on each patch (Table 2.2). The inversion requires subsurface slip well beyond the ends of the surface rupture on the Beichuan Fault and Pengguan Fault segments. The maximum depth of each fault plane was limited to 25km, which corresponds to the depth extent of aftershocks; deeper slip is not required by the InSAR and GPS data.

2.3.2 Topographic effect

The Wenchuan earthquake occurred along the steepest topographic gradient of the Longmen Shan thrust belt (Figure 2.1). The mountains to the northwest are on average 3 km higher than the Sichuan Basin to the southeast at 500 m elevation. This elevation contrast is sufficiently large that we need to take it into account in our inversion. In modeling the topographic effects, we set 500 m above from sea level as the reference (free surface of the half space) and modify the Greens functions according to the elevation of each data point. For points above this level the effective depth of slip patches was increased when calculating the surface displacement. This first-order correction improved fit to the InSAR data on the hanging wall side of the fault.

2.3.3 Incidence angle

The incidence angle in radar interferograms varies smoothly from 16.8° to 44.1° along descending tracks and from 36.8° to 41.4° along ascending tracks. We utilize precise orbit data to calculate the unit look vectors in a global Cartesian coordinate system for each InSAR ground point measurement and then convert them into local east-north-up coordinates using rotation matrix (*Price and Sandwell*, 1998). This information is needed for the inversion matrix. The observation vectors are given by

$$d_{LOS} = \begin{bmatrix} d_E & d_N & d_V \end{bmatrix} \begin{bmatrix} n_E \\ n_N \\ n_V \end{bmatrix} \tag{2.4}$$

where d_{LOS} is the displacement in LOS direction; d_E , d_N , d_V are displacements in east, north, and up respectively; n_E , n_N, n_V are three component of the unit look vectors.

2.3.4 Joint inversion

After applying weights on different data types according to the measurement errors in Eq. (1.2), terms in the combined the linear system of equations to be solved are

$$A = \begin{bmatrix} \sigma_{LOS}^{-1} G_{LOS} \\ \beta \sigma_{GPS}^{-1} G_{GPS} \\ \lambda S \end{bmatrix}, b = \begin{bmatrix} \sigma_{LOS}^{-1} d_{LOS} \\ \beta \sigma_{GPS}^{-1} d_{GPS} \\ 0 \end{bmatrix}, m = \begin{bmatrix} m_{dip} \\ m_{strike} \end{bmatrix} \tag{2.5}$$

where σ_{LOS} and σ_{GPS} are two diagonal matrices derived from measurement uncertainties, and β represents the relative weight of InSAR and GPS data sets . We minimize the misfit between the data and the model prediction in a least square sense subject to two types of constraints: the first one is the positivity constraint prohibiting normal and left-lateral slip on the fault. The positivity constraint prevents unphysical Checker boarding patterns. As shown in Figure 2.5, the positivity constraint on strike-slip is mostly redundant (see discussion below). The second constraint is invoked to satisfy the field data on scarp height along the fault,

$$\begin{aligned} & min \| \, Am - b \, \|^2 \\ & m_{dip} \geq 0, m_{strike} \leq 0, Cm \geq s \\ & C = G_{hanging} - G_{foot} \end{aligned} \tag{2.6}$$

where s is the selected scarp height measurements on the surface rupture from geological survey, C is the Greens function for the surface throw on the fault, which is the difference in dip-slip displacements between the hanging wall

and the footwall. The scarp height might be underestimated due to the presence of secondary faulting thus we take the geologically measured scarp height as a lower bound. In other words, we added an inequality constraint that requires the model prediction of scarp height to be greater than the geologic observations. Equation (1.6) is a specific expression of the typical least squares problem with none-negative constraint (NNLS) (*Lawson and Hanson*, 1995) that has numerically stable solutions (*Parker*, 1994).

Calculated surface displacements are based on an elastic, isotropic and homogeneous half-space model. The Poisson ratio is taken to be 0.25. We used the tradeoff curve between model smoothness and normalized RMS misfit to define optimal smoothness parameter. The relative weight between InSAR and GPS data sets is adjusted iteratively, and then fixed when the misfit reaches the minimum. Our best-fitting model based on three independent data sets can explain both InSAR and GPS measurements reasonably well and results in a variance reduction of 93%.

Figure 2.4 shows that the residuals between InSAR data and the model predictions (ascending interferograms: mean 2.30 cm, standard deviation 12.41 cm; descending interferograms: mean -1.52 cm, standard deviation 10.20 cm). The greater near-fault residuals might be due to a combination of complicated near-field deformation, early postseismic deformation, oversimplified fault geometry, and material heterogeneity. The same model also provides a good fit to the GPS observations (Figure 2.7 and Figure 2.8). The RMS of the residuals is 4.93 cm for north component; 11.78 cm for east component; 6.75 cm for vertical component. Finally the model provides a good match to the observed scarp height along the fault (See Figure 2.9). Figure 2.9 shows that the calculated vertical offsets along the Beichuan and Pengguan faults correlate well with the geologic measurements. The fault throw varies along strike with peaks near Beichuan and Wenchuan areas, which suggests that the modeled coseismic slip in the shallow layers agrees with the geological observations. The magnitude of vertical displacement is also affected by fault dip angle at shallow depth, and the along-strike variation of vertical offsets could thus partially been due to change in fault dip along strike. We didnt use

the geologic lateral offset data in the inversions because the former are subject to larger bias (*Liu-Zeng et al.*, 2009).

2.4 Resolution tests

We conducted a set of synthetic checkerboard tests to assess qualitatively the model resolution (Figure 2.10). After visually examining and comparing corresponding slip features of the checkerboard test results; we found that the slip partitioning between Beichuan and Pengguan faults is not well-constrained since there are no geodetic data available to distinguish slip motion between the two parallel faults. Nevertheless, this test gives confirmation to the shallow slip in our final model. We also found that descending interferogram has great importance in resolving spatially variable slip distributions. GPS-only based inversions result in poorer resolution of the coseismic slip model than InSAR data in that the surface displacement measurements provided by GPS have wider spacing than InSAR. In the case of the final inversion, GPS dataset is generally compatible with our InSAR dataset.

We generated the synthetic InSAR and GPS data caused by an artificial slip model, while retaining all the parameter settings as were used in making final model. Different faulting types are tested, including right-lateral strike-slip fault, thrust fault, and a combination of these two. The slip magnitude in this checkerboard test were set to be uniform (5m), then we inverted these data to see how well the features are resolved. The smoothness was adjusted accordingly.

We also tested the resolution on slip depth for 3 cases: 2 km, 9 km, 20 km in width of the fault. We generated a uniform slip (5 m dextral strike-slip, 5 m reverse dip-slip) localized in those depth, and inverted the synthetic InSAR and GPS data to see whether this slip depth is resolved. The result shows that the resolving power with respect to slip depth is generally good. It is resolved with an error of one depth layer or less, except for the area where two parallel fault interfere with each other. This test confirms the shallow slip feature we found in our final slip model.

2.5 Results and discussion

The total geodetic moment inferred from our best-fitting model is $6.79 \times 10^{20} Nm$ (equivalent to earthquake moment magnitude of 7.8), in general agreement with the 7.9 moment magnitude (seismic moment of $7.6 \times 10^{20} Nm$) from U.S. Geological Survey. The geodetic moment is taken to be the vector sum of the strike-slip ($3.61 \times 10^{20} Nm$) and dip-slip ($4.96 \times 10^{20} Nm$) components, which are nearly equally partitioned. Caution should be exercised when interpreting the estimated geodetic moment. Firstly, to achieve a realistic geodetic moment, it involves estimating the area of rupture, the associated static slip and the shear modulus to a sufficient accuracy. Secondly, this geodetic moment should not be confused with the seismic moment because aseismic slip could take place after the dynamic rupture process and alter the final static deformation field.

The coseismic slip model (Figure 2.5 and Figure 2.11) based on a joint inversion of InSAR and GPS data shows the complex spatial variation in both depth and rake along the two major fault strands. The inferred subsurface rupture length is 304 km, which is consistent with the 316 km long distribution of aftershocks. On the Beichuan fault, the faulting in the epicentral area is dominated by a thrust component (5 to 13 m) and the major rupture extends down to depth of 10 km. The rupture progressively changed to strike-slip as it propagated northeast. In its middle segment, the slip is shallower (8 km) and the amount of right-lateral strike-slip and thrust are nearly equal (5 to 10 m for each component). On average, slip on the Beichuan fault extends to greater depth (12 km) toward the northern end and is mainly right-lateral strike-slip (2 to 7 m). The Pengguan fault, which runs parallel to the Beichuan fault, is inferred to have dominantly thrust slip (<12 m) at very shallow depth (see Table 2.3 for detailed summary). Figure 2.5 shows that the coseismic slip on the fault planes was heterogeneous along the strike: the thrust motion on the Beichuan fault concentrated near surface at a distance of 160, 210 and 260 km from the northeast end of the modeled fault plane. The dip-slip reached more than 10 m in those high slip areas (Figure 2.5b). The right-lateral strike-slip was mainly distributed in the northern part of the Beichuan fault near surface, at a distance of 50 to 100 km from the northeastern tip, with a magnitude

varying from 4 to 7 m. There is a slight increase in strike-slip at a distance of 160 km in the middle segment of Beichuan fault (See Figure 2.5c). Comparing these slip patterns with the reported damage distribution lends further support to the best-fitting model. The high slip areas correlate spatially with the two devastated regions in the Longmen Shan fault zone: one is about 260 km along the Beichuan fault (to the northeast of the epicenter area), corresponding to the Wenchuan county, and the other is about 160 km along the Beichuan fault, corresponding to the Beichuan county.

We compared other available coseismic slip models with our best-fitting model. Our model is in general agreement with the teleseismic inversion suggesting that the earthquake involved both thrust and right-lateral strike-slip (*Ji and Hayes*, 2008). One major difference is that the teleseismic inversion didnt show a significant amount of shallow (depth less than 5-8 km) slip. Teleseismic inversions have poor depth resolution, especially within the upper crust, in contrast to the spatially dense geodetic data. Both our model and the bi-fault model (*Hao et al.*, 2009), which is based on ascending interferograms only, indicate large thrust at YingXiu, Houshenggou and Bajiaomiao on southern Beichuan fault, and dominant right-lateral strike-slip at Pingtong and Nanba on northern Beichuan fault (Figure 2.5). In contrast, our joint-inversion shows that the large-amplitude thrust near the epicentral area is shallower and the thrust component on the Pengguan fault is larger. The descending track interferograms and the GPS data resolved the ambiguity in the combined horizontal and vertical motion caused by single radar look direction.

Resolving the slip partitioning between the parallel fault strands is difficult given their proximity and the fact that the interferograms are completely decorrelated in the near field, presumably due to extreme ground-shaking and high strain. The estimated slip on the Pengguan fault is less robust due to the ambiguity in this slip partitioning (Figure 2.5). On one hand, imposing the positivity constraint on strike-slip direction is largely redundant because the data are adequate to constrain the overall sense of motion. Relaxing the positivity constraint on strike-slip results in only two small areas on the Pengguan fault and southern end of middle

Beichuan fault where the slip becomes left-lateral. On the other hand, such a reversal suggests that this part of the model is less well resolved. An additional complexity is the Xiaoyudong fault (a cross-fault) near the epicentral region reported to have thrust slip of 1m and left-lateral strike-slip of 1m at the surface. Unfortunately, there is no available geodetic data close enough to the fault zone to resolve the motion on this cross-fault. We decide not to use this cross fault after carrying out a resolution test on several different fault models. The deformation gradient near the surface rupture is very high as indicated by the tightly packed phase fringes close to the faults. As shown in Figure 2.4 and Figure 2.8, our best-fitting model somewhat underestimates the deformation on the footwall. In Figure 2.4, there are positive residuals as high as 15 cm narrowly distributed along the fault. Similarly in Figure 2.8, the asymmetry of the histograms reveals that there is more subsidence on the footwall than predicted. This systematic misfit might be due to a combination of complicated near-field deformation, postseismic deformation, and oversimplified fault geometry.

We performed a series of checkerboard tests to investigate the spatial resolution of our inversions. As anticipated, the slip distribution inferred from geodetic data has better resolution at shallow depth. Figure 2.12 shows the slip versus depth profile for each fault segment along with the aftershocks. An interesting inference is that the slip magnitude decreases rapidly with depth and is concentrated in the upper 10km of the crust. We tested the robustness of the model by altering top patch size (from 4km by 8km to 1km by 2km), and perturbing the smoothing and weighting parameters. The depth distribution of seismic potency is similar to that of total slip magnitude in different fault discretization schemes. The depth-dependent slip showed stable and consistent characteristic throughout the inversions. Judging by the depth where slip drops to half of its maximum, the four fault segments behave differently. The slip is shallower in the central segment of Beichuan fault (8 km) and is deeper toward both ends. The rupture on Pengguan fault is extremely shallow, on average at depth of 3 to 4 km, which can be explained by the imbricate fault geometry showing that the Pengguan fault intersects and converges with Beichuan fault at depth (*Hubbard and Shaw*, 2009).

Although the shallowest part of the rupture is not well constrained due to decorrelation on the hanging wall near the fault, the slip distribution shown in Figure 10 appear to be qualitatively different from the slip distribution of well-imaged magnitude 7 strike-slip earthquakes characterized by the so-called shallow slip deficit (*Simons et al.*, 2002; *Fialko et al.*, 2005). One possibility is that great earthquakes on mature faults are qualitatively different from smaller earthquakes on immature or infrequently slipping faults in that the former are able to drive slip in the shallow velocity strengthening part of the brittle layer (*Tse and Rice*, 1986; *Marone*, 1998; *Fialko*, 2004). The slip versus depth profile (shown in Figure 2.12) provides insight into the long-term strain accumulation on the Longmen Shan fault. Comparing this coseismic model with intererseismic and postseismic slip models may shed light on fault behavior throughout the earthquake cycle. An alternative explanation for the prominent shallow slip in the Wenchuan earthquake is that the continental thrust events are different in rupture mode compared to the continental strike-slip events. The geodetic and seismic inversion of the Kashmir 2005 earthquake (Mw 7.6 thrusting event) showed similar kind of behavior as the Wenchuan earthquake: the slip mainly occurred in the upper 10 km of the crust (*Avouac et al.*, 2006; *Pathier et al.*, 2006).

The relocated aftershocks mostly occurred at depth between 10 km and 20 km where the coseismic slip decays considerably (Figure 2.12). The seismicity vanishes below 25 km. As one can gather from Figure 2.11, the aftershocks appear to be distributed on the periphery of the area of high slip. This pattern has been observed in previous studies of significant earthquakes, such as the 2004 Bam earthquake (*Funning et al.*, 2005; *Tatar et al.*, 2005), 2007 Nias-Simeulue earthquake (*Hsu et al.*, 2006) and 2004 Parkfield earthquake (*Johanson et al.*, 2006; *Thurber et al.*, 2006; *Barbot et al.*, 2009).

2.6 Conclusions

A coseismic slip model for the 2008 Wenchuan Earthquake has been developed based on a combination of line of sight displacement from 41 (39 normal

mode ascending and 2 ScanSAR - ScanSAR descending) ALOS interferograms, 109 GPS displacement vectors and geologic scarp height measurements. Our InSAR data provided a nearly complete coverage of the surface deformation along both ascending and descending orbits. Our best-fitting model suggests the geodetic moment of $6.79 \times 10^{20} Nm$, in gerneral agreement with the seismic moment ($7.6 \times 10^{20} Nm$). Fault motion was nearly equally partitioned between dip-slip and right-lateral strike-slip. The slip was mostly thrust in the southern segment of the Beichuan fault; then the rupture progressively changed to right-lateral strike-slip as it propagated northeast. Our inversions suggest that the slip magnitude decreased with depth and concentrated in the upper 10 km of the crust. The aftershocks of the Wenchuan earthquake primarily occurred below the area of coseismic slip.

References

Avouac, J.-P., F. Ayoub, S. Leprince, O. Konca, and D. V. Helmberger (2006), The 2005 M7.6 Kashmir earthquake: Sub-pixel correlation of aster images and seismic waveforms analysis, *Earth and Planetary Science Letters*, *249*(3), 514–528.

Barbot, S., Y. Fialko, and Y. Bock (2009), Postseismic deformation due to the Mw 6.0 2004 Parkfield earthquake: Stress-driven creep on a fault with spatially variable rate-and-state friction parameters, *Journal of Geophysical Research*, *114*(B7), B07,405.

Burchfiel, B., et al. (2008), A geological and geophysical context for the Wenchuan earthquake of 12 May 2008, Sichuan, People's Republic of China, *GSA Today*.

Chen, Z., B. Burchfiel, Y. Liu, R. King, L. Royden, W. Tang, E. Wang, J. Zhao, and X. Zhang (2000), Global Positioning System measurements from eastern Tibet and their implications for India/Eurasia intercontinental deformation, *Journal of Geophysical Research*, *105*, 16,215–16,228.

Delouis, B., D. Giardini, P. Lundgren, and J. Salichon (2002), Joint inversion of InSAR, GPS, teleseismic, and strong-motion data for the spatial and temporal distribution of earthquake slip: application to the 1999 Izmit mainshock, *Bulletin of the Seismological Society of America*, *92*(1), 278–299.

Densmore, A. L., M. A. Ellis, Y. Li, R. Zhou, G. S. Hancock, and N. Richardson (2007), Active tectonics of the Beichuan and Pengguan faults at the eastern margin of the Tibetan plateau, *Tectonics*, *26*(4), TC4005.

Farr, T. G., et al. (2007), The shuttle radar topography mission, *Reviews of Geophysics*, *45*(2), RG2004.

Fialko, Y. (2004), Evidence of fluid-filled upper crust from observations of post-seismic deformation due to the 1992 Mw7. 3 Landers earthquake, *Journal of geophysical research*, *109*(B8), B08,401.

Fialko, Y., M. Simons, D. Agnew, et al. (2001), The complete (3-D) surface displacement field in the epicentral area of the 1999 Mw 7.1 Hector Mine earthquake, California, from space geodetic observations, *Geophys. Res. Lett*, *28*(16), 3063–3066.

Fialko, Y., D. Sandwell, M. Simons, and P. Rosen (2005), Three-dimensional deformation caused by the Bam, Iran, earthquake and the origin of shallow slip deficit, *Nature*, *435*(7040), 295–299.

Funning, G. J., B. Parsons, T. J. Wright, J. A. Jackson, and E. J. Fielding (2005), Surface displacements and source parameters of the 2003 Bam (Iran) earthquake from ENVISAT advanced synthetic aperture radar imagery, *Journal of Geophysical Research*, *110*(B9), B09,406.

Goldstein, R., H. Zebker, and C. Werner (1988), Satellite radar interferometry-two-dimensional phase unwrapping, *Radio Science*, *23*(4), 713–720.

Goldstein, R. M., and C. L. Werner (1998), Radar interferogram filtering for geophysical applications, *Geophysical Research Letters*, *25*(21), 4035–4038.

Hao, K. X., H. Si, H. Fujiwara, and T. Ozawa (2009), Coseismic surface-ruptures and crustal deformations of the 2008 Wenchuan earthquake Mw7. 9, China, *Geophysical Research Letters*, *36*(11), L11,303.

Hearn, E. H., R. Bürgmann, and R. E. Reilinger (2002), Dynamics of Izmit earthquake postseismic deformation and loading of the Düzce earthquake hypocenter, *Bulletin of the Seismological Society of America*, *92*(1), 172–193.

Hernandez, B., F. Cotton, and M. Campillo (1999), Contribution of radar interferometry to a two-step inversion of the kinematic process of the 1992 Landers earthquake, *Journal of Geophysical Research*, *104*(B6), 13,083–13.

Hsu, Y.-J., M. Simons, J.-P. Avouac, J. Galetzka, K. Sieh, M. Chlieh, D. Natawidjaja, L. Prawirodirdjo, and Y. Bock (2006), Frictional afterslip following the 2005 Nias-Simeulue earthquake, Sumatra, *Science*, *312*(5782), 1921–1926.

Huang, Y., J. Wu, T. Zhang, and D. Zhang (2008), Relocation of the M8. 0 Wenchuan earthquake and its aftershock sequence, *Science in China Series D: Earth Sciences*, *51*(12), 1703–1711.

Hubbard, J., and J. H. Shaw (2009), Uplift of the Longmen shan and Tibetan plateau, and the 2008 Wenchuan (M= 7.9) earthquake, *Nature*, *458*(7235), 194–197.

Ji, C., and G. Hayes (2008), Finite fault model-preliminary result of the May 12, 2008 Mw 7.9 eastern Sichuan, China earthquake, *US Geological Survey National Earthquake Center*.

Johanson, I. A., E. J. Fielding, F. Rolandone, and R. Bürgmann (2006), Coseismic and postseismic slip of the 2004 Parkfield earthquake from space-geodetic data, *Bulletin of the Seismological Society of America*, *96*(4B), S269–S282.

King, G. C., R. S. Stein, and J. Lin (1994), Static stress changes and the triggering of earthquakes, *Bulletin of the Seismological Society of America*, *84*(3), 935–953.

Kirby, E., K. X. Whipple, W. Tang, and Z. Chen (2003), Distribution of active rock uplift along the eastern margin of the Tibetan plateau: Inferences from bedrock channel longitudinal profiles, *Journal of Geophysical Research*, *108*(B4), 2217.

Kobayashi, T., Y. Takada, M. Furuya, and M. Murakami (2009), Locations and types of ruptures involved in the 2008 Sichuan earthquake inferred from SAR image matching, *Geophysical research letters*, *36*(7), L07,302.

Lawson, C. L., and R. J. Hanson (1995), *Solving least squares problems*, vol. 15, SIAM.

Liu-Zeng, J., et al. (2009), Co-seismic ruptures of the 12 May 2008, Ms 8.0 Wenchuan earthquake, Sichuan: East-west crustal shortening on oblique, parallel thrusts along the eastern edge of Tibet, *Earth and Planetary Science Letters*, *286*, 355–370.

Marone, C. (1998), Laboratory-derived friction laws and their application to seismic faulting, *Annual Review of Earth and Planetary Sciences*, *26*(1), 643–696.

Massonnet, D., and K. L. Feigl (1998), Radar interferometry and its application to changes in the earth's surface, *Reviews of geophysics*, *36*(4), 441–500.

Meyer, F., R. Bamler, N. Jakowski, and T. Fritz (2006), The potential of low-frequency SAR systems for mapping ionospheric TEC distributions, *Geoscience and Remote Sensing Letters, IEEE*, *3*(4), 560–564.

Crustal Motion Observation Network of China Project, W. G. (2008), The coseismic displacement of 2008 Wenchuan Ms8.0 earthquake measured by GPS (in chinese), *Science in China Series D: Earth Sciences*, *38*(10), 1195–1206.

Okada, Y. (1985), Surface deformation due to shear and tensile faults in a half-space, *Bulletin of the seismological society of America*, *75*(4), 1135–1154.

Parker, R. L. (1994), *Geophysical inverse theory*, Princeton University Press.

Pathier, E., E. Fielding, T. Wright, R. Walker, B. Parsons, and S. Hensley (2006), Displacement field and slip distribution of the 2005 Kashmir earthquake from SAR imagery, *Geophys. Res. Lett*, *33*(20), L20,310.

Perfettini, H., and J.-P. Avouac (2007), Modeling afterslip and aftershocks following the 1992 Landers earthquake, *Journal of Geophysical Research*, *112*(B7), B07,409.

Pollitz, F. F., G. Peltzer, and R. Bürgmann (2000), Mobility of continental mantle: Evidence from postseismic geodetic observations following the 1992 Landers earthquake, *Journal of Geophysical Research*, *105*(B4), 8035–8054.

Price, E. J., and D. T. Sandwell (1998), Small-scale deformations associated with the 1992 Landers, California, earthquake mapped by synthetic aperture radar interferometry phase gradients, *Journal of Geophysical Research*, *103*(11), 27,001–27,016.

Rosenqvist, A., M. Shimada, N. Ito, and M. Watanabe (2007), ALOS PALSAR: A pathfinder mission for global-scale monitoring of the environment, *Geoscience and Remote Sensing, IEEE Transactions on*, *45*(11), 3307–3316.

Sandwell, D. T., L. Sichoix, and B. Smith (2002), The 1999 Hector Mine earthquake, southern California: Vector near-field displacements from ERS InSAR, *Bulletin of the Seismological Society of America*, *92*(4), 1341–1354.

Sandwell, D. T., D. Myer, R. Mellors, M. Shimada, B. Brooks, and J. Foster (2008), Accuracy and resolution of ALOS interferometry: Vector deformation maps of the Father's day intrusion at Kilauea, *Geoscience and Remote Sensing, IEEE Transactions on*, *46*(11), 3524–3534.

Simons, M., Y. Fialko, and L. Rivera (2002), Coseismic deformation from the 1999 Mw 7.1 Hector Mine, California, earthquake as inferred from InSAR and GPS observations, *Bulletin of the Seismological Society of America*, *92*(4), 1390–1402.

Tatar, M., D. Hatzfeld, A. Moradi, and A. Paul (2005), The 2003 December 26 Bam earthquake (iran), Mw 6.6, aftershock sequence, *Geophysical Journal International*, *163*(1), 90–105.

Thurber, C., H. Zhang, F. Waldhauser, J. Hardebeck, A. Michael, and D. Eberhart-Phillips (2006), Three-dimensional compressional wavespeed model, earthquake relocations, and focal mechanisms for the Parkfield, California, region, *Bulletin of the Seismological Society of America*, *96*(4B), S38–S49.

Tong, X., D. Sandwell, Y. Fialko, and R. Mellors (2008), Coseismic displacement of M8. 0 Sichuan earthquake derived by ALOS radar interferometry, in *AGU Fall Meeting Abstracts*, vol. 1, p. 0715.

Tse, S. T., and J. R. Rice (1986), Crustal earthquake instability in relation to the depth variation of frictional slip properties, *J. geophys. Res*, *91*(B9), 9452–9472.

Zebker, H. A., P. A. Rosen, R. M. Goldstein, A. Gabriel, and C. L. Werner (1994), On the derivation of coseismic displacement fields using differential radar interferometry: The Landers earthquake, *Journal of Geophysical Research*, *99*(B10), 19,617–19.

Table 2.1: Acquisition dates, perpendicular baselines and planar phase for each Interferometry tracks.

track	acquisition dates	perpendicular baseline	planar phase removed		
			Sx	Sy	Dc Value
471	Feb/29/2008 May/31/2008	93.2	-15	-15	4.79
472	Jan/28/2008 Jun/17/2008	211.6	6	12	-2.66
473	Feb/17/2008 May/19/2008	229.5	-6	0	2.13
474	Mar/5/2008 Jun/5/2008	290.7	0	0	1.06
475	Jun/20/2007 Jun/22/2008	68.4	-3	-6	-1.06
476	Apr/8/2008 May/24/2008	207.0	-3	-4	-6.39
124	Jan/3/2008 May/20/2008	844.04	0	5	3.19

Table 2.2: Modeled fault geometry and their geographic locations.

fault index	lon	lat	strike	dip	length(km)
1	105.26	32.49	-128.41	70	95.74
2	104.31	31.71	-136.84	50	154.82
3	103.40	30.95	-128.43	35	87.60
4	104.08	31.38	-137.03	25	82.07

Table 2.3: Description of the best-fitting coseismic slip model.

fault plane index	fault segment	maximum total slip amplitude (m)	maximum slip depth (km)	average slip depth (km)
1	northern Beichuan	7	23	12
2	middle Beichuan	12	22	8
3	southern Beichuan	13	21	10
4	Pengguan	12	7	3.5

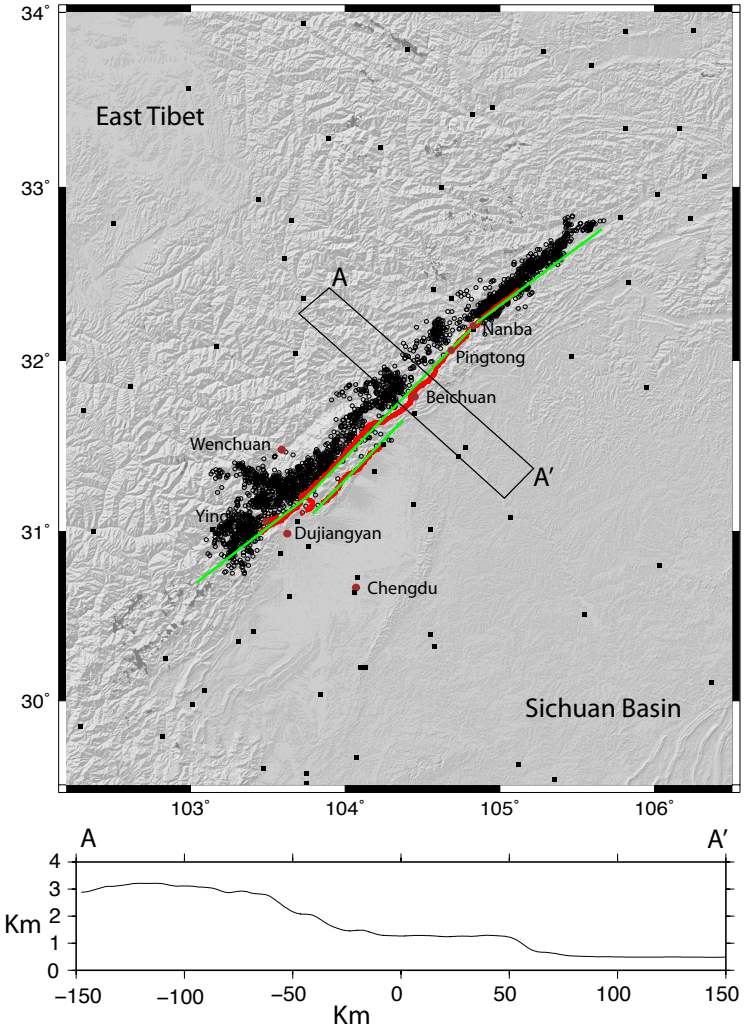

Figure 2.1: Shaded topography in the Longmen Shan area. The black circles are 2706 relocated aftershocks ($M > 2.0$) following the mainshock by the end of July 8th 2008. The red line is the surface rupture from geological survey. The green lines indicate four segments of simplified faults used in the inversion. The black squares show the deployed GPS receivers. The subplot shows the filtered topographic step across Longmen Shan fault zone.

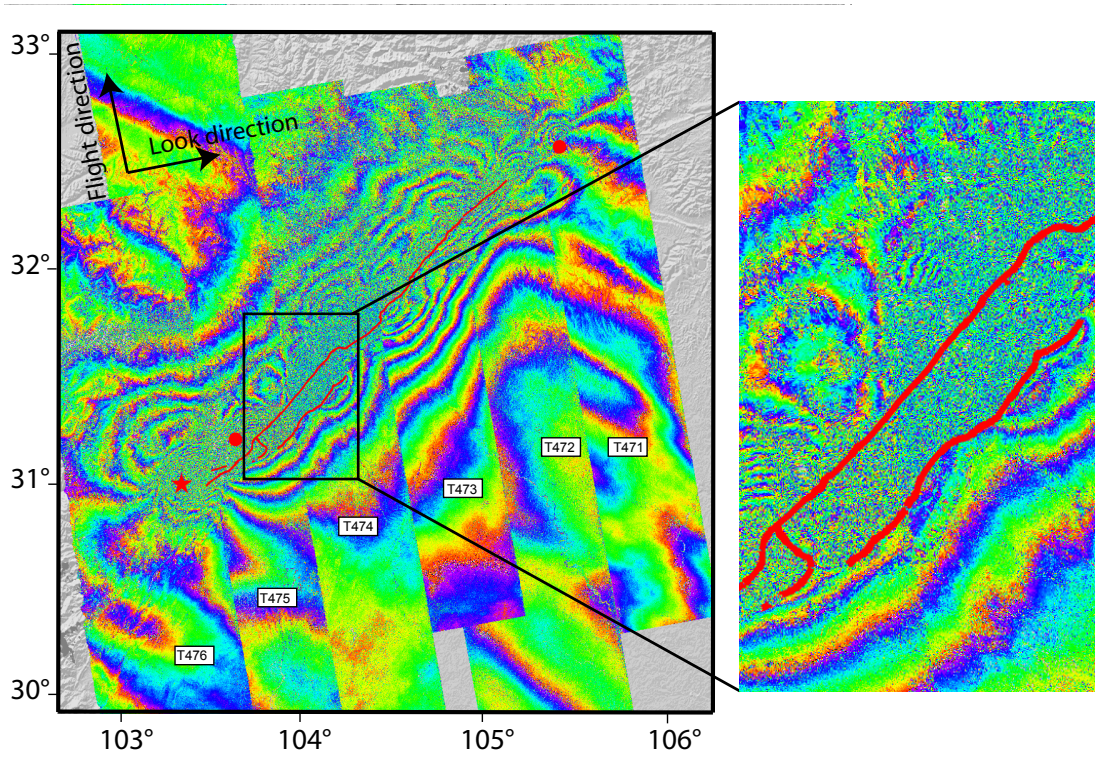

Figure 2.2: Ascending swath mode interferograms after trend removal (Six tracks). The color scale shows the wrapped phase that corresponds to the range change (11.8 cm per fringe) between the ground points to the radar antenna. Phase increase corresponds to range increase; and vice versa. The red star is the main-shock and the two red dots are two M6.0 aftershocks. The red line is the surface rupture from geological survey. A zoom-in view demonstrates the fine phase fringes on the hanging wall that are manually digitized.

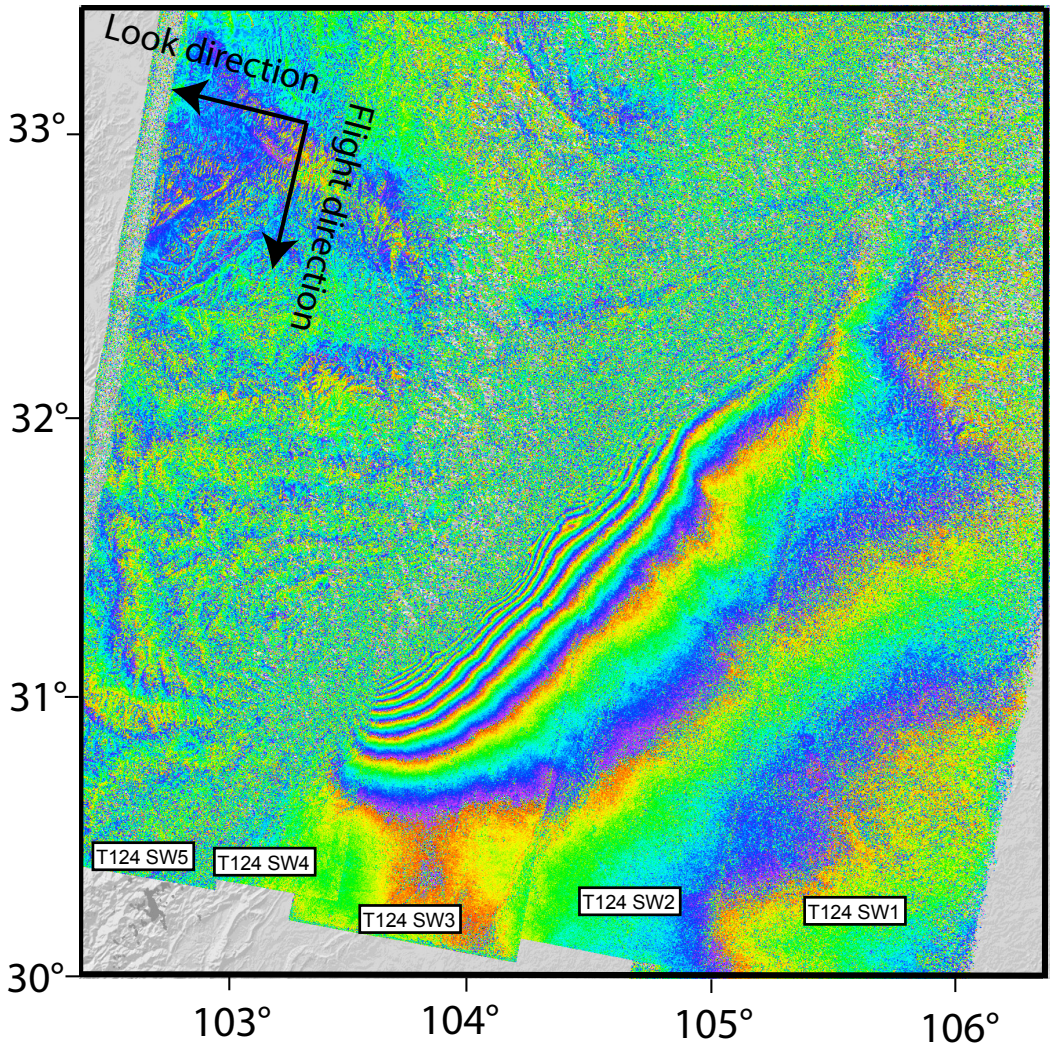

Figure 2.3: Descending ScanSAR mode interferograms after trend removal (11.8 cm per fringe). Each scene of the interferogram consists of 5 sub-swaths across look direction. The decorrelation in the mountainous area is probably due to long perpendicular baseline (657 $\sim$ 844 m). The phase change has the same sign as the range change, in the same convention as in Figure 2.2.

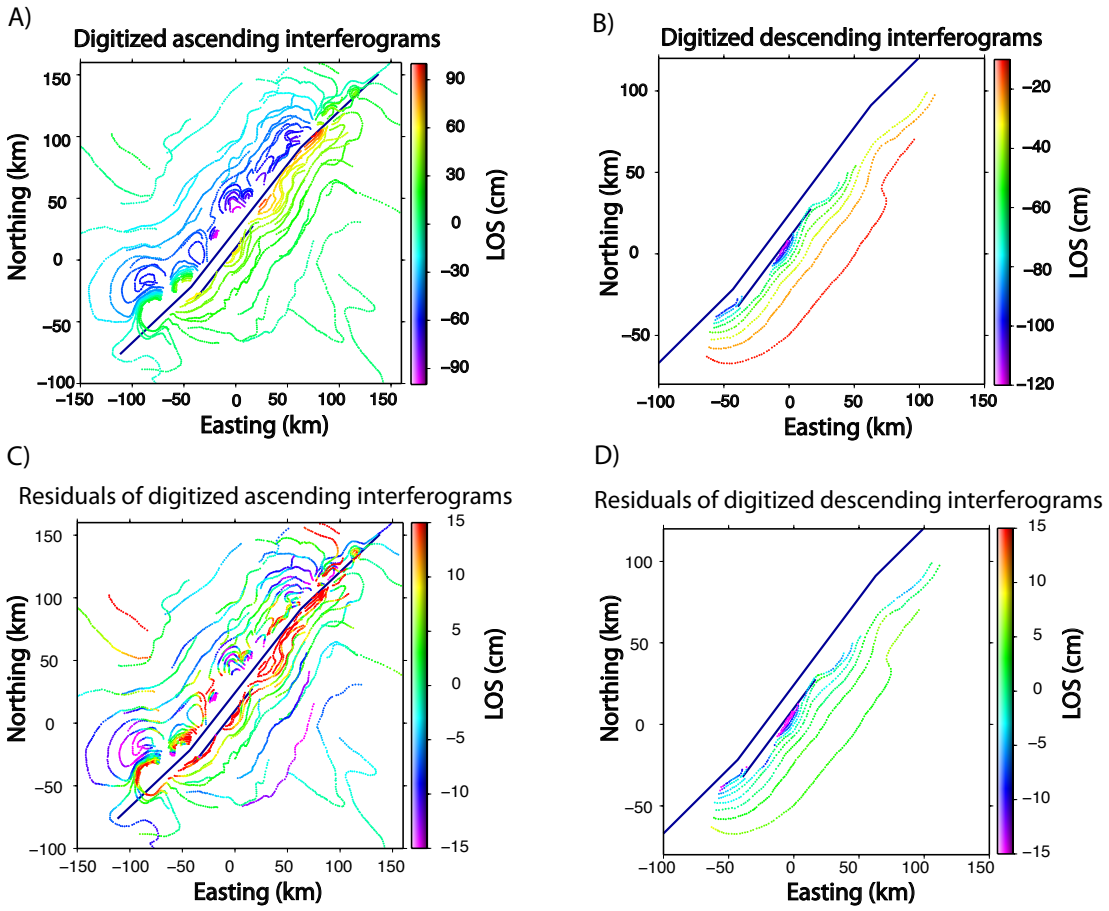

Figure 2.4: a) b) show digitized InSAR data in map view. Each line of dots represents the digitized fringes with an integer phase value in the interferograms. The color represents the line-of-sight (LOS) displacement. c) d) show the model residuals. Positive LOS displacement represents decrease in the distance from ground scatters to the radar; negative LOS displacement represents increase in the distance from ground scatters to the radar. Note the LOS displacement is a combination of the horizontal and vertical components.

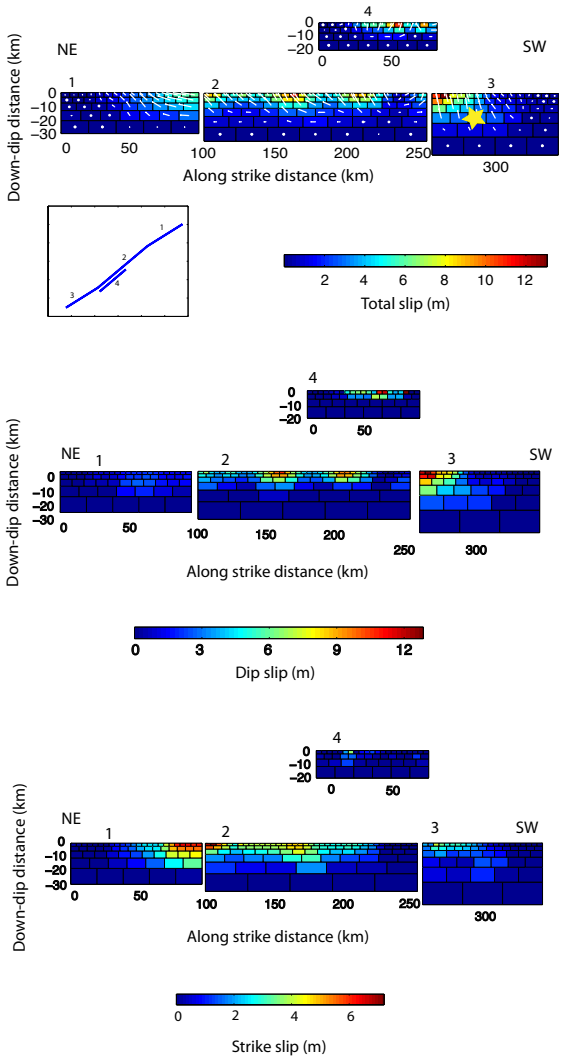

Figure 2.5: a) Coseismic slip model. The faults are located as shown in the inset map. The color represents the total slip magnitude on fault patches. The white lines, which originate from center of the rectangular patches and point outward, illustrate the relative motion of the hanging wall with respect to footwall. (thrust slip and right-lateral strike-slip in this case.) The yellow star is the mainshock. b) The dip-slip magnitude. Note the diminished dip-slip on the southern end of middle Beichuan fault is less robust due to ambiguity in the slip partitioning. c) The strike-slip magnitude.

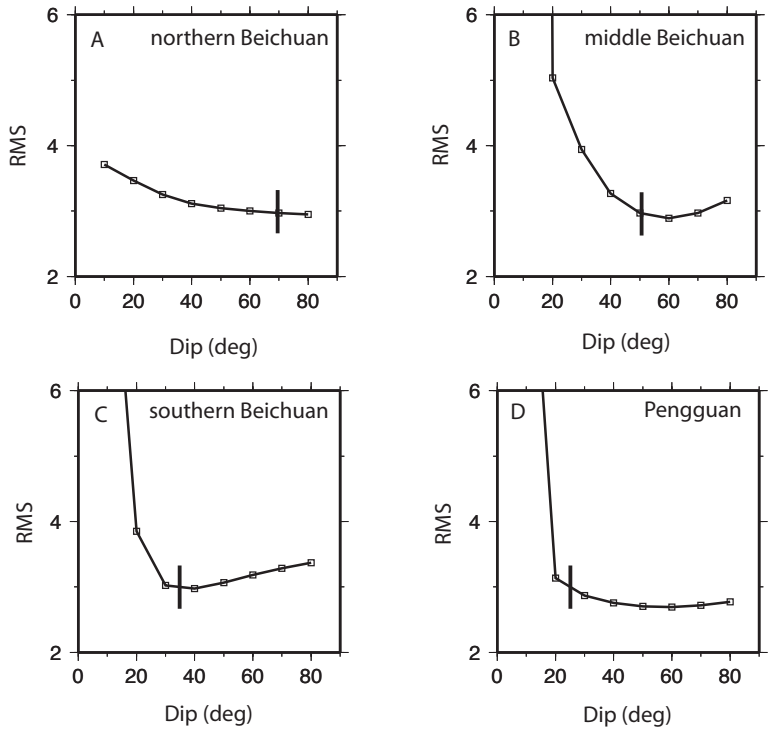

Figure 2.6: Plots of the normalized RMS misfit with various fault dip angles. We altered the dip angle of each fault segment at 10° interval while keeping other parameters fixed in searching for optimal fault dips. The stick indicates the dip angles we used in our best-fitting model. For the middle and southern Beichuan fault, the constraint are fairly well as can be seen in the subplot B and C. Subplot A suggests a nearly vertical fault in the northern Beichuan. Subplot D shows the Pengguan fault is worse constrained: the dip angle can vary from 20° to 80° .

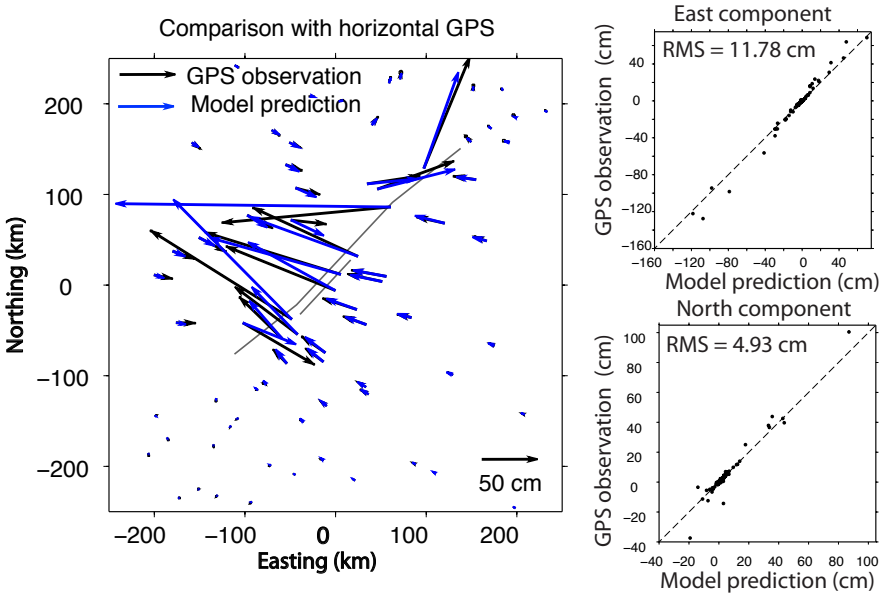

Figure 2.7: The subplot on the left is the horizontal GPS measurements (black arrows) and our model prediction (blue arrows). The two subplots on the right are model prediction versus GPS observation in east and north direction. The model residuals in the corner show the goodness of the fit. The larger RMS in east component could be due to larger magnitude of the east-westward movement. Gray lines are simplified fault models. The error ellipses on the GPS data are relatively too small to be seen in the figure.

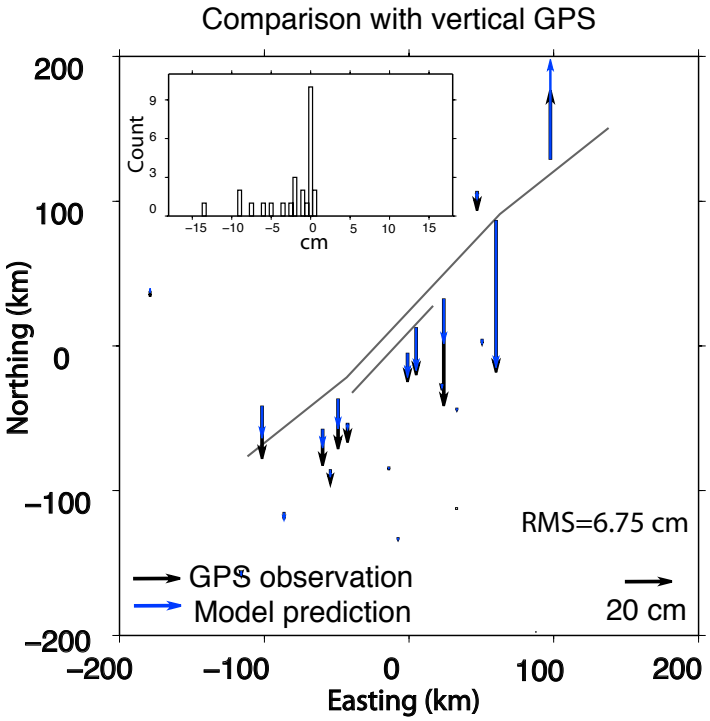

Figure 2.8: The vertical GPS measurements (black arrows) and the model predictions (blue arrows). The subplot in the upper left corner shows the distribution of the residuals.

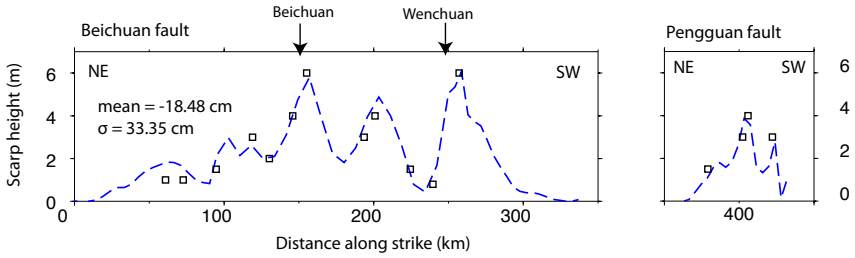

Figure 2.9: The black boxes are selected scarp height measurements used in the inversion from geological survey. The blue dash lines are the model predictions. The vertical offsets vary along the strike of the fault with peaks near Beichuan and Wenchuan areas. The model residuals have a mean value of -18.48cm and a standard deviation of 33.35 cm.

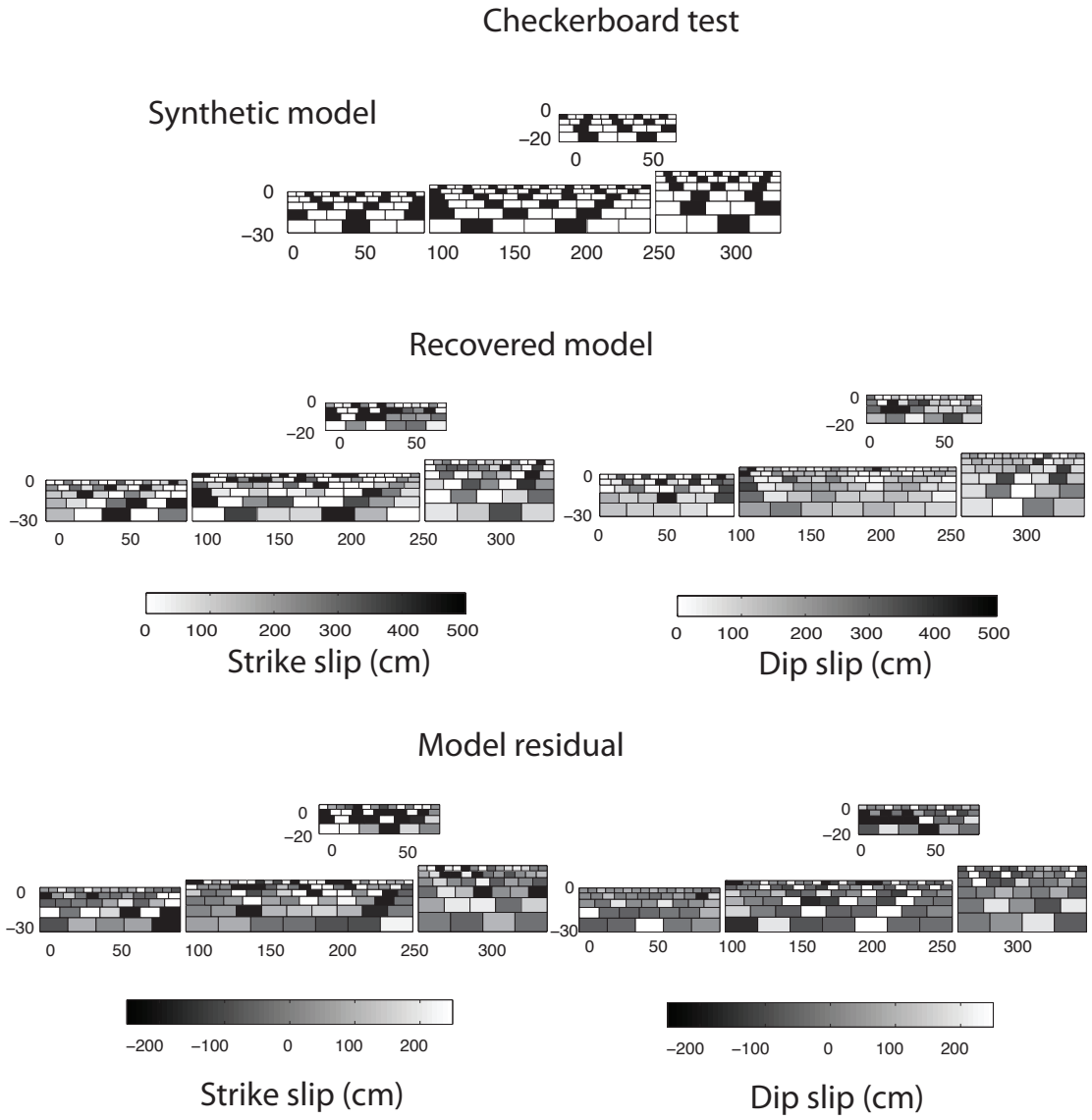

Figure 2.10: Checkerboard test on resolution of the inversion. The generated synthetic model has displacement of either zero or 500 cm at intervals for both the right-lateral strike-slip and dip-slip components. Then we simulated the LOS radar data, GPS data and scarp measurement and inverted for the best-fitting recovered models

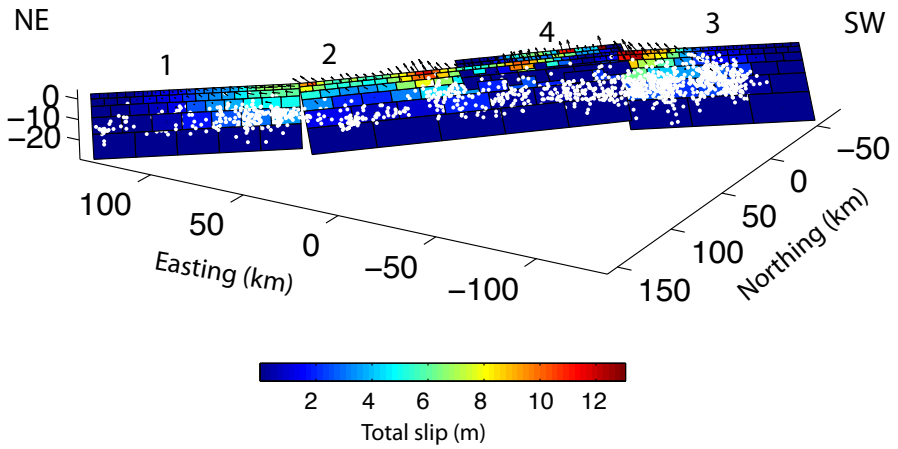

Figure 2.11: Coseismic slip model in 3D view. The white dots are the aftershocks from double difference relocation result.

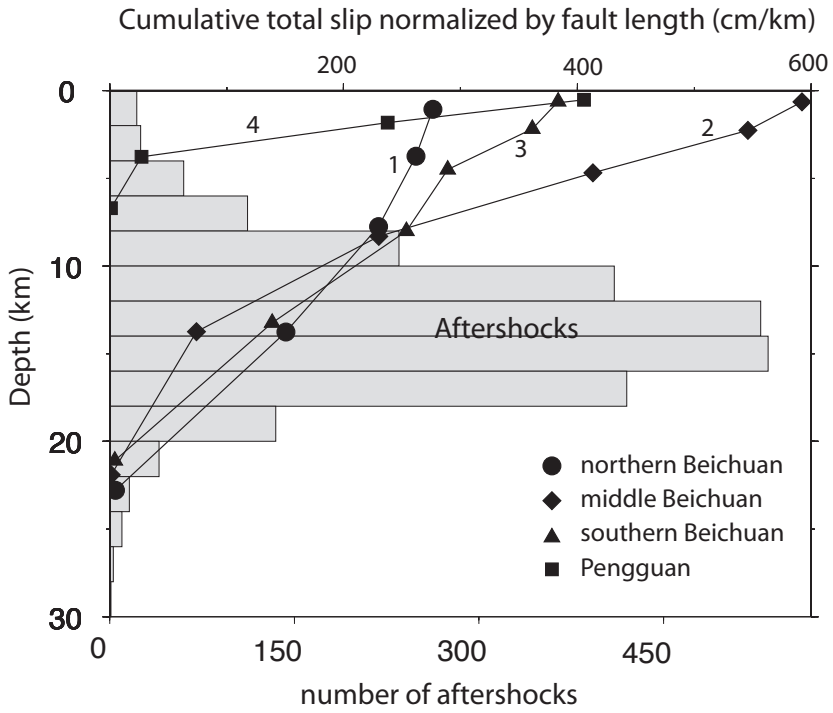

Figure 2.12: The amount of slip versus depth. The connected symbols indicate the normalized cumulative slip on the four fault segments, whose scale is on the top horizontal axis. The index numbers (1 to 4) on each line correspond to different fault segments. The gray histogram shows the depth distribution of aftershocks.

Chapter 3

The 2010 Maule, Chile earthquake: Downdip rupture limit revealed from space geodesy

Radar interferometry from the ALOS satellite captured the coseismic ground deformation associated with the 2010 Mw 8.8 Maule, Chile earthquake. The ALOS interferograms along ascending tracks reveal a sharp transition from high fringe rate to low fringe rate at $\sim$ 150 km from the trench axis. At a similar distance the descending interferograms exhibit a phase minimum. These fringe patterns are diagnostic of the downdip rupture limit of the Maule earthquake. An elastic dislocation model based on both ascending and descending ALOS interferograms and 13 near-field 3-component GPS measurements reveals that the coseismic slip decreases more or less linearly from a maximum of 17 m (along-strike average of 6.5 m) at 18 km depth to near zero at 43-48 km depth, quantitatively indicating the downdip limit of the seismogenic zone. The depth at which slip drops to near zero appears to be at the intersection of the subducting plate with the continental Moho. Our model also suggests that the depth where coseismic slip vanishes is nearly uniform along the strike direction for a rupture length of $\sim$ 600 km. The

[0]This chapter is a reformatted version of a publication in *Geophysical Research Letters*: Tong, X., *et al.*, "The 2010 Maule, Chile earthquake: Downdip rupture limit revealed by space geodesy", v.37, L24311, doi:10.1029/2010GL045805, 2010

average coseismic slip vector and the interseismic velocity vector are not parallel, which can be interpreted as a deficit in strike-slip moment release.

3.1 Introduction

On February 27, 2010, a magnitude 8.8 earthquake struck off the coast of Maule, Chile. The earthquake occurred on a locked megathrust fault resulting from oblique convergence of the oceanic Nazca plate subducting beneath the continental South American plate at $\sim$ 6.5 cm/yr (*Kendrick et al.*, 2003). To date, the Maule event is the fifth largest earthquake since modern recording began, and the largest in this region since the great magnitude 9.5 Chile earthquake in 1960. Modern geodetic technologies permit this event to be studied in greater detail than was possible for any previous large earthquake. Studying the downdip limit of seismogenic rupture in relation to the compositional layering of surrounding areas may provide insights into the rheological controls on the earthquake process. Of particular interest in the case of continental subduction zones is the relationship between the downdip limit of stick-slip behavior and the depth of the continental Moho at its intersection with the subduction interface (*Oleskevich et al.*, 1999; *Hyndman*, 2007).

There are at least four approaches to probing the downdip limit of seismic rupture for subduction thrust earthquakes. The first approach uses the maximum depth of the moderate thrust events along plate interfaces from global teleseismic data. *Tichelaar and Ruff* (1993) estimated the maximum depth of the seismically coupled zone of the Chile subduction zone to be 36-41 km south of 28° S and 48-53 km north of 28° S. Using a similar approach, *Pacheco et al.* (1993) suggested that this downdip limit is at 45 km depth in Central Chile. A second approach is to use the interseismic velocity from near-field GPS measurements to infer the downdip limit of the locked zone (*Brooks et al.*, 2003; *Bürgmann et al.*, 2005). However, with the exceptions of Japan and Cascadia, there are generally not enough GPS stations in convergent plate boundaries to accurately constrain the locking depth. The third approach uses precisely located episodic-tremor-and-slip (ETS) (e.g. in

Cascadia, southwest Japan, and Mexico) as a proxy for the downdip edge of the seismogenic zone (*Rogers and Dragert*, 2003; *Schwartz*, 2007). A fourth approach uses geodetic measurements (e.g., GPS and InSAR) to invert for the co-seismic slip distribution on the megathrust and infer the downdip limit of the rupture (*Pritchard et al.*, 2007; *Hyndman*, 2007). Geodesy data, combined with optical images of shoreline emergence, were used to invert for the slip distribution of the Great Sumatra-Andaman 2004 earthquake, although the geodetic coverage was insufficient to provide better than 80 km spatial resolution on slip patches (*Subarya et al.*, 2006). Here we use nearly complete geodetic coverage from ALOS L-band interferometry (launched January 2006) to resolve the spatial variations in slip for the entire Maule, Chile megathrust zone to a resolution of 40 km or better, and thus provide tight constraints on the depth of this rupture.

3.2 InSAR and GPS data analysis

We investigated the crustal deformation produced by the Mw 8.8 Maule, Chile earthquake using interferometric synthetic aperture radar (InSAR) (*Massonnet and Feigl*, 1998) from the Advanced Land Observatory Satellite (ALOS) (*Shimada et al.*, 2010) in conjunction with measurements obtained from thirteen continuously operating GPS (CGPS) stations. Following the Maule, Chile earthquake, the Japan Aerospace Exploration Agency (JAXA) conducted high priority observations using Fine Beam Single Polarization (FBS) strip-mode SAR along ascending orbits and burst-synchronized ScanSAR along descending orbits. The improved coherence at L-band along with systematic pre- and post-earthquake acquisitions yielded excellent coseismic InSAR coverage of a 630 km by 150 km area of ground deformation (Figure 3.1 and Table 3.1). The interferograms were analyzed frame-by-frame using the same local earth radius and spacecraft ephemeris to ensure along-track phase continuity. We used the line-of-sight (LOS) displacement from both ascending and descending orbits to distinguish between horizontal and vertical deformation. We processed track T422-subswath4 (T422-sw4) using newly developed FBS to ScanSAR software following the algorithm of *Ortiz and Ze-*

bker (2007) and track T422-subswath3 (T422-sw3) using our ScanSAR-ScanSAR processor, which is part of the GMTSAR software (*Sandwell et al.*, 2008; *Tong et al.*, 2010). The ScanSAR to strip mode interferograms along track T422-sw4 are critical for recovering the complicated deformation near the shoreline from the descending orbits.

An examination of the raw phase data reveals an interesting feature in the coseismic surface deformation: the dashed black line on the ascending interferograms (Figure 3.1a) marks a boundary where the phase gradient changes remarkably, reflecting that the coseismic slip stopped at $\sim$ 150 km from the trench axis (i.e. $\sim$ 40 km depth for a fault with 15° dip angle). At a similar distance from the trench, the descending interferograms exhibit a phase minimum (Figure 3.1b). Both of these features are diagnostic of the surface deformation immediately above the downdip extent of the megathrust (*Savage*, 1983). The different signatures seen in the ascending and descending interferograms are due to the difference in the radar LOS vectors.

As interferograms are only able to detect relative movement, GPS vectors are important for providing absolute measurements of displacement and constraining the overall magnitude of slip (*Fialko et al.*, 2001). Near-field 3-component GPS displacement vectors in this region provide independent constraints on the fault slip model. We did not include GPS measurements that are beyond $\sim$ 300 km from the coast of the Maule, Chile region. Adding the far-field GPS sites should not change the features of our slip model in the depth of 15-45 km because the geometric attenuation would cause all the far-field GPS measurements to be largely sensitive to the long wavelength part of the model. Methods used for unwrapping the interferograms and adjusting the absolute value of range change to the GPS measurements are discussed in the following sections. We found that it was not necessary to remove a ramp from the interferograms in order to achieve the 10 cm uncertainty assigned to the digitized InSAR measurements.

The LOS displacement ranges from 1 cm to 428 cm along ascending orbits (820 data points) and -368 cm to 21 cm along descending orbits (1112 data points). The maximum LOS displacement along the ascending tracks is near the Peninsula

in Arauco, Chile while the maximum negative LOS displacement along the descending track is north of Constitucin (Figure 3.2). Profiles of LOS displacement (Figures 2.3) show that the characteristic inflection points at $\sim$ 150 km east of the trench are readily discernable from transects of the InSAR LOS displacement.

3.2.1 GPS data analysis

All available continuous GPS data in South America from 2007 through 2010 May 5 were processed using GAMIT (*King and Bock*, 1999) with additional GPS sites included to provide reference frame stability (Tabel 2.1). All data were processed using the MIT precise orbits. Orbits were held tightly constrained and standard earth orientation parameters (EOP) and earth and ocean tides were applied. Due to the number of stations, two separate subnets were formed with common fiducial sites. The subnets were merged and combined with MIT's global solution using GLOBK. We defined a South American fixed reference frame, primarily from the Brazilian craton, to better than 2.4 mm/yr RMS horizontal velocity by performing daily Helmert transformations for the network solutions and stacking in an ITRF2005 reference frame (*Kendrick et al.*, 2006). Finally we used these time series to estimate the coseismic displacement, or jumps, at each station affected by the Maule event, as well as crustal velocity before and after the earthquake.

3.2.2 InSAR phase unwrapping and adjustment

We unwrapped all the interferograms by digitizing and counting fringes at every 2 phase cycle (11.8 cm) (see Figure 3.2). This method works well even in low coherence areas, such as ScanSAR-ScanSAR interferograms (see Figure 3.1, T422-sw3). We assembled all the digitized fringes, subsampled them using a blockmedian average with pixel spacing of 0.05° in latitude and 0.1° in longitude, and converted them into line of sight (LOS) displacement. The interferograms are subject to propagation delay through the atmosphere and ionosphere. It is likely that T112 and parts of T116 include significant ($>$ 10 cm) ionospheric delay, so

these data were excluded from the analysis. To account for the potential errors in digitization and propagation delay effects, we assigned a uniform uncertainty of 10 cm to the LOS data. Interferometry is a relative measurement of LOS displacement, so after unwrapping the average value of each track was adjusted to match the available GPS displacement vectors projected into the LOS direction. For tracks that do not contain a GPS station, their average value was adjusted so that the LOS displacement field is mostly continuous from track to track. Over a distance of up to 1000 km the satellite orbits are much more accurate than the 10 cm assigned uncertainty (*Sandwell et al.*, 2008) so no linear ramp was removed from the unwrapped and sampled LOS displacement data. Even after adjustment, the phase between neighboring tracks is sometimes discontinuous, as seen, for example, at the southern end of the descending interferograms (see Figure 3.1b) where the fringes are denser in T422-sw4 than T420. This is partially due to the difference in look angle between the far range in one track and the near range of the adjacent track. This kind of discontinuity can also be caused by rapid and significant postseismic deformation between the acquisition times of the adjacent SAR tracks. The final step in the processing was to calculate the unit look vector between each LOS data point and the satellite using the precise orbits. This is needed to project the vector deformation from a model into the LOS direction of the measurement.

3.2.3 Uncertainty in GPS and InSAR data

When calculating the weighted residual misfit, we estimated the uncertainty of the geodetic measurement. Errors in the GPS measurement were calculated using residual scatter values (Table 3.2). Errors in the InSAR LOS displacement measurement were assigned uniformly as 10 cm based on posteriori misfit.

3.3 Coseismic slip model and resolution test

We used InSAR and GPS observations to constrain a model of coseismic slip on a single plane striking N 16.8° E and dipping 15° to the east, approximating the

geometry of the megathrust (Figure 3.3). We also tested a model that more closely follows the trench axis, but the more complicated model did not improve the RMS misfit. The surface trace and dip angle of the fault plane were initially determined by fitting the locations of $M > 6.0$ aftershocks and then refined using the geodetic data. The weighted residual misfit is determined from $\chi^2 = \frac{1}{N}\sum_{i=1}^{N}(\frac{o_i - m_i}{\sigma_i})^2$, where o_i is the geodetic displacement measurement, m_i is the modeled displacement, σ_i is the uncertainty estimate of the i^{th} measurement, and N is the total number of InSAR LOS displacement and 3-component GPS measurements. A 15° dip is preferred because a steeper dip angle (18°) results in a larger misfit (Figure 3.4) and a shallower dip angle (12°) results in unlikely maximum slip at the top edge of the fault plane (i.e. 0 km depth). Moreover, the 12° dipping fault plane lies shallower than both the hypocenter and the $M > 4$ background seismicity from 1960-2007, whose depths are well constrained in the EHB bulletin (Figure 3.3).

This finite fault model assumes an isotropic homogeneous elastic half-space (*Okada*, 1985; *Fialko*, 2004). The fault plane is 670 km long and 260 km wide and is subdivided into 19.7 km by 20 km patches. The fault patch size was chosen to retrieve major features in the slip model while keeping the inversion problem manageable. A resolution analysis is provided in the following section and shows that features 40 km by 40 km are well resolved over the area of InSAR coverage. This 40 km resolution along the dipping fault plane provides approximately 10 km absolute depth resolution (see Figure 3.3). We applied a non-negativity constraint to allow only thrust and right-lateral strike slip. In this geodetic inversion, only the bottom boundary of the fault plane is constrained to have zero slip. The smoothness matrix penalizes the curvature (second derivative) of slip on the fault plane. The relative weight of the GPS and InSAR data is determined iteratively such that the residuals are minimized in both datasets. We determined the roughness of the model based on the trade-off curve between model smoothness and the normalized RMS misfit. The RMS misfit for ascending and descending LOS displacement is 10.9 cm and 7.9 cm respectively and the RMS misfit for the GPS data is: 1.54 cm for the east component, 0.44 cm for the north component and 2.93 cm for the up component. The residuals in InSAR LOS displacement (Figure 3.2c and 2.2d) are

generally smaller than 15 cm, though there are larger misfits in the southern end of the rupture area. The ALOS interferograms, LOS data points and slip model are available at `ftp://topex.ucsd.edu/pub/chile_eq/chile_insar.zip`.

3.3.1 Model optimization

As described in the previous section, the model consists of a 670 km long and 260 km wide 15° dipping fault plane in a homogeneous elastic half-space. The minimization criteria is given by the equation

$$min(\| Am - b \|^2 + \lambda^2 \| Sm \|^2) \tag{3.1}$$

where the first term minimizes the data misfit and the second term minimizes model roughness (i.e., second derivative) of slip on the fault plane. In the first term, A is the inversion matrix, m is the vector of unknowns, and b is the matrix of observations, given by

$$A = \begin{bmatrix} \sigma_{LOS}^{-1} G_{LOS} \\ \beta \sigma_{GPS}^{-1} G_{GPS} \end{bmatrix}, m = \begin{bmatrix} m_{dip} \\ m_{strike} \end{bmatrix}, b = \begin{bmatrix} \sigma_{LOS}^{-1} d_{LOS} \\ \beta \sigma_{GPS}^{-1} d_{GPS} \end{bmatrix} \tag{3.2}$$

The A matrix consists of the Greens function matrices G_{LOS} and G_{GPS} weighted by the uncertainties in the measurements. The two diagonal matrices σ_{LOS} and σ_{GPS} are derived from measurement uncertainties, and β represents the relative weight between InSAR and GPS data sets. The model vectors m_{dip} and m_{strike} represent dip slip components and strike slip components on discretized fault patches. In matrix b, the observation vectors d_{LOS} and d_{GPS} consist of the InSAR data, which are the LOS displacement from the ascending and descending tracks, and the GPS data with east-north-up displacement components. In the second term the smoothness matrix is given by

$$S = \begin{pmatrix} -1 & 4 & 1 & 0 & \cdots \\ 0 & -1 & 4 & 1 & \cdots \\ \vdots & \vdots & \vdots & \ddots & \cdots \\ 0 & \cdots & -1 & 4 & -1 \end{pmatrix} \tag{3.3}$$

The relative weighting between GPS and InSAR data, parameter β, is determined iteratively so that the residuals are minimized in both datasets. We select the relative weighting between the data misfit and roughness, parameter λ , based on the trade-off curve between model smoothness and the normalized RMS misfit. Nine different weights were tested and the preferred model is chosen at the turning point of this trade-off curve (Figure 3.5). While the selection of the best model is somewhat subjective, all the models share a common characteristic of high depth-averaged slip at an along-dip distance of 60-100 km and essentially zero slip at $\sim$ 160 km.

3.3.2 Resolution tests

To assess the resolution capabilities of the data and model, we conducted two sets of checkerboard tests. The first test had a 20 km checkerboard of 5 m in dip slip (Figure 3.6, 2.7 and 2.8). The checkerboard model was used to generate synthetic InSAR and GPS data at the observation locations. The InSAR, and GPS data were assigned the same uncertainties as used in the final model. We inverted for a best fitting solution by adjusting the smoothness parameter while retaining all the other parameter settings as were used in the final model. We found that the resolution is better over the southern half of the fault plane where there is more complete InSAR coverage closer to the trench axis. We calculated the RMS of the slip difference (i.e. a measure of the misfit) between the synthetic model and the recovered model, averaged over the fault strike direction. Plots of RMS slip difference versus depth (Figure 3.8) show a minimum at a downdip distance of 120 km. The accuracy of the recovered model is good between downdip distances of 110 and 130 km where the average RMS curve falls below 100 cm. Over this depth range features as small as 20 km can be resolved to a 20% accuracy. We repeated the checkerboard test at a size of 40 km as shown in Figure 3.7. The accuracy of the recovered checkerboard improves significantly when the checker size is increased from 20 km to 40 km. We calculated the RMS of the slip difference in a same way as we did for 20 km checker size (see Figure 3.8). The accuracy of the recovered model is good between downdip distances of 70 and 220 km where

the average RMS curve falls below 100 cm, corresponding to the area where the recovered model uncertainties are less than 20% of the input model. The accuracy is excellent between the downdip distances of 80 and 190 km where the average RMS curve falls below 50 cm, corresponding to the area where the recovered model uncertainties are less than 10% of the input model. From these checkerboard tests we conclude that the overall model resolution is 40 km or better over the downdip depth range of 70 to 220 km.

3.3.3 Determination of shear modulus

Our model requires a representative value of shear modulus in order to calculate the geodetic moments from the slip model, although the Okadas displacement solution only depends on the Poissons ratio. We determined the average shear modulus from regional 1D seismic velocity structure (*Bohm et al.*, 2002). Above 45 km depth, the average shear modulus (weighted by layer thickness) is 38.3 GPa. Above 55 km depth, the average shear modulus (weighted by layer thickness) is 43.5 GPa. Thus an average shear modulus of 40 GPa is a preferred value for estimating geodetic moment.

3.3.4 Results

The preferred slip model (Figure 3.4) shows significant along-strike variation of the fault rupture. The most intense fault slip is found to be about 17 m, located at 140-180 km north of the epicenter. This is consistent with the large LOS displacement over that region seen in the interferograms (Figure 3.1). To the south of the epicenter near the peninsula in Arauco, Chile is another patch of significant slip. The length of the rupture area of slip greater than one meter is 606 km, compared with 645 km indicated by the aftershock distribution. Figure 3.4b shows the depth distribution of fault slip from the geodetic inversion. The peak of the coseismic slip is located offshore and is at $\sim$ 18 km depth. The depth of maximum slip is slightly shallower than the depth of rupture initiation, given by the USGS/NEIC PDE catalog as 22 km.

The coseismic slip model from a joint inversion of GPS and InSAR data (Figure 3.4a) suggests the slip direction is dominantly downdip, with a relatively small component of right-lateral strike-slip. Assuming the average shear modulus to be 40 GPa, the total moment of the preferred model is $1.82 \times 10^{22} Nm$ (thrust component: $1.68 \times 10^{22} Nm$; right-lateral strike-slip component: $4.89 \times 10^{21} Nm$). The total corresponds to moment magnitude 8.77, comparable to the seismic moment magnitude 8.8. Because of the lack of observations offshore, the geodetic model probably underestimates the amount of slip at shallower depth, which could explain the observed moment discrepancy. The above relatively smooth and simple model results in a variance reduction in the geodetic data of 99%.

We compared the direction of the interseismic velocity vector with the direction of the area-averaged coseismic slip vector. A non-parallel interseismic velocity vector and coseismic slip vector would indicate an incomplete moment release of the Maule event. The interseismic velocity from the Nazca-South America Euler vector is oriented at 27.3° counterclockwise from trench perpendicular (*Kendrick et al.*, 2003). Based on the ratio of the thrust and right-lateral strike-slip moments, the area-averaged coseismic slip direction is 16.8 ° counterclockwise from trench perpendicular. The misalignment of the interseismic velocity vector and the coseismic slip vector could be interpreted as a moment deficit in right-lateral strike-slip moment. This moment deficit is about $3.49 \times 10^{21} Nm$, equivalent to 70% of the moment release in strike-slip component, which could be accommodated by either aseismic slip or subsequent earthquakes.

The most intriguing observation from the slip model is that the along-strike-averaged slip decreases by more than a factor of 10 between 18 km and 43 km depth and reaches a minimum of approximately zero at a depth of 43-48 km (Figure 3.4b). This dramatic decrease indicates the downdip limit of the seismogenic zone and the transition from seismic to aseismic slip. The depth at which slip drops to near zero is almost uniform in the along-strike direction for a rupture length of $\sim$ 600 km. This depth approximately corresponds to the intersection of the subducting plate with the continental Moho. Based on receiver function and seismic refraction analysis, the Moho depth is between 35 and 45

km (*Yuan et al.*, 2002; *Sick et al.*, 2006), although it is not well resolved at its intersection with the subducting plate. We used a checkerboard resolution test to explore the model resolution and to understand the uncertainties in the along-strike averaged slip versus depth estimation. We found that the resolution is better on the southern half of the fault plane where we have more complete InSAR and GPS coverage near the rupture. The accuracy of the recovered checkerboard improves significantly when the size of the checkerboard pattern increased from 20 km to 40 km. For a feature with size of 20 km in the slip model, the resolution is good over the downdip distance of 90-140 km. For a feature with size of 40 km, the resolution is good over the downdip distance of 50-240 km and is even better over the downdip distance of 70-180 km (Figure 3.8). This checkerboard test confirms that the monotonic decrease in slip between 18-43 km depth and the slip minimum between 43-48 km depth is well resolved ($\sim$ 10 km resolution in depth). Slip uncertainties are larger at the top and bottom ends of the fault plane (depth $<$ 15 km and depth $>$ 50 km). The slip model also shows a slight increase in slip at depth greater than 50 km, but this feature is not supported by the resolution analysis.

3.4 Discussion and conclusions

We compared the coseismic slip model derived from near-field displacement measurements from this study with previous published slip models. Our geodetic inversion, a teleseismic inversion of P, SH, and Rayleigh wave (*Lay et al.*, 2010) and a joint inversion of InSAR, GPS, and teleseismic data (*Delouis et al.*, 2010) all suggest that the largest slip occurred to the north of the epicenter. However, none of the previous studies have used the InSAR observations from both the ascending and descending orbits to resolve the downdip rupture limit. Our study is novel in that we infer the downdip rupture limit from a prominent change in LOS displacement manifested in interferograms (Figure 1).

The along-strike averaged slip depth distribution suggests that the coseismic slip of the Maule event peaks at 18 km depth and decreases to near zero at 43-48

km depth. From a phenomenological perspective the slip distribution indicates that the contact between oceanic and continental crust is velocity weakening. The largest fraction of interseismic coupling occurs at a depth of $\sim$ 18 km and this fraction decreases more or less linearly with increasing depth to $\sim$ 43 km where it becomes essentially zero. This observation is in fair agreement with the observation that earthquake depth distribution tapers smoothly to zero (*Tichelaar and Ruff*, 1993; *Pacheco et al.*, 1993), indicating the accumulated and released energy on the megathrust is not a simple step function that goes to zero at 43 km.

Based on available seismic evidence on the local Moho depth, we note that the downdip coseismic rupture limit is near the depth where the subducting Nazca plate intersects with the continental Moho of the South America plate. This downdip limit approximately coincides with the transition in topography from Coast Range to Longitudinal Valley. It is noticeable that the free-air gravity changes from positive to negative at the same location as this downdip limit (see Figure 3.3c). Further, the surface heat flow is low at the Coast Range above the intersection of the descending oceanic plate with the fore-arc mantle (*Springer and Förster*, 1998).

There are two possible physical mechanisms controlling the downdip limit of the seismogenic zone. First, fault friction behavior may transition from velocity weakening to velocity strengthening at the depth of the 350-450° C isotherm (*Oleskevich et al.*, 1999; *Hyndman*, 2007; *Klingelhoefer et al.*, 2010). Second, the downdip rupture limit may occur at the depth of the fore-arc Moho due to a change in frictional properties associated with the serpentinization of the mantle wedge (*Bostock et al.*, 2002; *Hyndman*, 2007; *Hippchen and Hyndman*, 2008). In southern Chile, the 350° C isotherm is at a similar depth as the fore-arc Moho, hence previous studies could not distinguish between the two possible controlling mechanisms. The observed monotonic decrease in slip with depth combined with the tapering of the earthquake depth distribution provides new information that can be used to constrain earthquake cycle models at megathrusts. This transitional behavior is similar to what is observed on continental transforms both in terms of coseismic slip (*Fialko et al.*, 2005) and seismicity (*Marone and Scholz*, 1988; *Tichelaar and*

Ruff, 1993; *Pacheco et al.*, 1993).

In summary we have found: (1) The ALOS interferograms show pronounced changes in fringe pattern at a distance of $\sim$ 150 km from the trench axis that are diagnostic of the downdip rupture limit of the Maule earthquake. (2) An elastic dislocation model based on InSAR and GPS displacement measurements shows that the coseismic slip decreases more or less linearly from its maximum at $\sim$ 18 km depth to near zero at 43 km depth. (3) The depth at which slip drops to near zero is almost uniform in the along-strike direction for a rupture length of $\sim$ 600 km and it appears to be at the intersection of the subducting plate with the continental Moho. (4) The average coseismic slip vector and the interseismic velocity vector are not parallel, suggesting a possible deficit in strike-slip moment release.

References

Bohm, M., S. Lüth, H. Echtler, G. Asch, K. Bataille, C. Bruhn, A. Rietbrock, and P. Wigger (2002), The southern Andes between 36 and 40 s latitude: seismicity and average seismic velocities, *Tectonophysics*, *356*(4), 275–289.

Bostock, M., R. Hyndman, S. Rondenay, and S. Peacock (2002), An inverted continental moho and serpentinization of the forearc mantle, *Nature*, *417*(6888), 536–538.

Brooks, B. A., M. Bevis, R. Smalley Jr, E. Kendrick, R. Manceda, E. Lauria, R. Maturana, and M. Araujo (2003), Crustal motion in the southern Andes (26–36 s): Do the Andes behave like a microplate?, *Geochemistry Geophysics Geosystems*, *4*(10), 1085.

Bürgmann, R., M. G. Kogan, G. M. Steblov, G. Hilley, V. E. Levin, and E. Apel (2005), Interseismic coupling and asperity distribution along the Kamchatka subduction zone, *Journal of geophysical research*, *110*(B7), B07,405.

Delouis, B., J.-M. Nocquet, and M. Vallée (2010), Slip distribution of the February 27, 2010 Mw= 8.8 Maule earthquake, central Chile, from static and high-rate GPS, InSAR, and broadband teleseismic data, *Geophysical Research Letters*, *37*(17), L17,305.

Fialko, Y. (2004), Evidence of fluid-filled upper crust from observations of post-seismic deformation due to the 1992 Mw7. 3 Landers earthquake, *Journal of geophysical research*, *109*(B8), B08,401.

Fialko, Y., M. Simons, D. Agnew, et al. (2001), The complete (3-D) surface displacement field in the epicentral area of the 1999 Mw 7.1 Hector Mine earthquake, California, from space geodetic observations, *Geophys. Res. Lett*, *28*(16), 3063–3066.

Fialko, Y., D. Sandwell, M. Simons, and P. Rosen (2005), Three-dimensional deformation caused by the Bam, Iran, earthquake and the origin of shallow slip deficit, *Nature*, *435*(7040), 295–299.

Hippchen, S., and R. Hyndman (2008), Thermal and structural models of the Sumatra subduction zone: Implications for the megathrust seismogenic zone, *Journal of Geophysical Research*, *113*(B12), B12,103.

Hyndman, R. (2007), The seismogenic zone of subduction thrust faults, *The seismogenic zone of subduction thrust faults*, pp. 15–40.

Kendrick, E., M. Bevis, R. Smalley Jr, B. Brooks, R. B. Vargas, E. Lauria, and L. P. S. Fortes (2003), The Nazca–South America Euler vector and its rate of change, *Journal of South American Earth Sciences*, *16*(2), 125–131.

Kendrick, E., B. Brooks, M. Bevis, R. Smalley, E. Lauria, M. Araujo, and H. Parra (2006), Active orogeny of the south-central Andes studied with GPS geodesy, *Revista de la Asociación Geológica Argentina*, *61*(4), 555–566.

King, R., and Y. Bock (1999), Documentation for the GAMIT GPS analysis software, *Mass. Inst. of Technol., Cambridge Mass.*

Klingelhoefer, F., et al. (2010), Limits of the seismogenic zone in the epicentral region of the 26 December 2004 great Sumatra-Andaman earthquake: Results from seismic refraction and wide-angle reflection surveys and thermal modeling, *Journal of Geophysical Research*, *115*(B1), B01,304.

Lay, T., C. Ammon, H. Kanamori, K. Koper, O. Sufri, and A. Hutko (2010), Teleseismic inversion for rupture process of the 27 February 2010 Chile (Mw 8.8) earthquake, *Geophysical Research Letters*, *37*(13), L13,301.

Marone, C., and C. Scholz (1988), The depth of seismic faulting and the upper transition from stable to unstable slip regimes, *Geophysical Research Letters*, *15*(6), 621–624.

Massonnet, D., and K. L. Feigl (1998), Radar interferometry and its application to changes in the earth's surface, *Reviews of geophysics*, *36*(4), 441–500.

Okada, Y. (1985), Surface deformation due to shear and tensile faults in a half-space, *Bulletin of the seismological society of America*, *75*(4), 1135–1154.

Oleskevich, D., R. Hyndman, and K. Wang (1999), The updip and downdip limits to great subduction earthquakes: thermal and structural models of Cascadia, south Alaska, sw Japan, and Chile, *Journal of Geophysical Research*, *104*(B7), 14,965–14.

Ortiz, A. B. and H. Zebker (2007), ScanSAR-to-stripmap mode interferometry processing using ENVISAT/ASAR data, *IEEE Transactions on Geoscience and Remote Sensing*, *45*(11).

Pacheco, J. F., L. R. Sykes, and C. H. Scholz (1993), Nature of seismic coupling along simple plate boundaries of the subduction type, *Journal of Geophysical Research*, *98*(14), 133–59.

Pritchard, M., E. Norabuena, C. Ji, R. Boroschek, D. Comte, M. Simons, T. Dixon, and P. Rosen (2007), Geodetic, teleseismic, and strong motion constraints on slip from recent southern Peru subduction zone earthquakes, *Journal of geophysical research*, *112*(B3), B03,307.

Rogers, G., and H. Dragert (2003), Episodic tremor and slip on the Cascadia subduction zone: The chatter of silent slip, *Science*, *300*(5627), 1942–1943.

Sandwell, D. T., D. Myer, R. Mellors, M. Shimada, B. Brooks, and J. Foster (2008), Accuracy and resolution of ALOS interferometry: Vector deformation maps of the Father's day intrusion at Kilauea, *Geoscience and Remote Sensing, IEEE Transactions on*, *46*(11), 3524–3534.

Savage, J. (1983), A dislocation model of strain accumulation and release at a subduction zone, *J. geophys. Res*, *88*(B6), 4984–4996.

Schwartz, S. Y. (2007), *Episodic Aseismic Slip at Plate Boundaries (in The Treatise on Geophysics)*, vol. 4. Earthquake Seismology, pp. 445–472, Elsevier Press, Amsterdam, Netherlands.

Shimada, M., T. Tadono, and A. Rosenqvist (2010), Advanced land observing satellite (ALOS) and monitoring global environmental change, *Proceedings of the IEEE*, *98*(5), 780–799.

Sick, C., et al. (2006), Seismic images of accretive and erosive subduction zones from the Chilean margin, *The Andes*, pp. 147–169.

Springer, M., and A. Förster (1998), Heat-flow density across the central Andean subduction zone, *Tectonophysics*, *291*(1), 123–139.

Subarya, C., M. Chlieh, L. Prawirodirdjo, J.-P. Avouac, Y. Bock, K. Sieh, A. J. Meltzner, D. H. Natawidjaja, and R. McCaffrey (2006), Plate-boundary deformation associated with the great Sumatra–Andaman earthquake, *Nature*, *440*(7080), 46–51.

TICHELAAR, B. W., and L. J. RUFF (1993), Depth of seismic coupling along subduction zones, *JOURNAL OF GEOPHYSICAL RESEARCH*, *98*(B2), 2017–2037.

Tong, X., D. T. Sandwell, and Y. Fialko (2010), Coseismic slip model of the 2008 Wenchuan earthquake derived from joint inversion of interferometric synthetic aperture radar, GPS, and field data, *Journal of Geophysical Research*, *115*(B4), B04,314.

Yuan, X., S. Sobolev, and R. Kind (2002), Moho topography in the central Andes and its geodynamic implications, *Earth and Planetary Science Letters*, *199*(3), 389–402.

Table 3.1: InSAR data used in this study.

track	orbit (reference/repeat)	acquisition dates	baseline (m)	frames	observation mode	comments
Ascending tracks						
T111	07119/21881	5/27/07–3/4/2010	215	6480–6520	FBS-FBS	
T112	21458/22129	2/3/10–3/21/2010	485	6470–6500	FBS-FBS	propagation phase delay
T113	10970/21706	2/15/08–4/7/2010	274	6470-6500	FBS-FBS	more recent pair is noisy
T114	21283/21954	1/22/10–3/9/10	284	6460–6480	FBS-FBS	
T115	21531/22202	2/8/10–5/11/2010	409	6470	FBS-FBS	PRF change
T116	21779/22450	2/25/2010–4/12/10	480	6460	FBS-FBS	propagation phase delay
T117	09949/22027	12/7/07–3/14/10	157	6420-6440	FBS-FBS	low coherence
T118	21604/22275	2/13/2010–3/31/10	717	6410–6430	FBS-FBS	
T119	21181/21852	1/15/10–3/2/10	453	6400–6420	FBS-FBS	
Descending tracks						
T422-sw3	11779/21844	4/10/08–3/1/10	1411	4350	ScanSAR-ScanSAR	low coherence
T422-sw4	21173/21844	1/14/10–3/1/2010	560	4300-4400	FBS-ScanSAR	

T420	21348/22019	1/26/10–3/13/2010	517	4330-4400	FBS-FBS

Table 3.2: GPS measurements used in this study and their fits to the model.

site	longitude	latitude	east	model east	north	model north	vertical	model vertical
ANTC	-71.532	-37.338	-80.62	-81.62	18.37	17.90	-2.73	-5.48
CONZ	-73.025	-36.843	-300.19	-300.15	-67.76	-67.89	-3.98	-4.28
MZ04	-69.020	-32.948	-12.17	-15.20	-4.93	-5.68	1.89	-1.20
SANT	-70.668	-33.150	-23.53	-25.19	-14.07	-14.24	-1.76	-5.88
LNQM	-71.361	-38.455	-33.44	-34.67	14.31	14.32	0.47	-3.85
MZ05	-69.169	-32.951	-12.63	-15.77	-5.19	-6.15	1.79	-1.46
ACPM	-70.537	-33.447	-41.49	-40.24	-18.55	-18.20	-1.90	-5.96
BAVE	-70.765	-34.167	-116.61	-116.57	-19.49	-19.49	-9.44	-9.94
LAJA	-71.376	-37.385	-72.18	-71.77	17.77	17.65	-2.36	-5.00
LLFN	-71.788	-39.333	-11.20	-12.53	7.86	7.69	-1.74	-3.66
LNDS	-70.575	-32.839	-14.27	-15.38	-9.50	-9.34	-1.53	-4.83
MOCH	-73.904	-38.410	-120.39	-120.36	-29.45	-29.45	20.29	20.27
NIEB	-73.401	-39.868	-0.49	-1.76	-2.90	-3.67	-1.26	-4.43

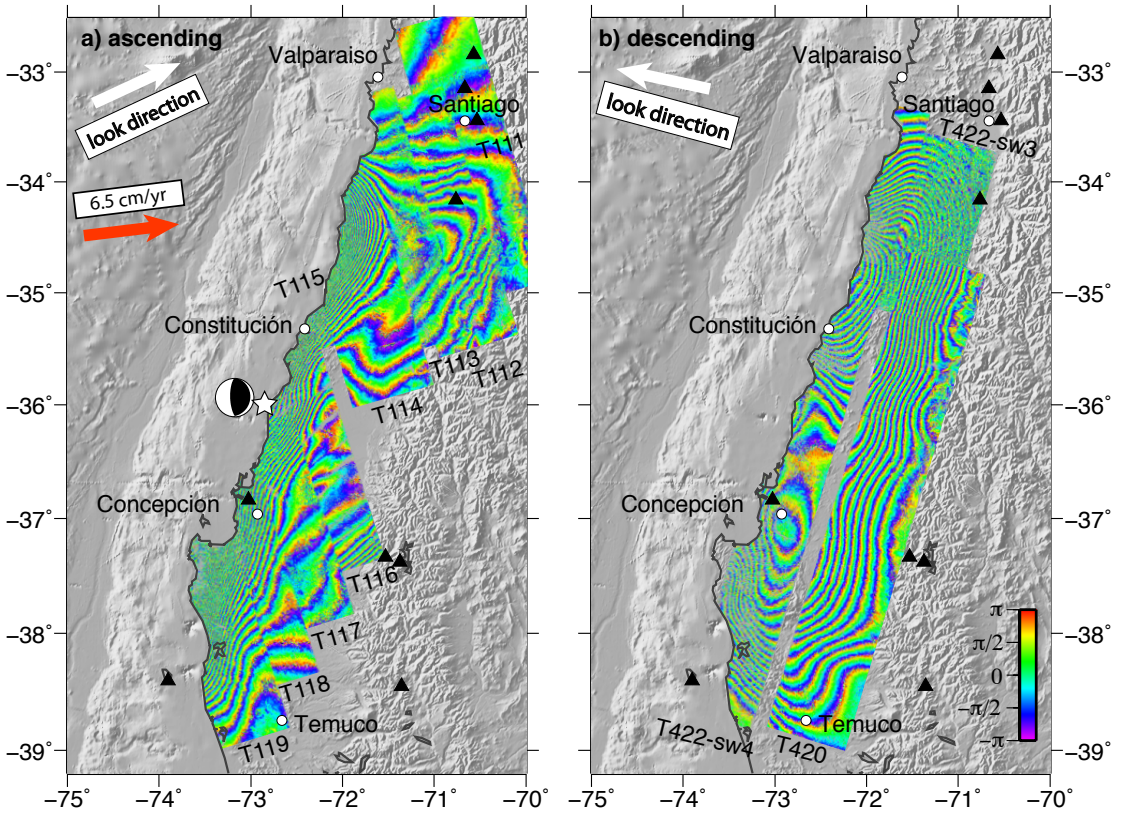

Figure 3.1: Nine tracks of ALOS ascending interferograms (FBS-FBS mode) and two tracks of ALOS descending interferograms (two subswaths of ScanSAR-ScanSAR mode and ScanSAR-FBS mode, and one track of FBS-FBS mode) cover a wide area from the coastline of central Chile to the foothills of the southern Andes. The fat white arrow shows the horizontal component of the line of sight look direction. The nominal look angle from the vertical is 34° . The color scale shows the wrapped phase ($-\pi$ to π) that corresponds to the range change (11.8 cm per cycle) between the ground points and the radar antenna. The ScanSAR acquisition of Track 422 on March 1, 2010 is particularly important for recording the entire coseismic deformation along the coastline of Chile. The white star indicates the earthquake epicenter. The focal mechanism of this earthquake is from Global CMT solution. The black triangles show the locations of the 13 GPS sites used in the inversion (4 sites are outside of the map boundaries). Solid black line shows the surface trace of the simplified fault model and the dashed black line marks the 40-km depth position of the fault for a 15° dip angle. Red fat arrow shows the interseismic convergence vector.

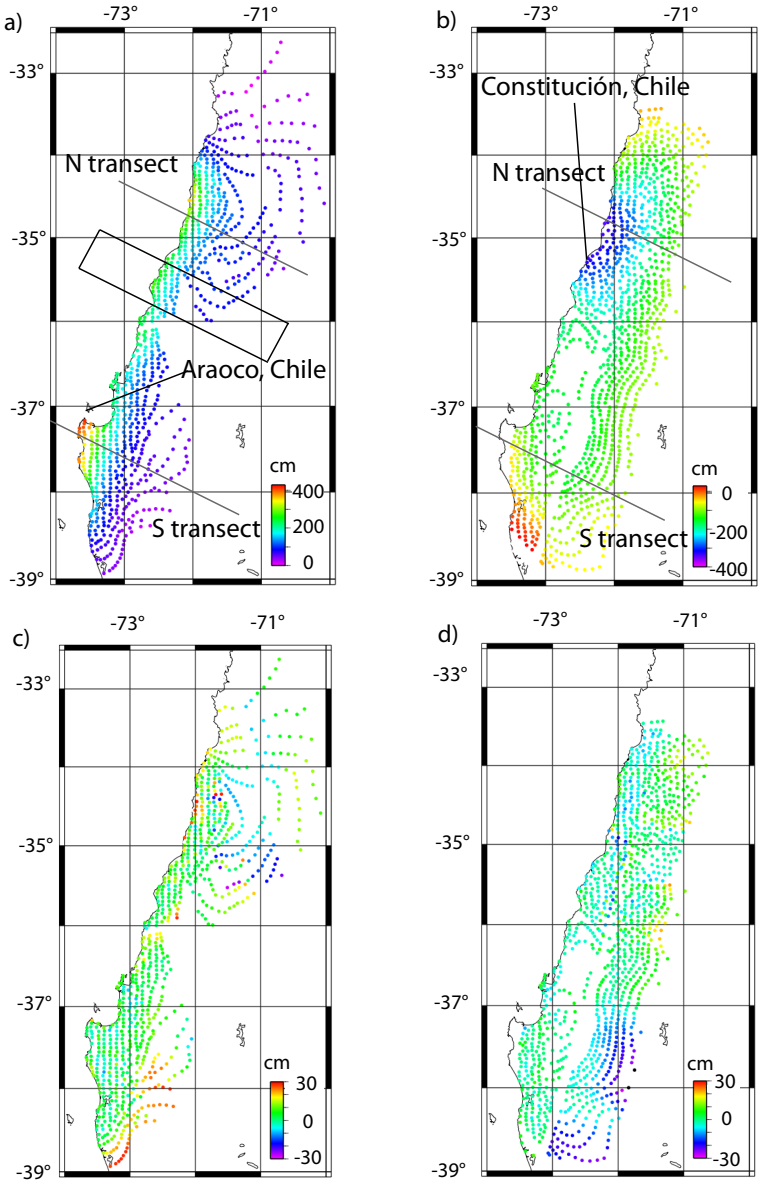

Figure 3.2: Unwrapped, subsampled, and calibrated InSAR line-of-sight (LOS) displacements and their residuals. Positive LOS displacement indicates ground motion toward the radar. a) Ascending LOS displacement. b) Descending LOS displacement. c) Model residuals of the ascending LOS displacement. d) Model residual of the descending LOS displacement. The two black lines (N transect and S transect) mark the locations of profiles shown in Figure 3.3. The black box in subplot a) shows the sampled area of topography and gravity profiles as shown in Figure 3.3c

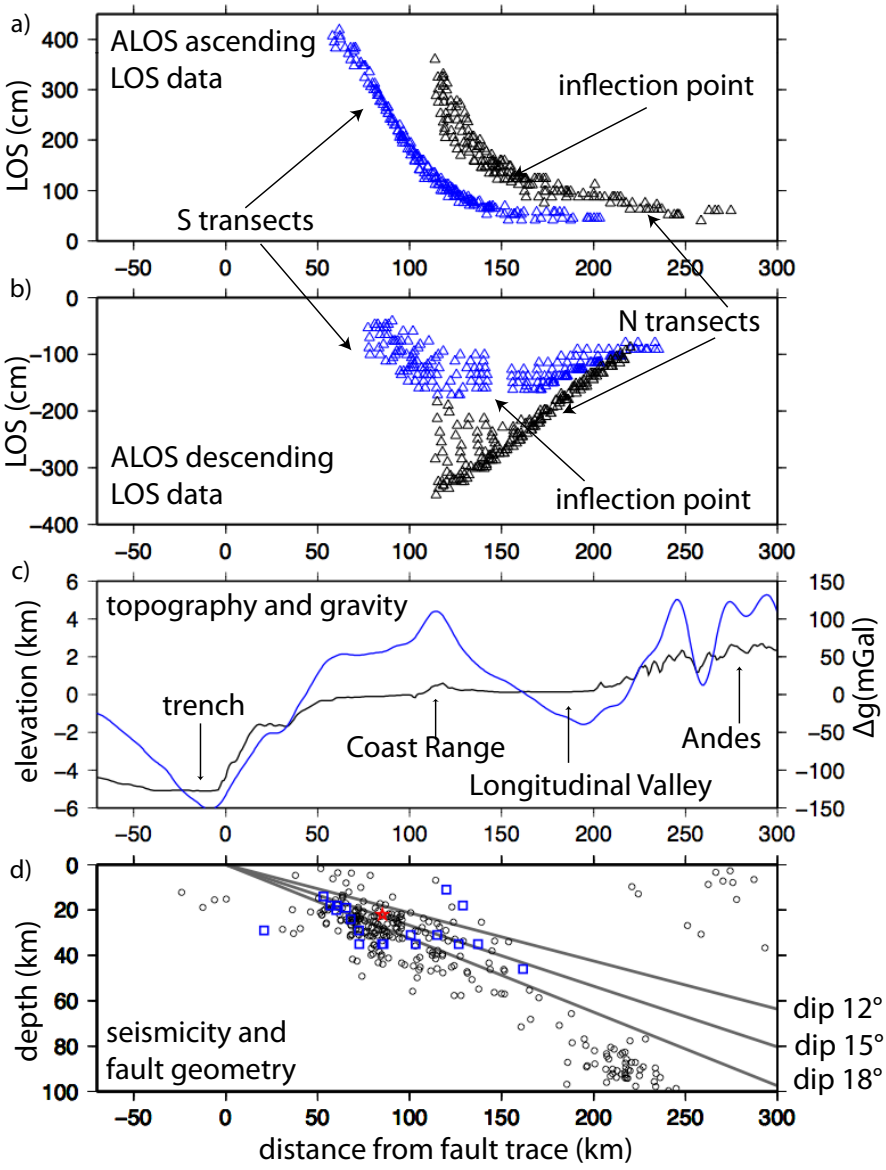

Figure 3.3: Transects of unwrapped ALOS line-of-sight data a) ascending and b) descending. Locations of north (black) and south (blue) transects are shown in Figure 3.2. c) Smoothed topography (black line) and free-air gravity (blue line) profiles over Maule, Chile illustrating major geological features: trench axis, Chilean Coast Range, Longitudinal Valley and High Andes. d) Seismicity and fault geometry in Maule, Chile region. The black circles show the $M > 4$ background seismicity spanning 1960-2007, whose depths are well constrained in EHB bulletin. The red star shows the epicenter of the Maule, Chile earthquake and the blue squares show the locations of the $M > 6$ aftershocks from USGS/NEIC PDE catalog. Three gray lines show the fault plane for 12° , 15° , 18° dip angles used in the slip models. Note the 12° dipping surface lies shallower than the epicenter and much of the background seismicity.

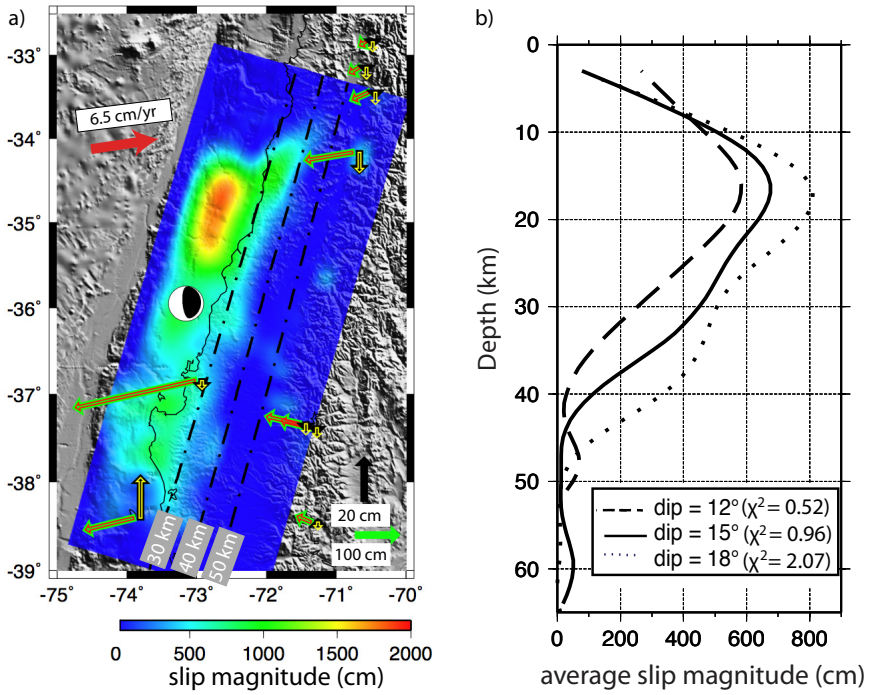

Figure 3.4: a) Coseismic slip model along a 15° dipping fault plane over shaded topography in Mercator projection. Dashed lines show contours of fault depth (they are not exactly parallel because of the map projection). Red fat arrow shows the interseismic convergence vector. The fat green and black arrows show the observed horizontal and vertical displacement of the GPS vectors respectively and the narrow red and yellow arrows show the predicted horizontal and vertical displacement from the coseismic slip model. Note the directions of coseismic slip from the coastal GPS, and the moment tensor is parallel to the interseismic motion vector indicating a significant right-lateral slip component to accommodate the oblique convergence. b) Along-strike averaged slip versus depth for different dip angles. The solid black line (15° dip) shows the preferred slip-depth distribution. The χ^2 misfits for different dip angles are also shown. The possible range of Moho depth is marked by two gray bars. Note the average slip magnitude decreases more or less linearly from $\sim$ 18 km depth to $\sim$ 43 km depth then becomes essentially zero from $\sim 43 - 48$ km depth.

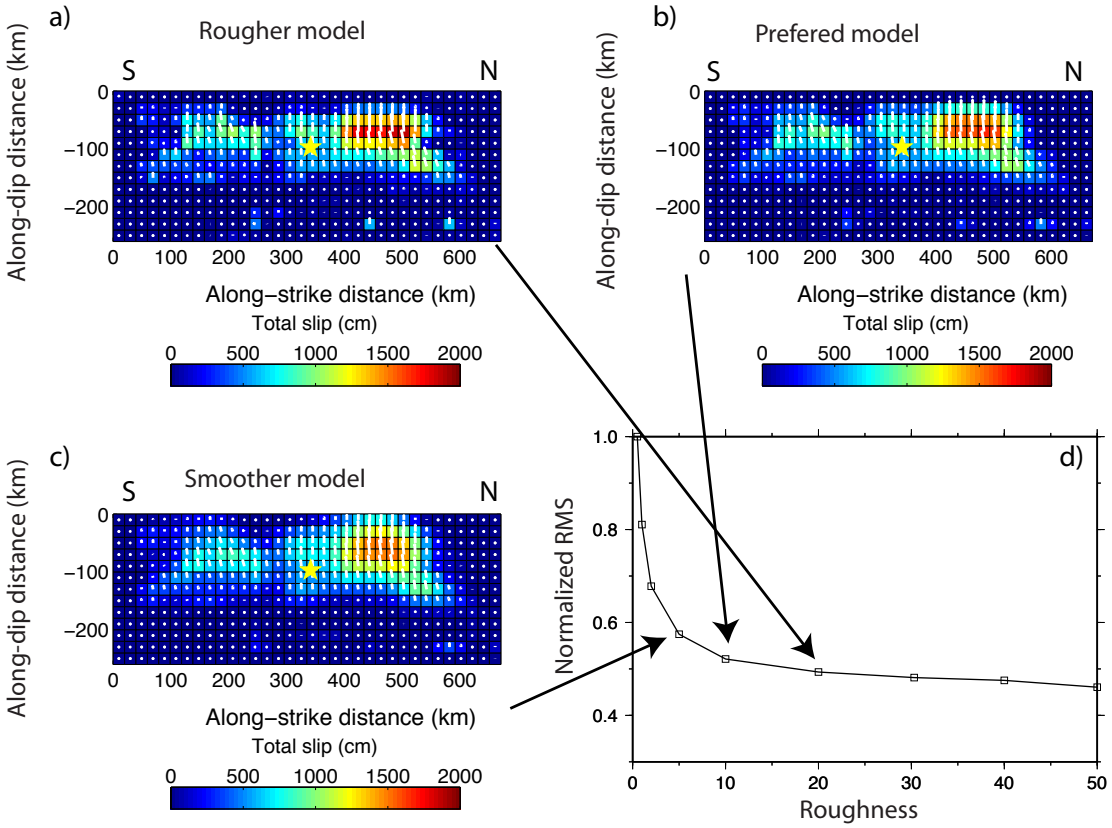

Figure 3.5: Slip models with three different weights on the smoothing function. The total slip magnitude on fault patches are represented by the color. In each slip model, the white lines, which originate from center of the rectangular patches and point outward, illustrate the relative motion of the hanging wall with respect to the footwall (mainly thrust slip with certain right-lateral strike slip in this case). The yellow star is the position of the main shock. a) A rougher model. b) Our preferred model. c) A smoother model. d) Trade-off curve showing the χ^2 misfit versus the roughness.

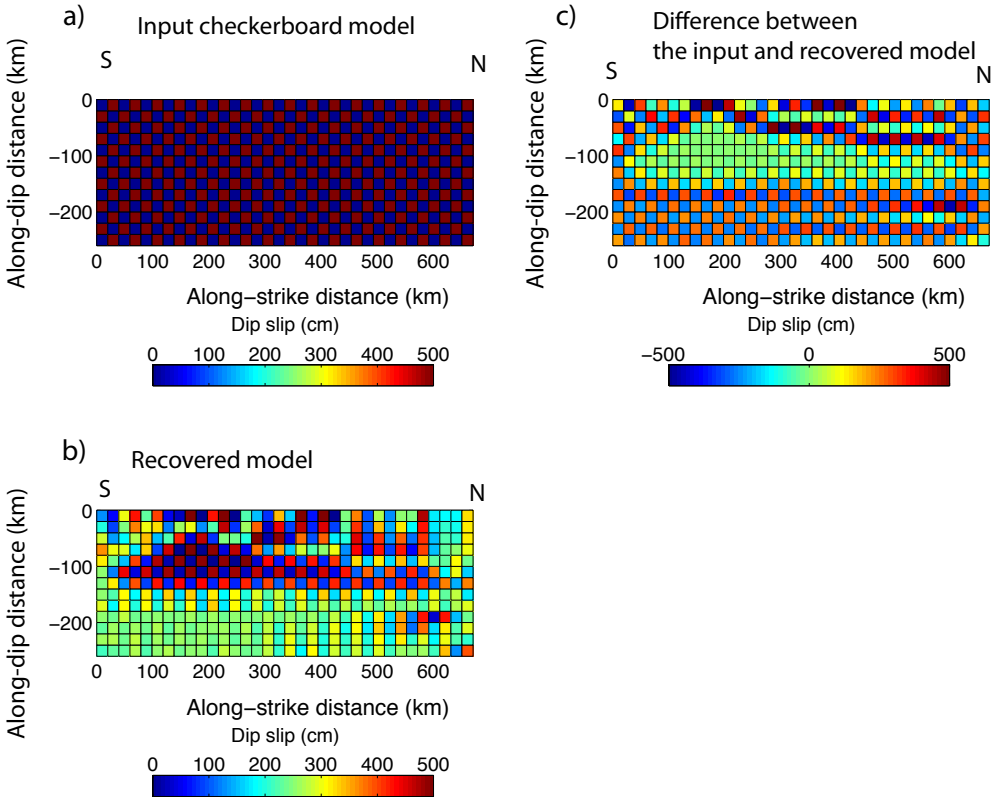

Figure 3.6: Resolution test with checker size of 20 km. a) Synthetic input model has thrust displacement of either zero or 500 cm spaced at 20 km intervals . b) The recovered model. c) The difference between the synthetic input model and the recovered model.

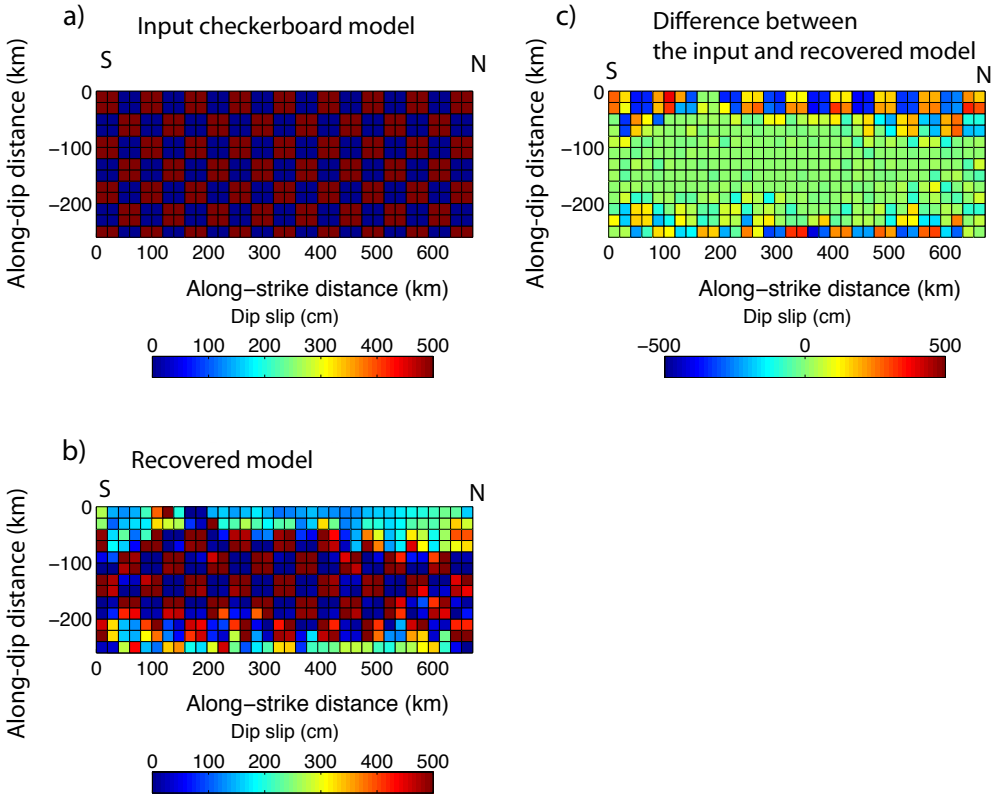

Figure 3.7: Resolution tests with checker size of 40 km. a) Synthetic input model that has displacement of either zero or 500 cm spaced at 40 km intervals for thrust slip. b) The recovered model. c) The difference between the synthetic input model and the recovered model.

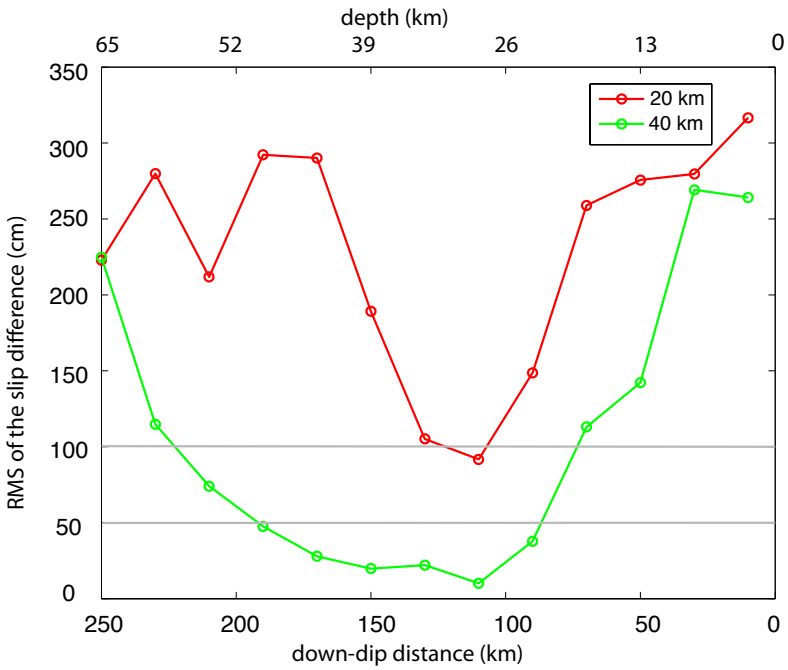

Figure 3.8: Accuracy of slip recovery versus downdip distance for 20 km (red line) and 40 km (green line) checker size. The RMS slip difference is the along-strike average of slip differences shown in Figure 3.6 (red line) and Figure 3.7 (green line). The horizontal axis shows the downdip distance (below) and depth (above). We set 20% RMS difference as the accuracy threshold so in this case the model is resolved at 20 km between downdip distances of 110 and 130 km and the model is resolved at 40 km between downdip distances of 70 and 220 km.

Chapter 4

High-resolution interseismic velocity data along the San Andreas Fault from GPS and InSAR

We compared 4 interseismic velocity models of the San Andreas fault (SAF) based on GPS observations (*McCaffrey*, 2005; *Meade and Hager*, 2005a; *Smith-Konter and Sandwell*, 2009; *Zeng and Shen*, 2010). The standard deviations of the predicted secular velocity from the 4 models are larger north of the San Francisco Bay area, near the Creeping segment in Central California, and along the San Jacinto fault and the East California Shear Zone in Southern California. A coherence spectrum analysis of the secular velocity fields indicates relatively high correlation among the 4 models at longer wavelengths (>15-40 km), with lower correlation at shorter wavelengths. To improve the short-wavelength accuracy of the interseismic velocity model, we integrated InSAR observations, initially from ALOS ascending data (spanning from the middle of 2006 to the end of 2010, totaling more than 1100 interferograms), using a Sum/Remove/Filter/Restore (SURF)

[0]This chapter is a reformatted version of a publication in *Journal of Geophysical Research*: Tong, X., D. Sandwell and B. Smith-Konter, "High resolution interseismic velocity data along the San Andreas fault from GPS and InSAR",118, doi:10.1029/2012JB009442, 2013

approach. The final InSAR line-of-sight (LOS) data match the point GPS observations with a mean absolute deviation of 1.3 mm/yr. We systematically evaluated the fault creep rates along major faults of the SAF and compared them with creepmeters and alignment array data compiled in UCERF2. Moreover, this InSAR LOS dataset can constrain rapid velocity gradients near the faults, which are critical for understanding the along-strike variations in stress accumulation rate and associated earthquake hazard.

4.1 Introduction

The San Andreas fault (SAF) System is northwest trending transform plate boundary between the North America and Pacific plates. Major geological fault traces along the SAF are shown in Figure 4.1 in an oblique Mercator projection. The plate velocity between the North America and Pacific plates is about 45 mm/yr, determined from global plate motion models (*Demets et al.*, 1994, 1990). In Central California, the geological and geodetic slip rates of the SAF consistently suggest that 70-80% of the plate motion is accommodated by the SAF (*Noriega et al.*, 2006; *Rolandone et al.*, 2008). In Southern California, the SAF splays into three main branches, the Elsinore fault, the San Jacinto fault, and the San Andreas fault, which distribute about 45 mm/yr of strike-slip motion over a 200 km region. To the north of the creeping section, the SAF diverges offshore slipping at 25 mm/yr, while the paralleling Hayward and Calaveras faults absorb about 8 mm/yr of the dextral wrenching motion (*Lienkaemper and Borchardt*, 1996; *Segall*, 2002). A recent summary of the geological and geodetic slip rates of the SAF can be found in *Molnar and Dayem* (2010).

GPS measurements across the North American - Pacific Plate boundary are providing decade and longer time-series at 2 to 3 millimeter-level precision from which surface velocity estimates are derived. One of the goals of these models is to provide strain rate estimation and to forecast seismicity rate. Several geodetic research groups have used these point velocity measurements to construct large-scale maps of crustal velocity. Since the typical spacing of GPS stations is about 5-10 km,

an interpolation method or physical model must be used to compute a continuous vector velocity model that can be differentiated to construct a strain-rate map. Four approaches are typically used to develop strain maps: isotropic interpolation, interpolation guided by known faults, interpolation of a rheologically-layered lithosphere, and analytically determined strain rates derived from a geodetically constrained block model in an elastic half space.

The earliest interpolation studies used discrete GPS observations directly to obtain a spatially continuous horizontal velocity field and strain rate (*Frank*, 1966; *Shen et al.*, 1996). This method makes no assumptions on the location of a fault and does not need to solve for fault slip rates and locking depths when characterizing the strain field. Unknown faults (e.g. blind thrust faults), if accommodating enough strain, might be manifested through this method. *Freed et al.* (2007) explored the relationship between occurrence of the M>6 earthquakes and the stress changes induced by coseismic, postseismic, and interseismic deformation. Their interseismic stress accumulation rates were calculated directly from SCEC Crustal Motion Map (CMM3). *Kreemer et al.* (2003) constructed a global model for horizontal velocity and horizontal strain rate over major plate boundaries. They derived the velocity field from a least-squares interpolation method using bi-cubic Bessel splines. *Hackl et al.* (2009) developed a new interpolation procedure to compute strain directly from dense GPS networks and applied it to the interseismic deformation in Southern California and coseismic deformation of earthquakes. While these approaches have produced maps of the 1st order strain rate field, the main issue is that in places where fault location information is not used, the spacing of GPS data is insufficient to accurately map the high strain concentrations along major faults.

The second main strain rate modeling approach uses GPS observations to constrain fault slip rate and locking depths through model parameterization assuming a known set of fault locations. In these studies, model parameters are usually derived from minimization of the residual between the GPS observations and model prediction. An incomplete list of these models follows: *McCaffrey* (2005) represented the active deformation of the southwestern United States with

rotating, elastic-plastic spherical caps. *Meade and Hager* (2005b,a) estimated the moment accumulation rate from an elastic block model of interseismic deformation on the SAF constrained by GPS measurements. *Smith-Konter and Sandwell* (2009) used a semi-analytic viscoelastic earthquake cycle model to simulate the moment accumulation rate and stress evolution of the SAF over a thousand years(*Smith and Sandwell*, 2003, 2004, 2006). *Shen and Jackson* (2005) modeled the surface deformation of Southern California using an elastic block model, which did not strictly enforce the continuity of fault slip rate on adjacent fault segments. *Parsons* (2006) constructed a finite element model of California by considering surface GPS velocity, crustal thickness, geothermal gradient, topography, and creeping faults. *Bird* (2009) incorporated community geologic, geodetic, and stress direction data to constrain the long-term fault slip rates and distributed deformation rates with a finite element model. It is worth noting that a deep dislocation underneath active faults is not a unique representation of the strain accumulation pattern everywhere in California. It has been proposed that the geodetic data may be explained to first order by simple shear across an 135-km-wide shear zone (*Savage et al.*, 1998; *Pollitz and Nyst*, 2005) in the San Francisco Bay region.

A recent analysis of 17 strain-rate models for the SAF has shown that GPS data alone cannot uniquely resolve the rapid velocity gradients near faults (*Hearn et al.*, 2010). The standard deviation of the strain models reveals a large discrepancy close to the fault, which can be caused by the different interpolation schemes used in constructing the strain models from discrete GPS measurements. *Baxter et al.* (2011) investigated the techniques to derive strain from discrete GPS velocity vectors and its inherent limitations. Incorporating Interferometric Synthetic Aperture Radar (InSAR) data along with GPS data has proven to be important to constrain high resolution kinematics over tectonically active regions (*Fialko*, 2006; *Funning et al.*, 2007; *Ryder and Burgmann*, 2008).

In this paper we first evaluate the mean and standard deviation of 4 independent models to show that the GPS-derived interseismic velocity models are coherent at wavelengths greater than 15-40 km. Second, we develop a method to integrate InSAR data with GPS observations to recover the high-resolution interseismic

velocity of the SAF. Third, we evaluate errors in the InSAR Line-Of-Sight (LOS) data by comparing it to GPS measurements. (The InSAR LOS data and their uncertainties are available at `ftp://topex.ucsd.edu/pub/SAF_model/insar`). Finally, we use this dataset to estimate the fault creep rates along the SAF and other major faults systematically and compare these estimation with 115 ground-truth observations such as creepmeters and alignment arrays.

4.2 Evalution of interseismic velocity models based on GPS measurements

To establish the accuracy and resolution of available interseismic velocity models, we compared 4 independent models based primarily on GPS observations. These models are products from a comprehensive strain rate comparison analysis (*Hearn et al.*, 2010) and all the models are accessible through the following ftp site `ftp://topex.ucsd.edu/pub/sandwell/strain/`. The 4 models are:

H-model: *Meade and Hager* (2005a) developed a block model of Southern California constrained by the SCEC CMM3 GPS velocity. This was refined by *Loveless and Meade* (2011). Their block models considered the block rotation and both the fault-parallel and fault-normal steady-state slip on block-bounding faults. They estimated the effective locking depths on some of the fault segments, and used results from previous studies on other fault segments.

M-model: *McCaffrey* (2005) represented active deformation of the southwestern United States with rotating, elastic-plastic spherical caps. The GPS velocity field was modeled as a result of rigid block rotations, elastic strain on block-bounding faults, and slip on faults within blocks (i.e. permanent strain).

Z-model: *Zeng and Shen* (2010) inverted regional GPS observations to constrain slip rates on major faults in California based on Okada solutions. Their model simulates both block-like deformation and elastic strain accumulation.

S-model: *Smith-Konter and Sandwell* (2009) developed a 3-D semi-analytic viscoelastic model to simulate the full earthquake cycle including interseismic deformation, coseismic displacement from past earthquakes, and postseismic relaxation

following earthquakes. The slip rate was adopted from geologic studies and the apparent locking depth was estimated from the regional GPS velocity field. The model is fully 3-D and the vertical component of the GPS vectors is also used in the adjustment. In this study we improve the original model by adding a grid of residual velocity using a spline fitting method (*Hackl et al.*, 2009).

We use two approaches to establish the similarities and differences among these 4 models. First we compute the mean and standard deviations of the horizontal components of the models and then we evaluate the spectral coherence among the models.

4.2.1 Standard deviations

Figure 4.2 shows the mean velocity and standard deviations of the 4 different GPS models. All the models are gridded at 0.01° pixel spacing with the *GMT surface* command. We adjusted each velocity model by subtracting its mean so that they reflect the same reference. The mean value of these models (2.5 mm/yr contour interval) shows a right lateral shear along the SAF and the East California shear zone and transpression motion over the Mojave segment of SAF. At the creeping section, the velocity changes sharply, indicating a low degree of coupling of the fault, while in Southern and Northern California, the right lateral shear motion is taken up by multiple parallel faults. The standard deviation (0.5 mm/yr contour interval) ranges from 0 to 2 mm/yr for both the east and north velocity, except for at the creeping section where it exceeds 3 mm/yr. The smaller standard deviation (<1.0 mm/yr) indicates good agreement among models and larger standard deviation (>1.0 mm/yr) emphasizes the areas of largest discrepancy, such as the creeping section, north of the San Francisco Bay area, the San Jacinto fault and the East California Shear Zone in Southern California. A similar kind of effort to compare independent model results has been carried out in a previous California strain rate comparison (*Hearn et al.*, 2010).

There are several factors that could explain the discrepancies among the GPS models. First, the discrepancies could be caused by the imprecise location of a fault or inaccurate fault dip, which could be resolved by using a more accurate

fault model. On the creeping part of the SAF (e.g. Hayward fault, Calaveras fault, creeping sections over Central California), the fault trace could be more accurately constrained by velocity steps revealed by InSAR observations. Second, the discrepancy could be caused by different locking depth and slip rate used in different models. As shown in Figure 4.2, there is a larger uncertainty among the models north of the San Francisco Bay area. For example, *McCaffrey* (2005) inferred that the Maacama fault has a slip rate of 7.4 mm/yr and has a significant fraction of fault creep. *Smith-Konter and Sandwell* (2009) inverted a 10 mm/yr slip rate and 8.6 km locking depth along the Maacama fault. Likewise, 30 km east of the Maacama fault resides the Green Valley fault. *McCaffrey* (2005) inferred a 7.3 mm/yr slip rate with a large fraction of fault creep along the Green Valley fault (*McCaffrey*, 2005, Figure 3a). *Smith-Konter and Sandwell* (2009) estimated a slip rate of 6.4 mm/yr with a locking depth 5 km along the same fault. This analysis illustrates that the current GPS velocity field is not able to distinguish a shallow locked fault from a creeping fault. For instance, we calculated two fault-parallel velocity profiles by changing the locking depth from 1 km to 5 km, for a constant slip rate of 7 mm/yr. The difference of the velocity profiles reaches a maximum of 1.6 mm/yr at 2 km from the fault trace and decreases to 0.2 mm/yr at 40 km from the fault. Thus high resolution and high precision observations close to the fault are needed to constrain the slip rates and locking depths of parallel faults. Third, in the area where significant surface creep occurs, like the creeping section in Central California, the locking depth is difficult to constrain from GPS alone.

4.2.2 Cross-spectrum analysis

The second method used to establish the similarities and differences among these 4 models was to perform a cross-spectral analysis among pairs of models (Figure 4.3 and 3.4). Based on the above analysis, we expect the model pairs to show good agreement at longer wavelengths and poor agreement at shorter wavelengths. The coherence is a measure of the degree of relationship, as a function of frequency, between two time series. This crossover wavelength is needed to determine the filter wavelength in the GPS/InSAR integration step (section 3.2).

We used Welchs modified periodogram approach (*Welch*, 1967) as implemented in MATLAB to estimate the coherence for 37 LOS profiles crossing the plate boundary. There are three steps in this approach:

1. Project horizontal velocity components into LOS velocity for each of the 4 GPS models. In this cross-spectrum analysis the look direction of radar is taken to be constant (81° azimuth, 37° from vertical). In the InSAR/GPS integration (section 3), we take into account that the look direction of radar varies across satellite track.

2. Extract across-fault profiles spaced at 10-20 km intervals in the north-south direction. Each profile starts at the coastline and extends 300 km inland. The profiles that have gaps (no data) are discarded. We extract 37 profiles from each model (transect lines in Figure 4.3) using linear interpolation with a pixel spacing of 0.2 km.

3. Concatenate the 37 profiles end-to-end to form one vector for each model. Compute the magnitude-squared coherence using Welch's averaged periodogram method. In order to avoid artifacts associated with jumps where the 37 profiles abut each other, we first applied a 300 km long Hanning-tapered window to each profile. Then the periodogram for the 37 profiles were computed and averaged to get the final estimate of the coherence spectrum.

Figure 4.4 shows the coherence as a function of wavenumber for all the possible combinations within the 4 GPS models. Because the profiles only sample 300 km in across-fault distance, the coherence estimated over wavelengths greater than 150 km is not reliable. Below 150 km wavelengths however, the coherence estimates show several interesting features: To first order, the coherence among GPS models is high (>0.8) between wavelengths of 150 and 66 km and then drops to 0.5 at about 20 km wavelengths. This wavelength is expected because it corresponds to the characteristic spacing of the GPS receivers. There is a high coherence of 0.8 at the 33-50 km wavelength among Z, H and S models. In contrast, the coherence between M-model and other models has a relatively low value of 0.55 at the same scale. While all the other models show lower correlation at smaller length scales,

the correlation between Z-model and H-model reaches 0.9 between wavelengths of 1 and 10 km. We suspect that this high coherence reflects the fact that these two models use nearly identical fault geometry and have short wavelength signals that are common at creeping faults. We found that the averaged coherence spectrum falls off to 0.7 approximately at 40 km and to 0.5 at 20 km (Figure 4.4).

4.3 Integration of InSAR and GPS

The approach for combining multiple interferograms of a region with GPS observations has 4 primary steps and is based on a study by *Wei et al.* (2010). The first step is to sum up the available interferograms, keeping track of the total time span of the sum to compute a line-of-sight (LOS) velocity. This stacking will enhance the signal-to-noise ratio because, for example, the residual tropospheric noise is uncorrelated for a time span longer than 1 day (*Williams et al.*, 1998; *Emardson et al.*, 2003). The second step is to project a fine-sampled interseismic velocity field based on the GPS measurements into the line-of-sight (LOS) velocity of the interferogram (Figure 4.5) and to remove this model from the stack. A block model or viscoelastic model is necessary to integrate the sparse GPS velocities with dense InSAR LOS data in the spatial domain. For this study we use a modified version of the S-model to provide a long-wavelength basis for integration of GPS and InSAR. The horizontal components of this velocity model are used in the projection since the vertical component are not well constrained by the current vertical velocity of GPS. The third step is to high-pass filter the residual stack to further suppress errors at length scales much greater than the crossover wavelength. This crossover wavelength was selected based on the coherence analysis above. The final step is to add the GPS-based model back to the filtered stack to recover the full LOS velocity. The acronym for this integration approach is called "SURF" (Sum/Remove/Filter/Restore). As shown in Figure 4.6, it is clear that the recovered InSAR LOS velocity map provides shorter wavelength information not captured by the GPS-based model (compare to Figure 4.5). The details of the result shown in Figure 4.6 are discussed in Section 4.

4.3.1 InSAR data processing

We processed 13 ascending tracks of ALOS PALSAR interferograms spanning from the middle of 2006 to the end of 2010 in preparation for stacking. More than 1100 interferograms were processed to cover the entire SAF. We performed the InSAR data processing and the GPS/InSAR integration using GMTSAR software, which is publicly available from `http://topex.ucsd.edu/gmtsar` (*Sandwell et al.*, 2011). We processed the SAR data on a frame-by-frame basis so that the frame boundaries of the interferograms match seamlessly along track (Figure 4.6). By doing so, we avoided discarding entire tracks of data and still processed other frames along the same track if the pulse repetition frequency (PRF) changes along track or the SAR data in one of the frames were missing or problematic. A summary of the SAR dataset used in the analysis is in Table 4.1. The baseline-time plots of the SAR data used in this study can be accessed through the following site: `ftp://topex.ucsd.edu/pub/SAF_models/insar/basetime`.

The main processing steps are (1) pre-processing, (2) SAR image formation and alignment, (3) interferogram formation and topographic phase correction, (4) phase unwrapping, (5) GPS/InSAR integration. We discuss details of steps 2) to 5) in the following paragraphs. All of these steps are done in the radar coordinates for consistency. After GPS/InSAR integration, we projected the products into geographic coordinates with pixel spacing of 3 arc seconds ($\sim$90 meters) for further analysis.

As shown in an example baseline-time plot (Figure 4.7), the perpendicular baseline of the ALOS satellite drifted from -1000 m to 1000 m (2007 June -2008 April) and then was reset to -7000 m in the middle of 2008, when it then started to drift again. Subsequently, short baseline and long time-span interferograms were not available until the middle of 2010. Unfortunately the satellite stopped working due to power issue in April 2011, so for most frames, fewer than 20 interferograms are available for stacking. The drifting orbit also makes it difficult to align all the images using conventional methods.

As shown in Figure 4.7, the baseline between the two SAR images can reach several thousand meters, thus a direct alignment of the images relying on

the satellite trajectory is difficult. We adopted a "leap frog" approach (*Sandwell and Sichoix*, 2000; *Sandwell et al.*, 2011) to align every image in this baseline-time plot to one image (called "super master"). Taking Figure 4.7 as an example, we first chose an image as "super master" (10024 in this case). We then aligned the images that were close to (i.e. perpendicular baseline <1000 m) the"super master" in the baseline-time domain to the"super master" (marked as Primary match in Figure 4.7). After alignments, the images were registered in the same coordinates as the"super master" within one pixel accuracy, thus they can be treated as new master images (called "surrogate master"). Then we aligned other images (marked as Secondary match in Figure 4.7) that are far from the "super master" in the baseline-time domain to the"surrogate master".

Because the interseismic motion is subtle compared to the atmospheric noise, we chose interferometry pairs with long time intervals (>1 yr) and with small perpendicular baselines (<600 m) to enhance the signal to noise ratio (Figure 4.8). The summations of the perpendicular baselines are minimized to reduce the topographic error (Table 4.1). Topographic phase is removed using digital elevation model obtained from Shuttle Radar Topography Mission (SRTM1) (*Farr et al.*, 2007). The relative height error of SRTM1 over North America is estimated to be 7 meters. In addition, the height measured by SRTM1 is an effective height. In the presence of vegetation or snow or very dry soil, C-band radar waves on board SRTM reflected at a different effective height than the L-band radar on board ALOS (*Farr et al.*, 2007), which can cause an error in DEM on the order of 5-10 meters. The relationship between LOS velocity error dv and the DEM error dh after stacking is: $dv = \frac{4\pi}{\lambda}\frac{\sum B^i_{perp}}{\sum_{i=1}^{N}\Delta t^i} \times \frac{r_e+h}{\rho b \sin\theta} dh$ (*Sandwell et al.*, 2011, Appendix C) , where r_e is radius of the Earth (6371 km), ρ is the distance from the radar satellite to the ground (800 km), b is the distance from the radar satellite to the center of the Earth (7171 km), λ is the radar wavelength (0.236 m), h is the elevation of the ground (1 km), θ is the radar look angle (34 °), i denotes the ith interferogram, N is the total number of interferograms, $\frac{\sum B^i_{perp}}{\sum_{i=1}^{N}\Delta t^i}$ is the summation of perpendicular baseline over the summation of the time span for all the interferograms (10m/10,000 days). See Table 4.1 for exact values used in the

data processing. Using the above representative values denoted in the parenthesis and taking DEM error dh to be 10 meters, we estimated a bias in LOS velocity dv of 0.4 mm/yr. The interferograms were filtered with a Gaussian low-pass filter at 200 meters full wavelength and subsequently subsampled at 2 pixels in range (15.6 meters projected on the ground) by 4 pixels in azimuth (13.2 meters). We then applied a Goldstein filter (*Goldstein and Werner*, 1998) to the interferograms to obtain the final interferogram in wrapped phase.

In order to identify the small-scale deformation signal, we must first eliminate the errors associated with the automatic unwrapping. Sometimes automatic unwrapping provide inaccurate results (known as"phase jumps"), especially where there are cultivated fields, sand dunes, or water. We devised an iterative approach to overcome difficulties that occasionally occur in automatic phase unwrapping of InSAR phase data (Figure 4.9). Initially, we unwrapped the phase of each interferogram using the SNAPHU software (*Chen and Zebker*, 2000) (SNAPHU stands for Statistical-Cost, Network-Flow Algorithm for Phase Unwrapping). Next, we constructed a trend from the unwrapped phase using *GMT functions grdtrend, grdfilter, surface*. Then we removed the trend from the original wrapped phase to derive the "fluctuation phase". If the fluctuation phase is within $\pm\pi$, we add fluctuation to the trend to get a complete unwrapped phase and the unwrapping is done; If not, we re-estimate the trend and iterate. We unwrapped the phase by hand for some extremely difficult cases, like the interferograms over the Imperial Valley.

4.3.2 The SURF approach

After unwrapping the phase of each interferogram, we carried out the GPS/InSAR integration step using the SURF approach (*Wei et al.*, 2010) shown as Figure 4.10. We discuss the advantages of this integration approach in section 3.3. Here we describe each step in detail:

1. **Sum** the unwrapped phase of each interferogram $\phi^i(x, \Delta t^i)$, i denotes the ith interferogram, x is a 2 dimensional spatial variable in radar coordinates. Scale the summation with respect to their corresponding time interval Δt^i

using the formula $\overline{\phi}(x) = \frac{\sum_{i=1}^{N} \phi^i(x,\Delta t^i)}{\sum_{i=1}^{N} \Delta t^i}$, and scale it from phase in radius to velocity in millimeters per year. $\overline{\phi}$ is the average LOS velocity. N is the total number of interferograms. Make a coherence mask (>0.06) from a stack of coherence maps. Make a land mask if applicable. Make a mask to isolate the anomalous deformation signals when necessary. By stacking we cancel out the random atmospheric noise and non-steady ground movement to recover the steady-state interseismic deformation.

2. **Remove** the GPS model $M(x)$ from the stacked phase to obtain the residual phase by $\overline{\phi}(x) - M(x)$, where $M(x)$ is the interseismic velocity model from GPS. The interseismic velocity model *Smith-Konter and Sandwell* (2009) is projected from geographic coordinates (longitude-latitude) into radar coordinates (range-azimuth). The 2-component (local East-North) velocity of each pixel is converted into Line-Of-Sight (LOS) velocity considering variable radar looking directions across track (Figure 4.5).

3. **Filter** the residual phase with a Gaussian high-pass filter $F_{high}(x)$ at the crossover wavelength by $[\overline{\phi}(x) - M(x)] * F_{high}(x)$. *Wei et al.* (2010) used a crossover wavelength of 40 km inferred from typical spacing of GPS sites. We determined the filter wavelength based on a coherence spectrum analysis and found that 40 km is a good choice for the crossover wavelength. The optimal crossover wavelength may vary from location to location and warrants further investigation. The high-pass filtered residual $[\overline{\phi}(x) - M(x)] * F_{high}(x)$ shows the small-scale difference between the InSAR LOS velocity and the GPS model prediction (Figure 4.11).

4. **Restore** the original interseismic velocity model $M(x)$ by adding it back to the filtered residual phase. Thus $V_{InSAR}(x)$ combines the short wavelength signal from InSAR stacking and the long wavelength signal from GPS. Convolution is a linear operator, thus we have: $V_{InSAR}(x) = [\overline{\phi}(x) - M(x)] * F_{high}(x) + M(x) = \overline{\phi}(x) * F_{high}(x) + M(x) * F_{low}(x)$. $F_{low}(x)$ is the corresponding low-pass filter. The error from the GPS-based model after low-pass filtering is reduced to a level of 1 mm/yr as discussed in Section 2, and the

error from InSAR after high-pass filtering is evaluated in step 5.

5. We evaluated the errors in the InSAR data after high-pass filtering by calculating its standard deviations with the formula

$$\sigma_{InSAR}(x) = \frac{\sum_{i=1}^{N}\{[\frac{\phi^i(x,\Delta t^i)}{\Delta t^i} - V_{InSAR}(x)] * F_{high}(x)\}^2}{N} \tag{4.1}$$

Larger uncertainties could be due to unwrapping errors, atmospheric noise or deviations from steady-state ground motion. The standard deviation varies spatially, ranging from <1 mm/yr to > 10 mm/yr for some regions with an average value of ∼3 mm/yr.

4.3.3 Advantage of this GPS/InSAR integration approach

Although there are not many explicit studies on GPS/InSAR integration methods, almost every study using InSAR phase data to retrieve coseismic, postseismic, interseismic and volcanic deformations relies on GPS to correct the long wavelength errors of InSAR phase data. We found that this integration method usually involves interpolation between GPS stations (*Gourmelen et al.*, 2010; *Johanson and Burgmann*, 2005; *Lyons and Sandwell*, 2003; *Peltzer et al.*, 2001; *Ryder and Burgmann*, 2008; *Wei et al.*, 2009). For instance *Johanson and Burgmann* (2005) studied the interseismic slip rate on the San Juan Bautista segments of the SAF. For each interferogram, they removed a GPS-derived interseismic velocity model from interferogram phase data to obtain the so-called residual phase, then they fitted and removed a lower-order polynomial from the residual phase, then they replaced the interseismic model back. The removal of an interseismic velocity model may facilitate phase unwrapping. We call this kind of integration approach remove/correct/restore/stack method. *Wei et al.* (2009) used a very similar method but their procedure is remove/stack/correct/restore. The exact order of the processing steps does not matter much because of the linearity of these operations. In other studies the difference between the interferogram phase data and the co-located GPS measurements are used to construct a linear trend, which is subsequently removed from the InSAR phase data (*Fialko*, 2006; *Lundgren et al.*, 2009).

In this study we used the SURF approach to integrate GPS and InSAR observations. This simple approach is an improvement based on the aforementioned method: the remove/correct/restore/stack method that has been used extensively. Our approach has the following characteristics: 1) this method does not assume a particular form of the orbital error because the exact form of the first- or second-order polynomial is uncertain (*Gourmelen et al.*, 2010). 2) The interpolation between GPS stations is realized by a physical model constrained by GPS velocity (*Smith-Konter and Sandwell*, 2009). 3) The high-pass filter further improves the signal to noise ratio of the stacking by filtering out tropospheric and ionospheric noise. 4) The wavelength of the high-pass filter used in this study is determined by a cross-comparison of 4 independent interseismic velocity models (Figure 4.4). 5) The high-pass filtered residual data provide information on the inaccuracy of the current interseismic models. This method has the potential to be applied and developed in other InSAR studies.

4.4 Evaluation and distribution of LOS results

4.4.1 InSAR LOS velocity map

Figure 4.6a shows the high-resolution interseismic velocity data ($V_{InSAR}(x)$) along the SAF derived from integrating the GPS observations with ALOS radar interferograms (2006.5-2010). The areas with low coherence and large standard deviation ($>$ 6 mm/yr) are masked. Comparing this to GPS model (Figure 4.5), the recovered interseismic velocity data has greater variations including: surface expression of the fault creep, localized deformation pattern related to non-tectonic effect and anomalous velocity gradient near active faults. These details of the velocity field are highlighted by shading the final grid weighted by its gradient. A full resolution version of this LOS velocity map and its relationship to faults and cultural features can be downloaded as a KML-file for Google Earth from the following site: `ftp://topex.ucsd.edu/pub/SAF_models/insar/ALOS_ASC_masked.kmz`. A data file of longitude, latitude, LOS velocity, standard deviations of the LOS velocity, unit vector for LOS can be obtained through `ftp://topex.ucsd.edu/pub/`

`SAF_model/insar`. Next we discuss two sub-regions.

Figure 4.6b shows the broad transition in velocity across the San Andreas and San Jacinto faults that is well studied (*Fialko*, 2006; *Lundgren et al.*, 2009). Besides this large-scale feature, we note several interesting small-scale features. Shallow fault creep is apparent across the San Andreas fault (∼4 mm/yr) near the Salton Sea (*Lyons and Sandwell*, 2003), as well as across the Superstition Hills fault (∼3 mm/yr) (*Wei et al.*, 2009). There are several areas of rapid localized subsidence possibly due to groundwater extraction. For example, there is a large subsidence region around Indio, CA where subsidence has been documented by *Sneed and Brandt* (2007). Other prominent examples of anomalous velocity occur along the Coachella valley west of the SAF where prominent subsidence at >30 mm/yr, and uplift of ∼10 mm/yr just north of the Salton Sea, is observed (see Figure 4.6b). There is an interesting subsidence confined by a "step-over" structure along the San Jacinto fault (*Wisely and Schmidt*, 2010). The subsidence rate in this "step-over" reaches as high as ∼18 mm/yr, which is too large compared to the expected signal from tectonic extension. Localized subsidence is also apparent at Obsidian Butte (∼14 mm/yr) to the south of the Salton Sea (*Eneva and Adams*, 2010).

Figure 4.6c shows the sharp velocity gradient across the creeping section, as well as the Calaveras fault along the central part of the SAF (*Rosen et al.*, 1998; *Johanson and Burgmann*, 2005). From this map we identify that the southern end of the creeping section is at a "step-over" south to the Parkfield region (Figure 4.6c). We divided the creeping section into 3 segments: northern, central, and southern segments and took profiles across the fault. Three profiles are shown in Figure 4.13. InSAR observations resolved the creeping signal within 10 km from the fault trace. On the northern segment, the creeping section is creeping at ∼4 mm/yr in LOS (∼14 mm/yr in horizontal). The Paicines segment of the Calaveras fault (5 km to the east of the SAF) is also creeping at 3-4 mm/yr in LOS. On the central segment of the creeping section, the ∼7 mm/yr creep rate in LOS (∼23 mm/yr in horizontal) is well recovered. On the southern segment of the creeping section, InSAR detects anomalous asymmetric ground motion within 3 km west of

the fault zone. From Figure 4.6c, the rate of the motion is about -12 mm/yr near the fault trace and decrease to -6 mm/yr just 3 km west of the fault. The gradient associated with this LOS velocity change is 2mm/yr/km, thus if we attribute this anomaly to horizontal simple shear in the vicinity of the fault zone and scale the LOS velocity into horizontal motion, the shear strain rate is 6 microstrain/yr. This large strain rate could be caused by the inelastic response of the fault zone material. Due to the ambiguity of the InSAR LOS direction, we could not detect if the ground is moving horizontally or vertically. Vertical motion could be caused by fluid flow within the porous brittle fault zone (*Byerlee*, 1993; *Wisely and Schmidt*, 2010). As far as we know, this peculiar deformation signal on the creeping section and its cause have not been understood by previous workers. This apparent anomaly could also be caused by artifacts in the radar interferograms, such as a change in the surface reflective property. With additional ERS or Envisat satellite data or GPS data, it might be possible to resolve this issue.

4.4.2 Comparison with GPS LOS data

We compared the recovered LOS velocity $V_{InSAR}(x)$ with 1068 co-located GPS measurements [*T. Herring, personal communication*] to investigate the accuracy of $V_{InSAR}(x)$. We denote the projected GPS velocity vectors and their standard deviations as $V_{GPS}(x)$ and $\sigma_{GPS}(x)$. These are projected into the LOS direction using the precise orbital information from each satellite track. We divide our comparison results into two groups depending on whether the vertical velocity of the GPS vectors are included in the projection. The results are summarized in Figure 4.14. Figure 4.14a shows the histogram of the differences between the recovered LOS velocity and GPS measurements $V_{diff}(x) = V_{GPS}(x) - V_{InSAR}(x)$. The standard deviation and the mean absolute deviation of $V_{diff}(x)$ are 4.0 mm/yr and 2.3 mm/yr respectively. Figure 4.14c shows the scatter plot between $V_{InSAR}(x)$ and $V_{GPS}(x)$. As expected, these two measurements are linearly correlated and the normalized correlation coefficient is 0.66 (1 means perfect correlation). Figure 4.14e shows that the uncertainties of the two measurements $\sigma_{GPS}(x)$ and $\sigma_{InSAR}(x)$ are not correlated as their correlation coefficient is only -0.05. The estimate of

$\sigma_{InSAR}(x)$ includes seasonal effects that vary annually or semi-annually but the estimate of $\sigma_{GPS}(x)$ has these effects removed. When only the horizontal components of the GPS velocity are used in the projection (Figure 4.14b, 3.14d, 3.14f), the standard deviation of $V_{diff}(x)$ reduces to 1.9 mm/yr, its mean absolute deviations is reduced to 1.3 mm/yr, and the correlation coefficient between GPS and InSAR measurements increases to 0.90.

Since the InSAR data contains both signal and noise, we investigated how spatial averaging can improve the signal-to-noise ratio of the LOS velocity. A common way to improve the signal-to-noise ratio is to apply a moving-average window with a designated window size. We used the *GMT blockmedian* command to average LOS velocity $V_{InSAR}(x)$ at different spatial scales and then computed the standard deviations of $V_{diff}(x)$. Figure 4.15 shows how the standard devations of $V_{diff}(x)$ vary as a function of spatial averaging. We present both the standard deviation and the mean absolute deviation of $V_{diff}(x)$. We consider the projected LOS velocity from GPS vectors both with and without vertical component. For the comparison using horizontal components of the GPS data, the mean absolute deviation of $V_{diff}(x)$ reduces from 1.5 mm/yr to 1.1 mm/yr after spatial averaging the InSAR data at 3 arcminutes ($\sim$6 km in distance) and remains constant for bigger average windows. For the comparison including vertical GPS velocity the spatial averaging hardly changes the fit to the GPS data. As shown in Figure 4.15, including the vertical component of GPS velocity degraded the fit by $\sim$25-50% compared to the case with only horizontal components, which could be caused by larger uncertainties in the vertical component of GPS data.

4.4.3 Power spectrum

The InSAR data adds significant short wavelength noise and signal to the GPS-only model. We calculated the power spectrum (Figure 4.16a) of the GPS model and the LOS data, as well as their coherence spectrum (Figure 4.16b). Since estimating the power spectrum at a wavelength of 100 km requires a swath longer than 200 km, 12 long profiles, instead of 37 profiles, in Southern California were averaged to obtain a reasonable spectrum (marked in Figure 4.3). At long

wavelengths, the two spectra are at similar magnitude but their fall-off rates differ (Figure 4.16a). A power-law fitting to the power spectrum suggests that the spectrum of the GPS model falls off as $f^{-5.5}$, while the spectrum of the InSAR data falls off as $f^{-1.8}$ where f is the wavenumber. Although the power in the InSAR data could also be due to noise (i.e. atmosphere and ionosphere noise), many small-scale features, such as localized subsidence and fault creep significantly contribute to the power over the short wavelengths, which could explain the difference in the fall-off rate. Figure 4.16b shows the coherence spectrum of the GPS model and the InSAR LOS velocity. The coherence reaches 0.95 at 100 km wavelengths, then decreases to below 0.2 at 15-40 km wavelength. This characteristic of the coherence spectrum is expected because the recovered lnSAR LOS data contains the short wavelength signal not captured by the GPS.

4.4.4 Influence of the GPS model

The approach of combining GPS and InSAR relies on a model to interpolate the GPS-derived vector velocity field to the full resolution of the InSAR LOS data. Our premise is that the long-wavelength components of the model (> 40 km) are well constrained by the GPS so the choice of the model should not have a significant effect on the final LOS data. To investigate the effects of the model selection, we repeated the above GPS/InSAR integration analysis using Z-model, instead of S-model. In both cases the vector velocities of the models were adjusted at long wavelengths to better match the GPS data so the residual misfits on the horizontal components are 1.8 mm/yr and 1.6 mm/yr for the S and Z-models respectively. The differences between the two models projected into the LOS are shown in Figure 4.17a. As expected there are large differences along the faults and in areas of high strain rate where the GPS spacing is insufficient to capture the full spatial resolution. In contrast, the differences between the two models after the integration of the InSAR data is smaller than 1 mm/yr, especially far from the faults (Figure 4.17b). There are two regions of larger difference: one along the Creeping Section and the other to the north of the Carrizo Plain. These are the areas where the S and Z-models show larger initial disagreements perhaps due to differences in fault

position or locking depth. However, away from these areas the differences between the two models after integration are usually smaller than 1 mm/yr suggesting the analysis is not very sensitive to the choice of the long-wavelength starting velocity field.

4.5 Fault creep

We used the InSAR LOS data to estimate surface fault creep rate along the SAF system. Although many previous InSAR studies have measured fault creep rate over limited areas, this analysis is the first to provide comprehensive creep rate estimates for all the major faults of the SAF system over the time interval of the ALOS data acquisition 2006.5 to 2010. In addition to estimating creep rate, we also provide uncertainties and show comparisons with ground-truth measurements (Figure 4.18) such as GPS, alignment arrays (AA), creepmeters (CM) and cultural offsets (Cult) (*Wisely et al.*, 2008). We performed the above analysis for the SAF, Maacama fault, Bartlett Springs fault, Concord fault, Rodgers Creek fault, Calaveras fault, Hayward fault, Garlock fault, San Jacinto fault, and Superstition Hills fault. The creep rate estimates, their geographic coordinates, and their uncertainties are summarized in Table 4.2.

4.5.1 Estimating fault creep rate

Here we record the best-fit creep rate across the fault trace from InSAR LOS velocity profiles. We used the method described by *Burford and Harsh* (1980) to determine the best-fit rates. The creep rate is quantified as an offset of the intercepts of the two best-fit linear functions (Figure 4.18 inset) at the fault trace (0 km distance). We took profiles of the high-resolution velocity grid perpendicular to fault strike. The profiles were spaced at 0.002° intervals in longitude along fault strike. The sampling interval across the fault was 0.2 km for 1 km on either side of the fault. The centers of the profiles were carefully chosen to reflect small bending sections of the fault traces. Then we averaged the profiles every 10 km along the fault strike. For each averaged profile, there were 5 LOS velocity data points on

either side of the fault. In this analysis, we assumed no vertical motion across fault. We scaled the LOS velocity into horizontal direction considering variation of the fault strike. The RMS of the residuals after linear regression was taken to be the error in the creep rate. We avoided making estimation if there were more than 2 data points missing in the averaged profiles on either side of the fault.

We then compared our estimates with the compilation of creep measurements from *Wisely et al.* (2008) from various instruments (GPS, AA, CM, Cult) along the SAF (Figure 4.18). It should be noted that the InSAR measurement of fault creep represents the velocity difference on a scale of 200-300 m across the fault. In contrast, creepmeters and alignment arrays measure the velocity difference over a shorter distance of typically tens of meters to ∼100 meters. Therefore, one would expect differences with the InSAR estimates being bigger unless the creep is really confined to a very small distance from the fault. Also note that the time period of these measurements is usually different. The alignment array surveys used in this comparison are mostly carried out in the 1970s and 1980s and while the GPS surveys and the InSAR observations are more recent and span shorter time period. Despite these limitations, we found that the match between these independent measurements is satisfactory.

4.5.2 Creep rate results

The InSAR-detected surface creep rates on the SAF are shown in Figure 4.18, along with records of the creep rates by other ground-based instruments. We did not find any significant creep signal on the SAF north of the Coachella segment and south of Parkfield. The Creeping segment, covered by dense alignment arrays and other instruments, provides a detailed kinematics of the fault creep (*Brown and Wallace*, 1968; *Burford and Harsh*, 1980; *Burford*, 1988; *Titus et al.*, 2006). As shown in Figure 4.18b, we found good agreement between the InSAR observations and the established measurements: creep starts at a "step-over" south of Parkfield and then increases northward. At Parkfield, the creep rate reaches 13 mm/yr. Between Monarch Peak and Parkfield, the creep rates are 25-30 mm/yr, which is compatible with the differential GPS survey by *Titus et al.* (2005) and

alignment array surveys by *Burford and Harsh* (1980). It is noteworthy that north of Monarch Peak (latitudes 36.2-36.4), close to the Smith Ranch (Figure 4.6b), the creep estimates from InSAR are approximately 20-25 mm/yr, which is lower than the alignment array (AA) surveys of *Burford and Harsh* (1980) by 10 mm/yr. This discrepancy is somewhat unexpected and we discuss it in the following paragraphs.

For creep rates obtained by alignment array method (AA), two different methods should be distinguished. In the study by *Burford and Harsh* (1980), two slip rates (best-fit rates and endpoint rates) are reported from repeated alignment array surveys on the SAF in Central California. The rates from the endpoint method are generally higher than the best-fit rates, sometimes by as large as 10 mm/yr (*Burford and Harsh*, 1980, Table 1). *Burford and Harsh* (1980) used an example of simple shear distributed across the entire alignment array to justify that the best-fit rates underestimate the amplitude of actual creep. *Titus et al.* (2005) reported two different rates over the creeping section. They preferred the best-fit rate as a more robust method because it is less sensitive to noise in one single measurement. The best-fit rates reflect the amount of creep within the main slip zone and the endpoint rates probably include auxiliary fractures close to the main slip zone (*Burford and Harsh*, 1980, Figure 2).

At the Smith Ranch site, the endpoint rates from *Burford and Harsh* (1980, Table 1) are 10mm/yr larger than their best-fit rates. *Titus et al.* (2005, 2006) investigated this issue with GPS surveys and they found an average slip rate of 25 mm/yr at the fault, slower than the geological slip rate by about 10 mm/yr. The independent creep observation from InSAR in this study lends further support to the result from GPS survey (*Titus et al.*, 2006). The lower creep rate suggests that over the central segment of the creeping section the slip rate at the shallow portion of the crust is lower than the slip rate at depth (35 mm/yr) (*Ryder and Burgmann*, 2008; *Rolandone et al.*, 2008).

To the north of the creeping section, the InSAR-derived creep rates along SAF transition gradually to lower values as the other parallel faults, like the Calaveras fault, the Rodgers Creek fault and the Maacama fault show signs of shallow fault creep. The creep estimates north of the San Francisco Bay area are contam-

inated by noise but in general they agree with previous results (*Galehouse and Lienkaemper*, 2003; *Funning et al.*, 2007; *McFarland et al.*, 2009). *Funning et al.* (2007) found evidence for shallow fault creep at a rate up to 6 mm/yr along the Rodgers Creek fault. Our study recovered a creep rate up to 3.8 mm/yr along the Rodgers Creek fault (Table 4.2). *McFarland et al.* (2009) recovered creep rates of the faults of the San Francisco Bay region using theodolite measurements. They found the maximum creep rates along the Rodgers Creek fault to be 4.2 mm/yr. *McFarland et al.* (2009) has found that the creep rates along the Maacama fault to be from 1.1 to 5.7 mm/yr. In this study we found that the creep rates along the Maacama fault varies from 0 to 8 mm/yr though the uncertainties are relatively large. As shown in Figure 4.18, certain estimates of creep rates are negative, which could suggest left-lateral creep or vertical movement across certain faults, however most of these negative rates could reflect negligible surface creep when considering their uncertainties.

Louie et al. (1985) surveyed 3 sites along the Garlock fault with alignment array methods. They found that the site near Cameron on the west Garlock fault experienced a left-lateral creep of >4 mm/yr; two sites on the east Garlock fault exhibited no creep. The InSAR-derived creep estimates supplement the alignment arrays that sparsely sampled the Garlock fault. The LOS direction is more sensitive to the horizontal motion along the east-west trending fault compared to the northwest-southeast trending SAF. As shown in Table 4.2, we found no significant creep (< 2 mm/yr) along the Garlock fault from InSAR.

The San Jacinto fault is another fault that is not well instrumented with creep measurements. On the northern section of the San Jacinto fault, we found no significant creep (< 2 mm/yr), consistent with alignment array survey at the Clark fault at Anza and the Claremont fault at Colton by *Louie et al.* (1985). *Louie et al.* (1985) documented aseismic slip on the Coyote Creek fault at Baileys Well with a rate of 5.2 mm/yr since 1971. The InSAR data shows an average creep rate of 8 mm/yr at the same location, in agreement with previous measurements (*Louie et al.*, 1985).

We computed the difference of the creep rates between InSAR and UCERF2

at the corresponding locations along the SAF and other major faults. We utilize 115 creep data measurements for this comparison, ranging from 0 to 30 mm/yr. Taking the creep rate observations such as creepmeters and alignment arrays to be ground-truth, the overall accuracy of the InSAR-derived creep rates can be evaluated as the standard deviation of the creep rates difference, which is 4.6 mm/yr (Figure 4.19). The mean absolute deviation, which is less sensitive to outliers, is 3.5 mm/yr. A linear correlation with correlation coefficient of 0.86 is found between the InSAR data and the ground-truth observations.

4.5.3 Creep rates from the Painted Canyon GPS survey

The surface creep rate at the Southern SAF Coachella segment near Painted Canyon is estimated to be 4-5 mm/yr from InSAR (Figure 4.18), whereas the rate from alignment arrays and creepmeters for the period of the 1970s to 1980s (*Louie et al.*, 1985) is about 2 mm/yr. It is fortunate that 32 GPS monuments at Painted Canyon were surveyed in February 2007 and February 2010 by geophysicists from UCSD. A. Sylvester from UCSB installed most of the benchmarks in the 1980s for repeated leveling surveys. The 3 year period of separation between the two surveys ensures that the differential displacement across the SAF exceeds the noise level (*Genrich and Bock*, 2006). As shown in Figure 4.20, the creep rate is approximately 4.5 mm/yr and there is a 300 m wide deformed zone near the fault trace. No apparent fault-perpendicular velocity or vertical velocity can be distinguished. The excellent agreement between the InSAR and GPS observations validates our assumption that, at least in this area, there is negligible fault-perpendicular motion or vertical motion across the fault when projecting the radar LOS direction into horizontal motion.

This difference between the creep rate from 1970s to 1980s and the creep rate from 2007 to 2010 could be explained by the temporal variation of the surface creep. The geological creep rate (*Sieh and Williams*, 1990) in the past 300 years is 2-4 mm/yr. The dense GPS array at Painted Canyon at almost the same time period of InSAR confirms an accelerated creep rate of 4-5 mm/yr. The non-steadiness of creep on active creeping faults is not a unusual phenomenon and it can

be, in general, attributed to a stress perturbation triggered by nearby earthquakes (*Lyons and Sandwell*, 2003; *Lienkaemper and Borchardt*, 1996). We suspect that the creep rate from InSAR includes triggered creep from the 2010 El Mayor - Cucapah earthquake.

4.6 Conclusions

Current interseismic velocity models based on GPS measurements alone cannot resolve features with short wavelengths (<15-40 km). L-band InSAR data is contaminated by errors at longer wavelengths from ionosphere, orbit (plane), and the atmosphere. To remedy these inadequacies, we recovered the interseismic deformation along the entire San Andreas fault at a spatial resolution of 200 meters by combining GPS and InSAR observations using a Sum/Remove/Filter/Restore (SURF) approach. The integration uses a dislocation-based velocity model to interpolate the Line-Of-Sight (LOS) velocity at the full resolution of the InSAR data in radar coordinates. The residual between the model and InSAR LOS velocity were stacked and high-pass filtered, then added back to the model. The filter wavelength is determined by a coherence spectrum analysis of 4 independent interseismic models. Future research should involve a spatially variable crossover wavelength. The LOS velocity data are compared against 1068 GPS velocity measurements. These LOS velocity data and standard deviations are available to modeling groups for future use in their models. We have used these data to systematically estimate fault creep rate along the SAF and 8 major faults and found a general agreement between InSAR and 115 published creep rate measurements. Our next step to advance this work will be to analyze, in detail, the LOS data away from the fault to estimate shallow moment release rate along major segments of the SAF.

References

Baxter, S. C., S. Kedar, J. W. Parker, F. H. Webb, S. E. Owen, A. Sibthorpe, and D. A. Dong (2011), Limitations of strain estimation techniques from discrete deformation observations, *Geophysical Research Letters*, *38*(L01305), doi: 10.1029/2010GL046028.

Bird, P. (2009), Long-term fault slip rates, distributed deformation rates, and forecast of seismicity in the western United States from joint fitting of community geologic, geodetic, and stress direction data sets, *Journal of Geophysical Research-Solid Earth*, *114*(B11403), doi:10.1029/2009JB006317.

Brown, R. D. J., and R. E. Wallace (1968), Current and historic fault movement along the San Andreas fault between Paicines and Camp Dix, California, in *Conference on Geologic Problems of the San Andreas Fault System*, vol. 11, edited by W. R. Dickinson and A. Grantz, pp. 22–39, Stanford University Publ. Geol. Sci.

Burford, R. O. (1988), Retardations in fault creep rates before local moderate earthquakes along the San-Andreas fault system, central California, *Pure and Applied Geophysics*, *126*(2-4), 499–529, doi:10.1007/BF00879008.

Burford, R. O., and P. W. Harsh (1980), Slip on the San-Andreas-fault in central California from alignment array surveys, *Bulletin of the Seismological Society of America*, *70*(4), 1233–1261.

Byerlee, J. (1993), Model for episodic flow of high-pressure water in fault zones before earthquakes, *Geology*, *21*(4), 303–306, doi:10.1130/0091-7613.

Chen, C. W., and H. A. Zebker (2000), Network approaches to two-dimensional phase unwrapping: Intractability and two new algorithms, *Journal of the Optical Society of America a-Optics Image Science and Vision*, *17*(3), 401–414, doi: 10.1364/JOSAA.17.000401.

Demets, C., R. G. Gordon, D. F. Argus, and S. Stein (1990), Current plate motions,

Geophysical Journal International, *101*(2), 425–478, doi:10.1111/j.1365-246X.1990.tb06579.x.

Demets, C., R. G. Gordon, D. F. Argus, and S. Stein (1994), Effect of recent revisions to the geomagnetic reversal time-scale on estimates of current plate motions, *Geophysical Research Letters*, *21*(20), 2191–2194, doi:10.1029/94GL02118.

Emardson, T. R., M. Simons, and F. H. Webb (2003), Neutral atmospheric delay in interferometric synthetic aperture radar applications: Statistical description and mitigation, *Journal of Geophysical Research-Solid Earth*, *108*(B5), doi:10.1029/2002JB001781.

Eneva, M., and D. Adams (2010), Modeling of surface deformation from satellite radar interferometry in the Salton Sea geothermal field, California, *Geothermal Resources Council Transactions*, *34*, 527–534.

Farr, T. G., P. A. Rosen, E. Caro, R. Crippen, R. Duren, S. Hensley, M. Kobrick, M. Paller, and E. R. et al. (2007), The shuttle radar topography mission, *Reviews of Geophysics*, *45*(2), doi:10.1029/2005RG000183.

Fialko, Y. (2006), Interseismic strain accumulation and the earthquake potential on the southern San Andreas fault system, *Nature*, *441*(7096), 968–971, doi:10.1038/nature04797.

Frank, F. C. (1966), Deduction of earth strains from survey data, *Bulletin of the Seismological Society of America*, *56*, 35–42.

Freed, A. M., S. T. Ali, and R. Burgmann (2007), Evolution of stress in southern California for the past 200 years from coseismic, postseismic and interseismic stress changes, *Geophysical Journal International*, *169*(3), 1164–1179, doi:10.1111/j.1365-246X.2007.03391.x.

Funning,G.J.., R. Burgmann, A. Ferretti, F. Novali and A. Fumagalli (2007), Creep on the Rodgers Creek fault, northern San Francisco Bay area from a 10 year PS-InSAR dataset, *Geophysical Research Letters*, *34*(19), doi:10.1029/2007GL030836.

Galehouse, J. S., and J. J. Lienkaemper (2003), Inferences drawn from two decades of alinement array measurements of creep on faults in the San Francisco Bay region, *Bulletin of the Seismological Society of America*, *93*(6), 2415–2433, doi: 10.1785/0120020226.

Genrich, J. F., and Y. Bock (2006), Instantaneous geodetic positioning with 10-50 hz GPS measurements: Noise characteristics and implications for monitoring networks, *Journal of Geophysical Research-Solid Earth*, *111*(B3), doi:10.1029/ 2005JB003617.

Goldstein, R. M., and C. L. Werner (1998), Radar interferogram filtering for geophysical applications, *Geophysical Research Letters*, *25*(21), 4035–4038, doi: 10.1029/1998GL900033.

Gourmelen, N., F. Amelung, and R. Lanari (2010), Interferometric synthetic aperture radar-GPS integration: Interseismic strain accumulation across the Hunter Mountain fault in the eastern California shear zone, *Journal of Geophysical Research-Solid Earth*, *115*(B09408), doi:10.1029/2009JB007064.

Hackl, M., R. Malservisi, and S. Wdowinski (2009), Strain rate patterns from dense GPS networks, *Natural Hazards and Earth System Sciences*, *9*(4), 1177–1187.

Hearn, E. H., K. Johnson, and W. Thatcher (2010), Space geodetic data improve seismic hazard assessment in California: Workshop on incorporating geodetic surface deformation data into UCERF3; Pomona, California, April 2010, *Eos Trans. AGU*, *91*(38), 336, doi:10.1029/2010EO380007.

Johanson, I. A., and R. Burgmann (2005), Creep and quakes on the northern transition zone of the San Andreas fault from GPS and InSAR data, *Geophysical Research Letters*, *32*(14), doi:10.1029/2005GL023150.

Kreemer, C., W. E. Holt, and A. J. Haines (2003), An integrated global model of present-day plate motions and plate boundary deformation, *Geophysical Journal International*, *154*(1), 8–34, doi:10.1046/j.1365-246X.2003.01917.x.

Lienkaemper, J. J., and G. Borchardt (1996), Holocene slip rate of the Hayward fault at Union city, California, *Journal of Geophysical Research-Solid Earth*, *101*(B3), 6099–6108, doi:10.1029/95JB01378.

Louie, J. N., C. R. Allen, D. C. Johnson, P. C. Haase, and S. N. Cohn (1985), Fault slip in southern-California, *Bulletin of the Seismological Society of America*, *75*(3), 811–833.

Loveless, J. P., and B. J. Meade (2011), Stress modulation on the San Andreas fault by interseismic fault system interactions, *Geology*, *39*(11), 1035–1038, doi: 10.1130/G32215.1.

Lundgren, P., E. A. Hetland, Z. Liu, and E. J. Fielding (2009), Southern San Andreas-San Jacinto fault system slip rates estimated from earthquake cycle models constrained by GPS and interferometric synthetic aperture radar observations, *Journal of Geophysical Research-Solid Earth*, *114*(B02403), doi: 10.1029/2008JB005996.

Lyons, S., and D. Sandwell (2003), Fault creep along the southern San Andreas from interferometric synthetic aperture radar, permanent scatterers, and stacking, *Journal of Geophysical Research-Solid Earth*, *108*(B1), doi:10.1029/ 2002JB001831.

McCaffrey, R. (2005), Block kinematics of the pacific-north america plate boundary in the southwestern United States from inversion of GPS, seismological, and geologic data, *Journal of Geophysical Research-Solid Earth*, *110*(B07401), doi: 10.1029/2004jb003307.

McFarland, F.S., J. J. Lienkaemper and S. J. Caskey (2009), Data from theodolite measurements of creep rates on San Francisco Bay Region faults, California, 1979-2011 *Tech. rep.*, *Open File Rep. 2009-1119*, U.S. Geological Survey.

Meade, B. J., and B. H. Hager (2005a), Block models of crustal motion in southern California constrained by GPS measurements, *Journal of Geophysical Research-Solid Earth*, *110*(B3), doi:10.1029/2004JB003209.

Meade, B. J., and B. H. Hager (2005b), Spatial localization of moment deficits in southern California, *Journal of Geophysical Research-Solid Earth*, *110*(B4), B04,402, doi:10.1029/2004JB003331.

Molnar, P., and K. E. Dayem (2010), Major intracontinental strike-slip faults and contrasts in lithospheric strength, *Geosphere*, *6*(4), 444–467, doi:10.1130/GES00519.1.

Noriega, G. R., J. R. Arrowsmith, L. B. Grant, and J. J. Young (2006), Stream channel offset and late holocene slip rate of the San Andreas fault at the Van Matre ranch site, Carrizo plain, California, *Bulletin of the Seismological Society of America*, *96*(1), 33–47, doi:10.1785/0120050094.

Parsons, T. (2006), Tectonic stressing in California modeled from GPS observations, *Journal of Geophysical Research-Solid Earth*, *111*(B3), B03,407, doi:10.1029/2005JB003946.

Peltzer, G., F. Crampe, S. Hensley, and P. Rosen (2001), Transient strain accumulation and fault interaction in the eastern California shear zone, *Geology*, *29*(11), 975–978, doi:10.1130/0091-7613.

Pollitz, F. F., and M. Nyst (2005), A physical model for strain accumulation in the san francisco bay region, *Geophysical Journal International*, *160*(1), 302–317, doi:10.1111/j.1365-246X.2005.02433.x.

Rolandone, F., R. Burgmann, D. C. Agnew, I. A. Johanson, D. C. Templeton, M. A. D'alessio, S. J. Titus, C. Demets, and B. Tikoff (2008), Aseismic slip and fault-normal strain along the central creeping section of the San Andreas fault, *Geophysical Research Letters*, *35*(14), doi:10.1029/2008GL034437.

Rosen, P., C. Werner, E. Fielding, S. Hensley, S. Buckley and P. Vincent Templeton (1998), Aseismic creep along the San Andreas fault northwest of Parkfield, ca measured by radar interferometry, *Geophysical Research Letters*, *25*(6), doi:10.1029/98GL50495.

Ryder, I., and R. Burgmann (2008), Spatial variations in slip deficit on the central San Andreas fault from InSAR, *Geophysical Journal International*, *175*(3), 837–852, doi:10.1111/j.1365-246X.2008.03938.x.

Sandwell, D., R. Mellors, X. Tong, M. Wei, and P. Wessel (2011), Open radar interferometry software for mapping surface deformation, *Eos Trans. AGU*, *92*(28), 234, doi:10.1029/2011EO280002.

Sandwell, D. T., and L. Sichoix (2000), Topographic phase recovery from stacked ERS interferometry and a low-resolution digital elevation model, *Journal of Geophysical Research-Solid Earth*, *105*(B12), 28,211–28,222.

Savage, J. C., R. W. Simpson, and M. H. Murray (1998), Strain accumulation rates in the San Francisco Bay area, 1972-1989, *Journal of Geophysical Research-Solid Earth*, *103*(B8), 18,039–18,051, doi:10.1029/98JB01574.

Segall, P. (2002), Integrating geologic and geodetic estimates of slip rate on the San Andreas fault system, *International Geology Review*, *44*(1), 62–82, doi:10.2747/0020-6814.44.1.62.

Shen, Z. K., and D. D. Jackson (2005), Southern California tectonic deformation modeling, *Tech. rep.*, Southern California Earthquake Center.

Shen, Z. K., D. D. Jackson, and B. X. Ge (1996), Crustal deformation across and beyond the los angeles basin from geodetic measurements, *Journal of Geophysical Research-Solid Earth*, *101*(B12), 27,957–27,980, doi:10.1029/96JB02544.

Sieh, K. E., and P. L. Williams (1990), Behavior of the southernmost San-Andreas fault during the past 300 years, *Journal of Geophysical Research-Solid Earth and Planets*, *95*(B5), 6629–6645, doi:10.1029/JB095iB05p06629.

Smith, B., and D. Sandwell (2003), Coulomb stress accumulation along the San Andreas fault system, *Journal of Geophysical Research-Solid Earth*, *108*(B6), doi:10.1029/2002JB002136.

Smith, B., and D. Sandwell (2004), A three-dimensional semianalytic viscoelastic model for time-dependent analyses of the earthquake cycle, *Journal of Geophysical Research-Solid Earth*, *109*(B12), doi:10.1029/2004JB003185.

Smith, B. R., and D. T. Sandwell (2006), A model of the earthquake cycle along the San Andreas fault system for the past 1000 years, *Journal of Geophysical Research-Solid Earth*, *111*(B1), B01,405, doi:10.1029/2005JB003703.

Smith-Konter, B., and D. Sandwell (2009), Stress evolution of the San Andreas fault system: Recurrence interval versus locking depth, *Geophysical Research Letters*, *36*(L13304), doi:10.1029/2009GL037235.

Sneed, M., and J. T. Brandt (2007), Detection and measurement of land subsidence using global positioning system surveying and interferometric synthetic aperture radar, Coachella valley, California, 19962005, *Scientific Investigations Report 20075251, 31 p*, U.S. Geological Survey.

Titus, S. J., C. Demets, and B. Tikoff (2005), New slip rate estimates for the creeping segment of the San Andreas fault, California, *Geology*, *33*(3), 205–208, doi:10.1130/G21107.1.

Titus, S. J., C. Demets, and B. Tikoff (2006), Thirty-five-year creep rates for the creeping segment of the San Andreas fault and the effects of the 2004 Parkfield earthquake: Constraints from alignment arrays, continuous global positioning system, and creepmeters, *Bulletin of the Seismological Society of America*, *96*(4), S250–S268, doi:10.1785/0120050811.

Wei, M., D. Sandwell, and Y. Fialko (2009), A silent m(w) 4.7 slip event of October 2006 on the Superstition Hills fault, southern California, *Journal of Geophysical Research-Solid Earth*, *114*, B07,402, doi:10.1029/2008JB006135.

Wei, M., D. Sandwell, and B. Smith-Konter (2010), Optimal combination of InSAR and GPS for measuring interseismic crustal deformation, *Advances in Space Research*, *46*(2), 236–249, doi:10.1016/j.asr.2010.03.013.

Welch, P. D. (1967), The use of Fast Fourier Transform for the estimation of power spectra: A method based on time averaging over short, modified periodograms, *IEEE Transactions on Audio Electroacoustics*, *AU-15*, 7073.

Williams, S., Y. Bock, and P. Fang (1998), Integrated satellite interferometry: Tropospheric noise, GPS estimates and implications for interferometric synthetic aperture radar products, *Journal of Geophysical Research-Solid Earth*, *103*(B11), 27,051–27,067, doi:10.1029/98JB02794.

Wisely, B. A., and D. Schmidt (2010), Deciphering vertical deformation and poroelastic parameters in a tectonically active fault-bound aquifer using InSAR and well level data, san bernardino basin, California, *Geophysical Journal International*, *181*(3), 1185–1200, doi:10.1111/j.1365-246X.2010.04568.x.

Wisely, B. A., D. Schmidt, and R. J. Weldon (2008), Compilation of surface creep on California faults and comparison of WGCEP 2007 deformation model to pacific-north american plate motion, Appendix P in the Uniform California Earthquake Rupture Forecast, version 2 (UCERF 2), *Open File Rep. 2007-1437P*, U.S. Geological Survey.

Zeng, Y., and Z.-K. Shen (2010), A kinematic fault network model of crustal deformation for California and its application to the seismic hazard analysis, *Tech. rep.*, U.S. Geological Survey.

Table 4.1: Data information about ALOS ascending tracks.

Track	Frame	Sum of perpendicular baseline (m)	Number of interferograms	Total time span (days)
224	780	-16	28	22724
224	770	-16	28	22724
224	760	-82	26	20930
223	750	148	16	14674
223	760	148	16	14674
223	770	148	16	14674
223	780	148	16	14674
222	780	-146	23	18676
222	770	-146	23	18676
222	760	-146	23	18676
222	750	-146	23	18676
222	740	-146	23	18676
222	730	-146	23	18676
222	720	9	19	17250
222	710	9	19	17250
221	710	-34	15	12374
221	720	30	8	7314
221	730	-104	14	11362
221	740	-104	14	11362
220	700	32	14	13110
220	710	32	14	13110
220	720	32	14	13110
219	690	13	29	24932
219	700	13	29	24932
218	670	3	23	19090
218	680	3	23	19090
218	690	3	23	19090
217	670	15	13	11914

Table 4.1 – Continued

Track	Frame	Sum of perpendicular baseline (m)	Number of interferograms	Total time span (days)
217	680	15	13	11914
217	690	15	13	11914
216	660	7	24	20838
216	670	7	24	20838
216	680	-60	23	19826
216	690	-60	23	19826
215	650	-65	9	6900
215	660	-6	11	9200
215	670	-6	11	9200
215	680	-6	11	9200
215	690	-104	16	13708
215	700	-104	16	13708
214	650	1	21	18952
214	660	1	21	18952
214	670	1	21	18952
214	680	1	21	18952
214	690	1	21	18952
214	700	1	21	18952
213	650	-228	33	28428
213	660	-228	33	28428
213	670	-228	33	28428
213	680	-228	33	28428
213	690	-228	33	28428
213	700	-228	33	28428
212	650	-1	10	9384
212	660	-1	10	9384
212	670	-1	10	9384
212	680	-1	10	9384

Table 4.1 – Continued

Track	Frame	Sum of perpendicular baseline (m)	Number of interferograms	Total time span (days)
212	690	-151	9	8418
212	700	-151	9	8418

Table 4.2: Creep rate on San Andreas fault system.

San Andreas fault

Latitude (°)	Longitude (°)	Creep rate (mm/yr)	Creep rate uncertainty (mm/yr)	Scale
33.349	-115.724	0.025	0.730	3.163
33.416	-115.799	4.074	0.629	2.643
33.475	-115.877	0.018	1.242	2.698
33.542	-115.951	4.299	0.802	3.075
33.608	-116.026	4.076	0.241	2.695
33.669	-116.102	4.762	0.642	2.902
33.734	-116.178	4.005	1.110	2.822
33.796	-116.255	0.139	0.138	2.666
33.856	-116.336	0.876	0.298	2.526
33.907	-116.422	0.939	0.396	2.360
33.962	-116.508	-0.618	0.410	2.475
34.013	-116.600	-0.598	0.393	1.938
34.042	-116.701	0.624	0.691	1.825
34.063	-116.806	1.089	1.413	1.772
34.078	-116.912	2.020	1.637	1.783
34.101	-117.017	-0.404	1.915	1.821
34.124	-117.121	0.081	0.537	1.845
34.151	-117.223	0.013	0.326	1.933
34.194	-117.319	0.346	0.505	2.175
34.245	-117.411	0.116	0.590	2.230
34.292	-117.503	-1.904	1.885	2.230
34.339	-117.597	-5.121	5.177	2.125
34.378	-117.694	-1.187	1.673	2.038
34.418	-117.791	-2.074	0.611	2.039
34.457	-117.888	-0.901	0.103	2.058
34.498	-117.985	0.056	0.241	2.059

Table 4.2 – Continued

Latitude (°)	Longitude (°)	Creep rate (mm/yr)	Creep rate uncertainty (mm/yr)	Scale
34.539	-118.082	-1.640	0.509	2.059
34.578	-118.181	-0.798	0.304	2.001
34.616	-118.280	-1.602	0.884	1.983
34.652	-118.379	-1.176	1.137	1.984
34.688	-118.480	-5.093	0.956	1.920
34.719	-118.582	-2.272	1.089	1.888
34.749	-118.685	-0.701	0.982	1.888
34.777	-118.789	-1.425	0.675	1.862
34.808	-118.893	-1.755	0.681	1.919
34.824	-118.998	-1.012	0.345	1.730
34.846	-119.105	1.344	0.444	1.775
34.860	-119.211	0.298	0.413	1.868
34.895	-119.312	2.101	0.872	1.999
34.941	-119.405	-0.850	0.765	2.456
34.998	-119.492	-1.631	0.274	2.490
35.057	-119.575	-1.647	0.844	2.770
35.120	-119.655	-0.175	0.565	2.732
35.183	-119.732	0.602	1.220	3.020
35.250	-119.805	0.016	2.546	3.188
35.319	-119.877	0.609	0.857	3.199
35.387	-119.946	0.800	0.885	3.298
35.461	-120.013	-0.593	2.139	3.627
35.531	-120.081	0.338	0.987	3.361
35.600	-120.152	-4.464	0.845	3.052
35.667	-120.224	1.856	0.522	3.355
35.738	-120.294	2.143	0.963	3.357
35.823	-120.355	-5.286	3.173	3.086

Table 4.2 – Continued

Latitude (°)	Longitude (°)	Creep rate (mm/yr)	Creep rate uncertainty (mm/yr)	Scale
35.880	-120.418	14.159	1.672	3.087
35.948	-120.493	26.732	1.783	3.056
36.011	-120.569	30.670	3.531	2.974
36.077	-120.645	26.096	2.101	2.853
36.146	-120.719	28.821	3.810	3.201
36.206	-120.790	19.429	3.770	2.902
36.280	-120.862	24.352	1.965	2.997
36.346	-120.935	18.891	1.152	3.119
36.419	-121.006	20.710	3.553	3.423
36.489	-121.077	22.461	2.733	3.167
36.556	-121.149	23.446	2.106	3.167
36.623	-121.223	11.006	1.550	2.955
36.689	-121.301	7.194	3.438	2.695
36.748	-121.384	15.479	1.590	2.402
36.802	-121.471	10.286	1.826	2.465
36.862	-121.557	4.543	2.084	2.722
36.919	-121.642	2.192	0.524	2.521
36.981	-121.724	0.343	1.174	2.871
37.098	-121.891	-1.910	1.456	2.315
37.160	-121.975	-4.693	2.182	2.799
37.357	-122.206	-2.632	3.124	3.481
37.500	-122.342	-3.671	5.213	3.898
37.877	-122.651	3.793	3.884	3.893
37.951	-122.715	-1.183	2.809	3.896
38.098	-122.846	9.042	5.003	3.696
38.319	-123.041	0.751	2.882	4.285
38.532	-123.250	1.216	2.051	3.292

Table 4.2 – Continued

Latitude (°)	Longitude (°)	Creep rate (mm/yr)	Creep rate uncertainty (mm/yr)	Scale
38.603	-123.322	-4.390	1.316	3.425
38.673	-123.392	-8.293	3.702	3.428
38.743	-123.462	-8.131	2.212	3.431
38.817	-123.530	0.242	1.453	3.866
38.892	-123.596	-1.140	2.282	3.870
38.965	-123.661	-3.385	3.239	3.874

Maacama fault

Latitude (°)	Longitude (°)	Creep rate (mm/yr)	Creep rate uncertainty (mm/yr)	Scale
38.786	-122.922	4.794	1.988	3.053
38.859	-122.993	-1.683	1.067	3.885
38.937	-123.048	8.481	5.452	5.635
39.018	-123.095	2.445	1.547	6.362
39.100	-123.143	2.749	1.301	6.372
39.181	-123.191	3.014	1.027	4.837
39.260	-123.248	-7.650	2.828	4.842
39.339	-123.305	0.846	2.700	4.848
39.420	-123.353	-6.367	6.170	6.319
39.502	-123.401	-8.432	6.456	6.085
39.584	-123.451	-13.417	3.456	6.091
39.665	-123.502	0.200	1.696	5.145
39.744	-123.557	-0.966	1.532	5.152

Bartlett Springs fault

Table 4.2 – Continued

Latitude (°)	Longitude (°)	Creep rate (mm/yr)	Creep rate uncertainty (mm/yr)	Scale
Latitude (°)	Longitude (°)	Creep rate (mm/yr)	Creep rate uncertainty (mm/yr)	Scale
39.038	-122.532	0.517	0.962	3.828
39.107	-122.623	1.776	1.369	3.270
39.170	-122.692	-4.980	2.055	2.443
39.234	-122.768	0.268	0.930	3.150
39.304	-122.833	-0.428	1.171	4.821
39.378	-122.899	-2.381	1.950	4.206
39.454	-122.959	-0.123	2.040	4.030
39.533	-123.020	6.946	4.026	5.388

Concord fault

Latitude (°)	Longitude (°)	Creep rate (mm/yr)	Creep rate uncertainty (mm/yr)	Scale
37.972	-122.036	1.738	1.550	5.099

Rodgers Creek fault

Latitude (°)	Longitude (°)	Creep rate (mm/yr)	Creep rate uncertainty (mm/yr)	Scale
38.170	-122.449	3.851	3.335	3.386
38.242	-122.520	-2.919	1.955	3.453
38.313	-122.594	-3.240	1.706	4.138
38.387	-122.654	2.083	2.017	4.204
38.465	-122.712	3.222	1.252	5.663

Table 4.2 – Continued

Latitude (°)	Longitude (°)	Creep rate (mm/yr)	Creep rate uncertainty (mm/yr)	Scale

Calaveras fault

Latitude (°)	Longitude (°)	Creep rate (mm/yr)	Creep rate uncertainty (mm/yr)	Scale
36.628	-121.189	7.420	2.063	3.053
36.697	-121.266	-0.533	1.552	3.214
36.766	-121.339	0.427	1.598	3.217
36.842	-121.396	5.190	2.051	5.806
36.924	-121.436	8.880	11.067	7.177
37.005	-121.483	7.157	2.284	4.660
37.084	-121.538	25.304	2.426	4.960
37.161	-121.598	9.220	1.458	3.971
37.238	-121.656	-3.419	1.843	4.612
37.315	-121.712	-3.855	4.634	4.617
37.392	-121.768	4.576	1.833	4.675
37.473	-121.819	-4.378	5.807	7.642
37.557	-121.859	14.671	6.272	11.950
37.640	-121.902	-2.585	2.477	5.413
37.721	-121.945	4.922	1.950	6.041

Hayward fault

Latitude (°)	Longitude (°)	Creep rate (mm/yr)	Creep rate uncertainty (mm/yr)	Scale
37.526	-121.949	5.708	1.137	3.943
37.601	-122.012	2.505	0.946	3.425

Table 4.2 – Continued

Latitude (°)	Longitude (°)	Creep rate (mm/yr)	Creep rate uncertainty (mm/yr)	Scale
37.673	-122.083	2.907	0.528	3.439
37.746	-122.143	1.291	0.586	3.557
37.821	-122.210	3.554	0.297	4.144
37.896	-122.270	4.910	0.718	4.243

Garlock fault

Latitude (°)	Longitude (°)	Creep rate (mm/yr)	Creep rate uncertainty (mm/yr)	Scale
34.826	-118.867	0.448	0.532	1.821
34.881	-118.771	0.954	0.543	1.846
34.924	-118.676	0.366	0.572	1.746
34.965	-118.578	-0.619	0.305	1.711
34.995	-118.479	1.717	0.609	1.780
35.044	-118.386	-0.349	0.477	1.917
35.098	-118.296	-1.688	0.419	1.839
35.145	-118.203	0.518	0.261	1.850
35.190	-118.112	-0.025	0.077	1.871
35.246	-118.025	0.073	0.593	1.902
35.309	-117.944	-2.065	2.262	2.047
35.368	-117.860	0.255	1.099	1.829
35.412	-117.766	0.042	0.255	1.774
35.449	-117.665	0.548	0.150	1.705
35.477	-117.561	0.467	0.252	1.683
35.504	-117.456	-0.320	0.055	1.669
35.526	-117.349	0.302	0.187	1.675
35.551	-117.242	1.583	0.219	1.675

Table 4.2 – Continued

Latitude (°)	Longitude (°)	Creep rate (mm/yr)	Creep rate uncertainty (mm/yr)	Scale
35.575	-117.136	0.516	0.190	1.675
35.595	-117.029	-0.702	0.210	1.666
35.604	-116.920	-0.360	0.097	1.665
35.596	-116.810	-0.088	0.091	1.665
35.593	-116.700	-0.869	0.483	1.682
35.591	-116.590	0.068	0.092	1.669

San Jacinto fault

Latitude (°)	Longitude (°)	Creep rate (mm/yr)	Creep rate uncertainty (mm/yr)	Scale
33.033	-116.004	-1.629	1.614	2.898
33.099	-116.056	8.579	0.896	3.938
33.164	-116.143	2.212	1.180	2.675
33.222	-116.217	0.186	0.398	2.442
33.282	-116.296	-2.118	0.745	2.975
33.346	-116.371	-0.184	0.806	2.751
33.407	-116.453	-0.659	0.260	2.648
33.473	-116.516	-1.115	0.675	5.928
33.538	-116.588	0.709	0.569	2.872
33.594	-116.679	0.317	1.258	2.434
33.647	-116.763	1.189	1.053	2.255
33.698	-116.855	0.806	1.565	2.279
33.753	-116.952	2.230	1.063	2.280
33.815	-116.966	-12.948	2.936	2.496
33.877	-117.055	0.362	3.404	2.671
33.938	-117.135	-5.653	1.462	2.733

Table 4.2 – Continued

Latitude (°)	Longitude (°)	Creep rate (mm/yr)	Creep rate uncertainty (mm/yr)	Scale
34.001	-117.215	1.442	0.678	2.946
34.067	-117.287	0.610	0.690	3.272
34.135	-117.358	6.505	2.733	3.274
34.198	-117.424	-0.316	2.192	2.417
34.253	-117.518	-0.875	2.281	2.283
34.311	-117.602	-0.308	1.204	2.594

Superstition Hills fault

Latitude (°)	Longitude (°)	Creep rate (mm/yr)	Creep rate uncertainty (mm/yr)	Scale
32.923	-115.692	1.066	2.930	2.731
32.984	-115.769	2.786	0.400	2.478

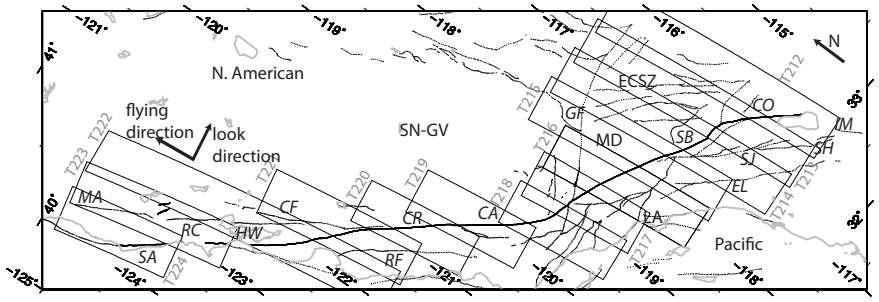

Figure 4.1: A map of the San Andreas fault in California in oblique Mercator projection. The gray boxes with track numbers outline the area covered by 13 ALOS ascending tracks. The radar flying direction and look direction are marked. The black lines shows the geological fault traces. Two-character labels with italicized font correspond to major faults mentioned in this paper: MA-Maacama fault, SA-San Andreas fault, RC-Rodgers Creeks fault, HW-Hayward fault, CF-Calaveras fault, RF-Riconada fault, CR-creeping section, CA-Carrizo segment, GF-Garlock fault, SB-San Bernadino segment, CO-Coachella segment, SJ-San Jacinto fault, EL-Elsinore fault, SH-Superstition Hills fault, IM-Imperial fault. Names with regular font are geographic locations: SN-GV-Sierra Nevada Great Valley, LA-Los Angeles basin, MD-Mojave desert, ECSZ-East California shear zone.

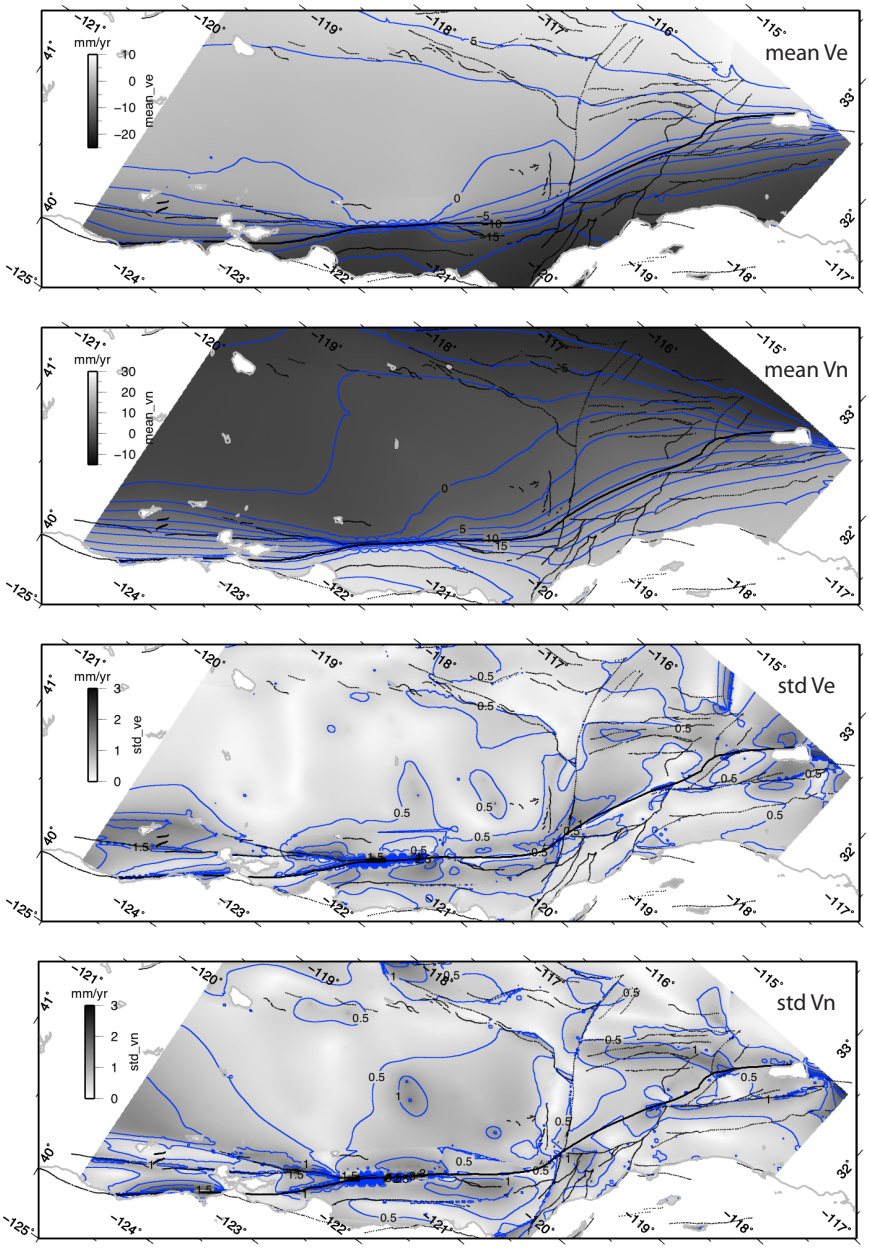

Figure 4.2: Cross comparison of the 4 independent GPS velocity models of the SAF in geographic coordinates. The plots are in Oblique Mercator projection with contour lines in blue. a) Mean of the east component of the velocity models. b) Mean of the north component of the velocity models. c) Standard deviation of the east component of the velocity models. d) Standard deviation of the north component of the velocity models. The contours are at 2.5 mm/yr interval for a) and b) and at 0.5 mm/yr interval for c) and d). The black lines show the geological fault traces.

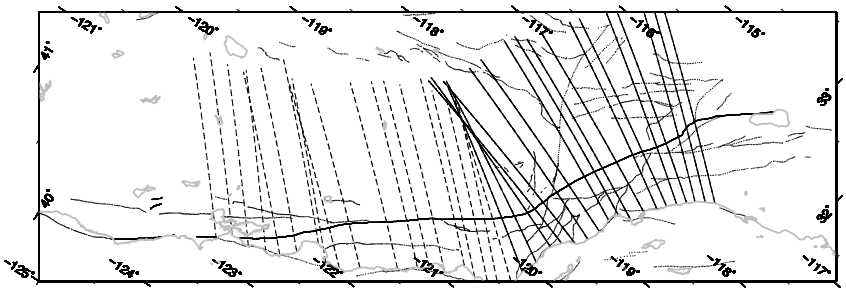

Figure 4.3: The 37 transect lines (solid lines and dashed lines) show the profiles used in the coherence spectrum analysis. The 18 solid transect lines show the profiles used in the power spectrum analysis (Figure 4.16).

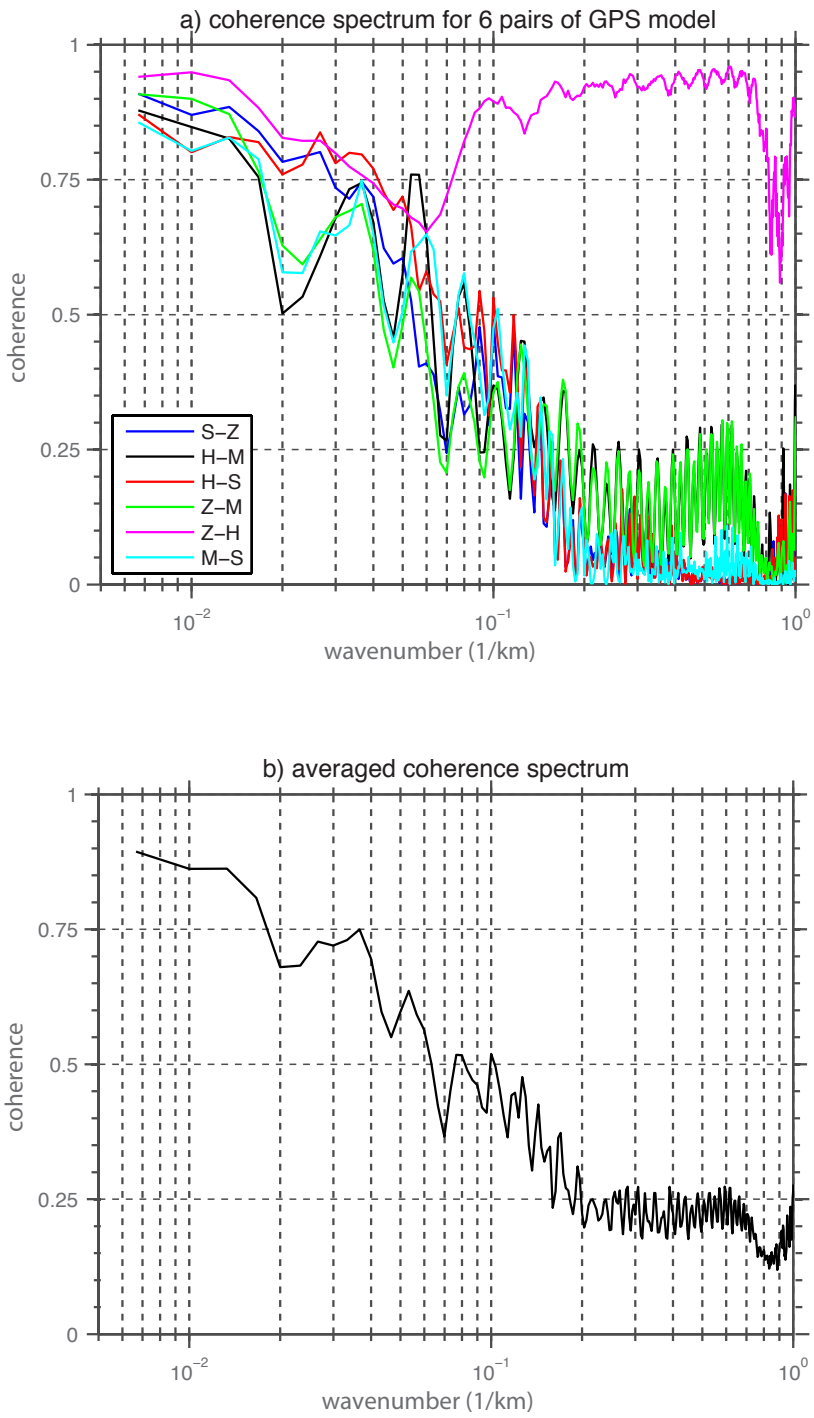

Figure 4.4: a) Coherence as a function of wavenumber for 4 independent GPS-derived models. The coherence spectrum for 6 pairs of the GPS velocity models are compared here: H-model from *Meade and Hager* (2005a); M-model from *McCaffrey* (2005); Z-model from *Zeng and Shen* (2010); S-model from *Smith-Konter and Sandwell* (2009). b) Average of the 6 pairs of coherence spectra from GPS velocity models.

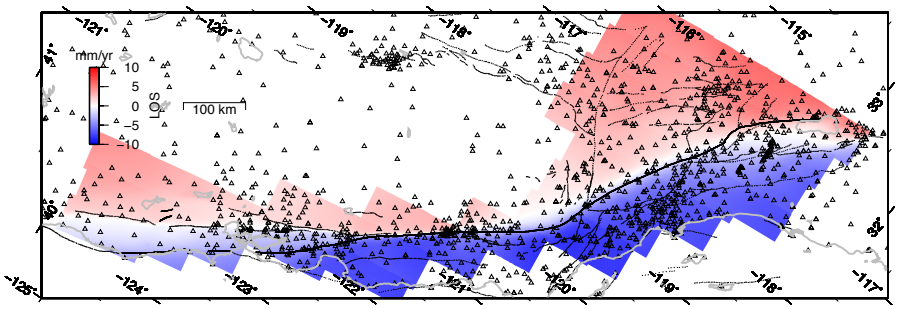

Figure 4.5: Crustal velocity model in line-of-sight (LOS) velocity based on regional the GPS velocity field (*Smith-Konter and Sandwell*, 2009) in oblique Mercator projection. The colors represent the LOS velocity field along 13 ALOS ascending tracks represented by radar swaths (Figure 4.1). The radar flying direction and look direction are marked in Figure 4.1. Positive velocities (reds) show the ground moving relatively away from the satellite. The small triangles are the GPS stations used to constrain the velocity model. The black lines shows the geological fault traces.

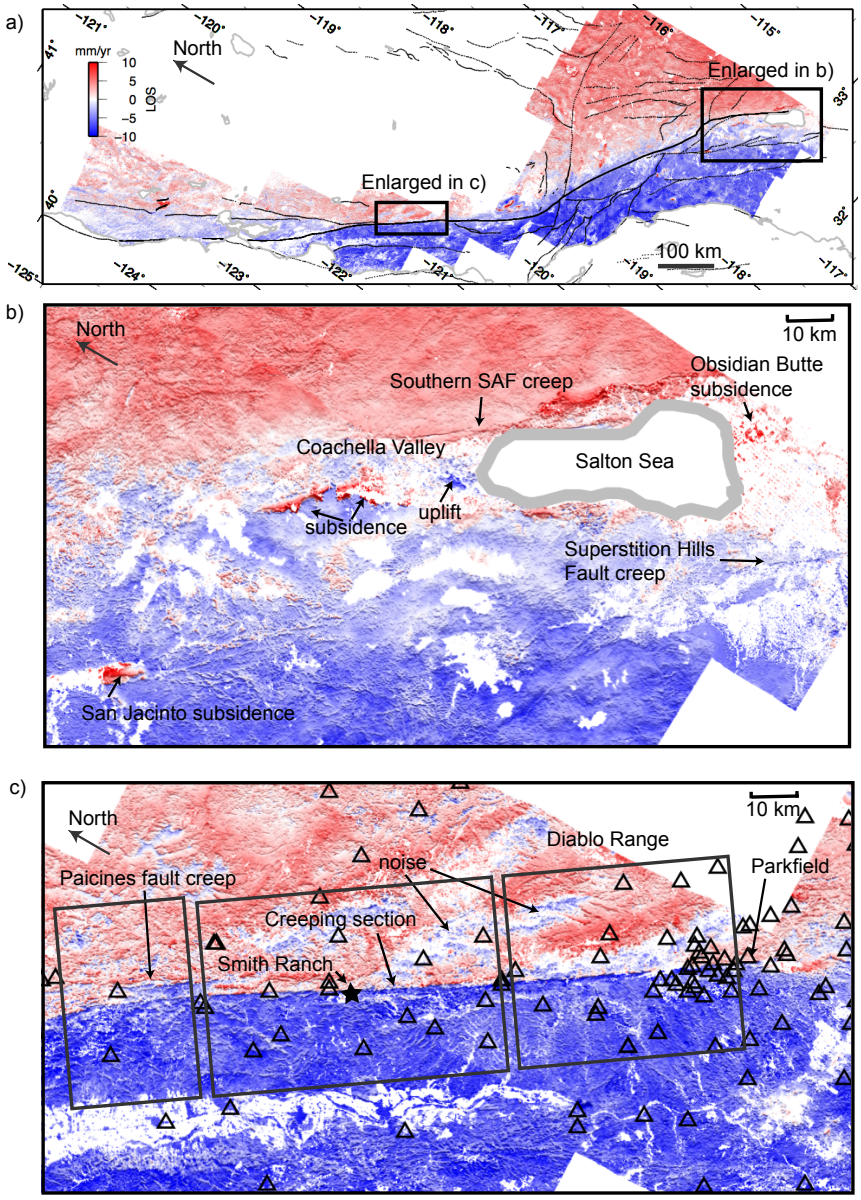

Figure 4.6: a) Interseismic deformation of the SAF derived from integrating the GPS observations with ALOS radar interferograms (2006.5-2010). The radar flying direction and look direction are marked in Figure 4.1. Positive velocities (reds) show the ground moving away from the satellite. The shading highlights the gradient in the velocity field. The areas with low coherence and large standard deviation (> 6 mm/yr) are masked. GPS sites are shown as triangles. b) Southern part of the SAFS shows the broad transition in velocity across the San Andreas and San Jacinto. c) Central section of the SAFS shows the sharp velocity gradient across the creeping section. The black star marks the location of the Smith Ranch. The black boxes mark the locations of the velocity profiles shown in Figure 4.13.

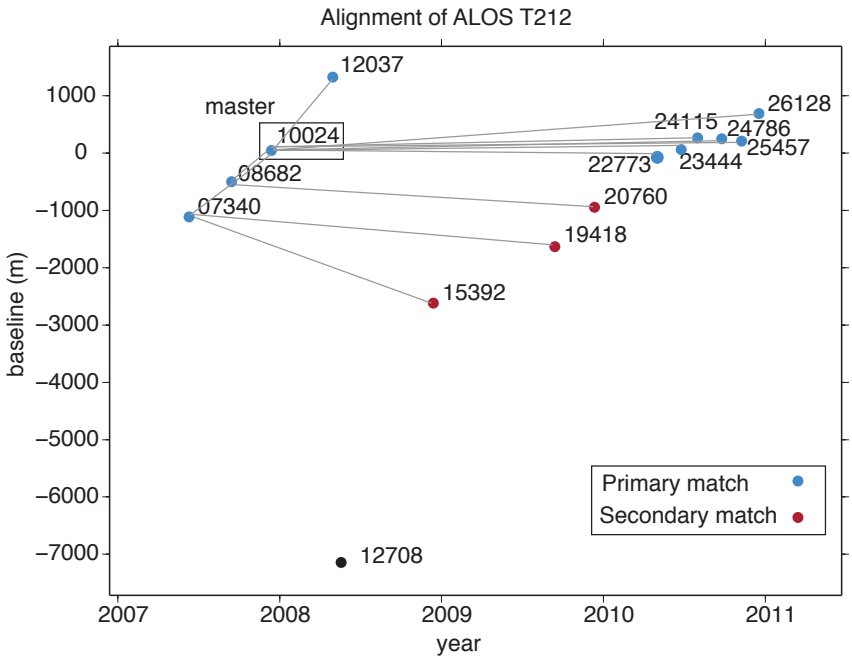

Figure 4.7: Example perpendicular baseline vs. time plot showing the "leap-frog" alignment approach taken prior to forming the interferograms. The track number is 212 and the orbital indices are shown as 5-digits number in the plot. Image 10024 is boxed, representing the super master image. Primary matches (those that plot close to the super master in the baseline-time domain) are represented by blue dots. Secondary matches are represented by red dots.

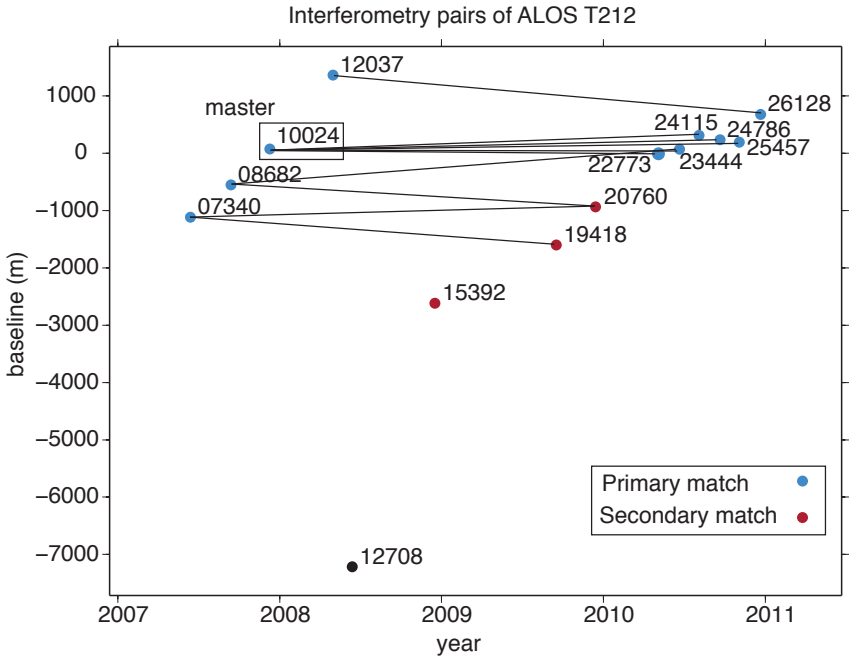

Figure 4.8: Example perpendicular baseline vs. time plot showing interferometric pairs used in the stacking. The track number is 212 and the orbital indices are shown as 5-digit numbers in the plot.

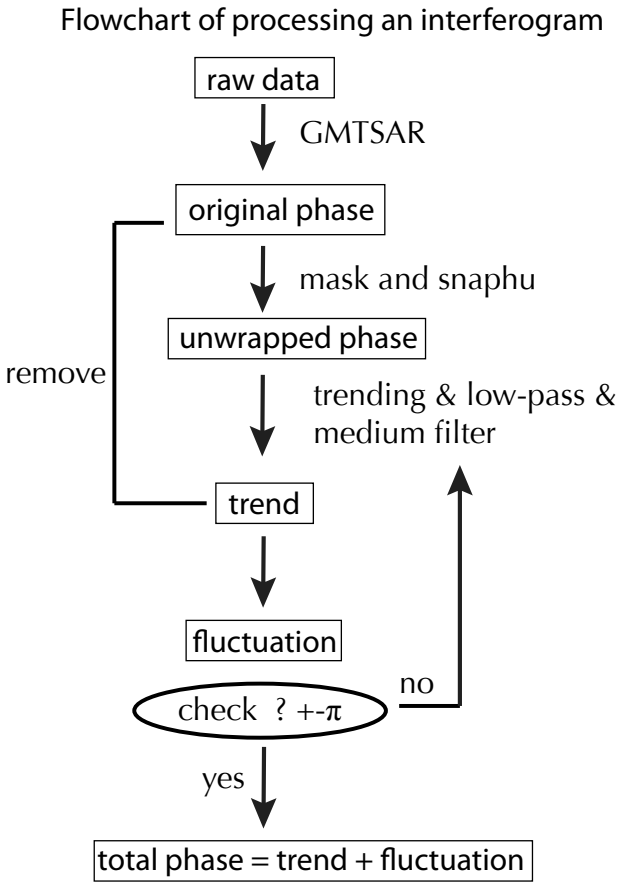

Figure 4.9: Flowchart for iterative phase unwapping of a single interferogram.

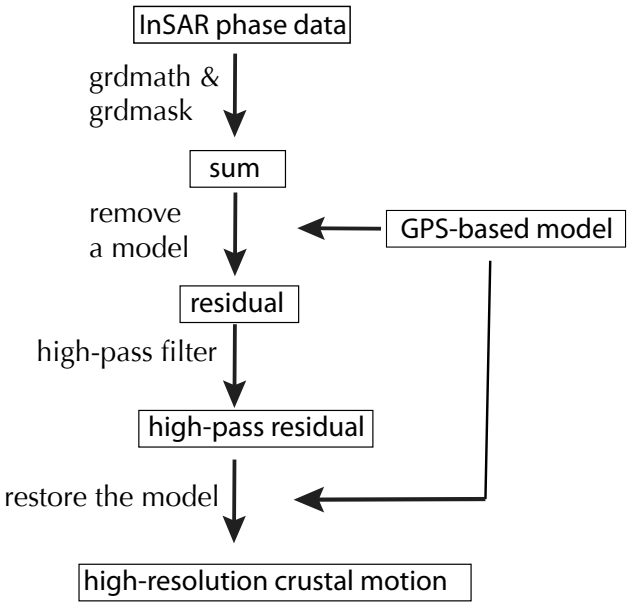

Figure 4.10: Flowchart of combining InSAR stacks with GPS observations (*Wei et al.*, 2010)

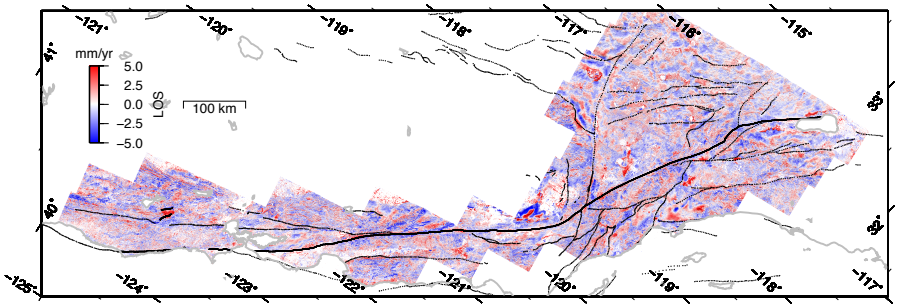

Figure 4.11: High-pass filtered residual velocity (2006.5-2010) along ALOS ascending tracks. This residual velocity reveals the discrepancy between the InSAR observations and GPS model prediction at short wavelength. For example, we found that the residual are significant along the creeping sections, the Garlock fault, and the LA basin. A fine-tuned interseismic velocity model based on both InSAR and GPS observations should have smaller high-pass filtered residual velocity. Note that the residual could also be caused by non-tectonic effects, such as ground water.

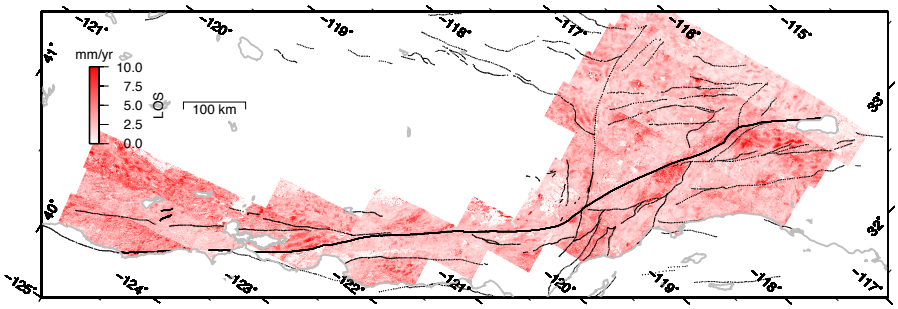

Figure 4.12: Standard deviation of the average LOS velocity (2006.5-2010) along ALOS ascending tracks. Larger uncertainties are found north of the San Francisco Bay area in northern California, near the San Bernadino Mountain. The uncertainties could be due to unwrapping errors, atmospheric noise or deviations from steady-state ground motion. The standard deviation provides a measure of uncertainty of the high-resolution LOS velocity data and can be used in modeling the interseismic deformation.

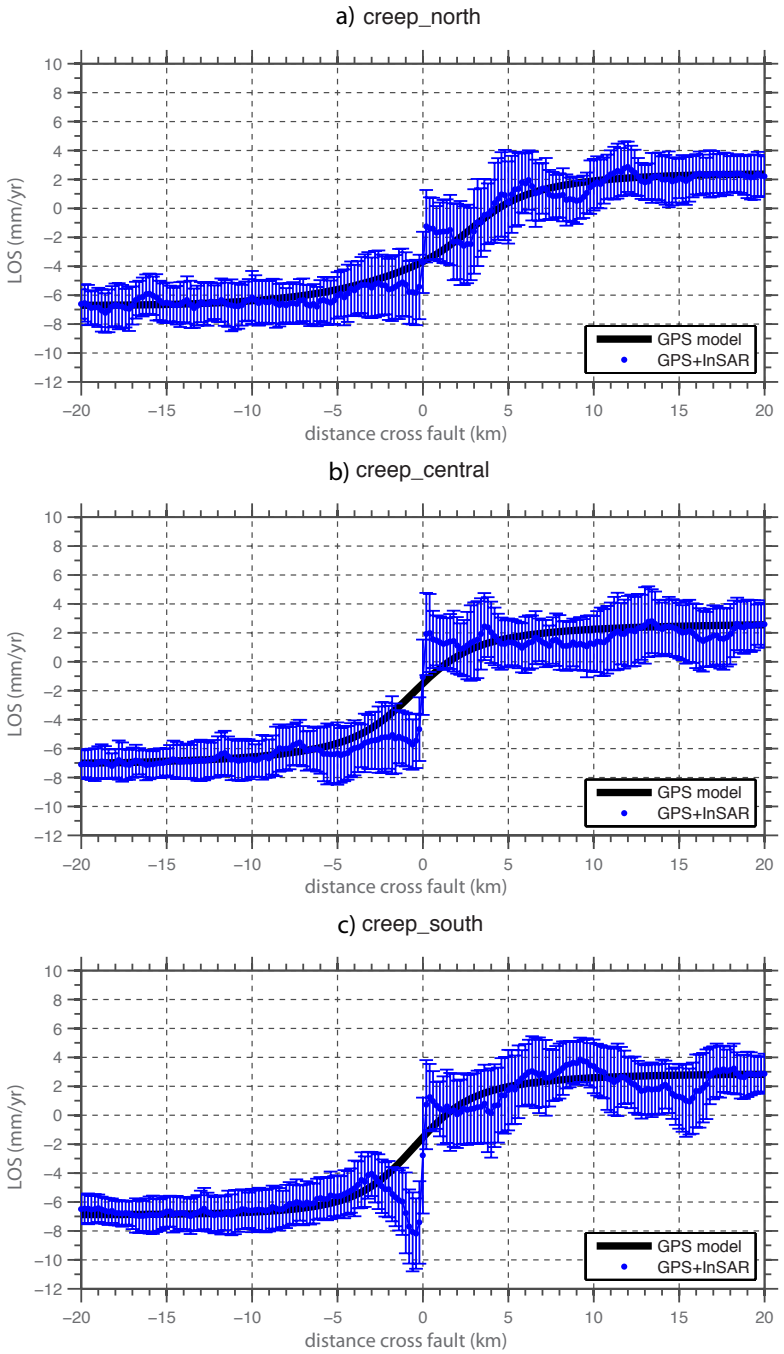

Figure 4.13: Averaged LOS velocity profiles perpendicular to the fault over Central California along the creeping section of the SAF (Figure 4.6c). The blue dots with 1-standard deviation errors bars indicate the total LOS velocity and the black lines are the GPS model. a) Profile taken along the northern segment of the creeping section. b) Profile taken along the central segment of the creeping section. c) Profile taken along the southern segment of the creeping section.

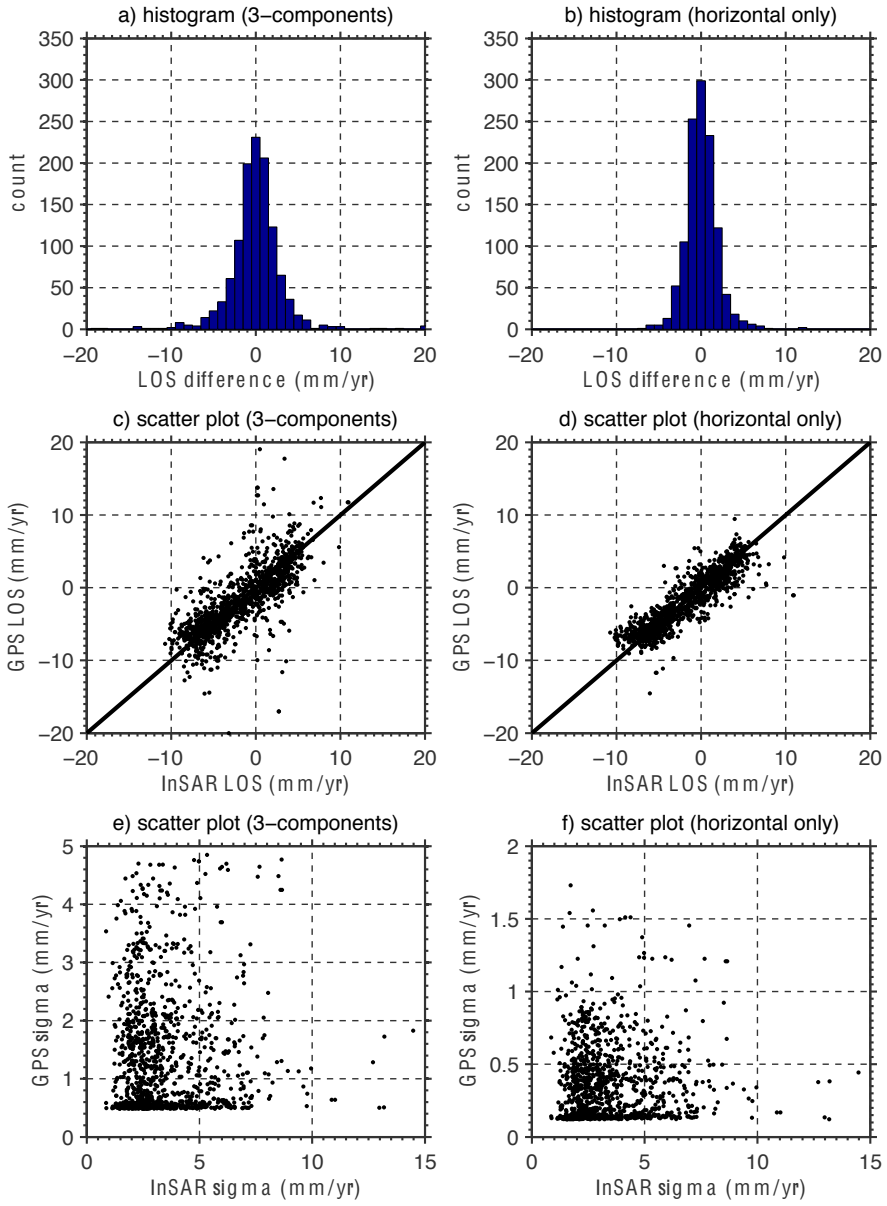

Figure 4.14: Comparison between the InSAR LOS velocity and the GPS observations projected into LOS coordinates. a) and b): histogram of $V_{diff}(x) = V_{GPS}(x) - V_{InSAR}(x)$ for 1068 GPS sites. c) and d): $V_{InSAR}(x)$ against $V_{GPS}(x)$. e) and f): comparison of the standard deviations $\sigma_{GPS}(x)$ and $\sigma_{InSAR}(x)$. Both the vertical and the horizontal components of the GPS velocity are used in the projection for a), c), and e). Only the horizontal components of the GPS velocity are used in the projection for b), d), and f).

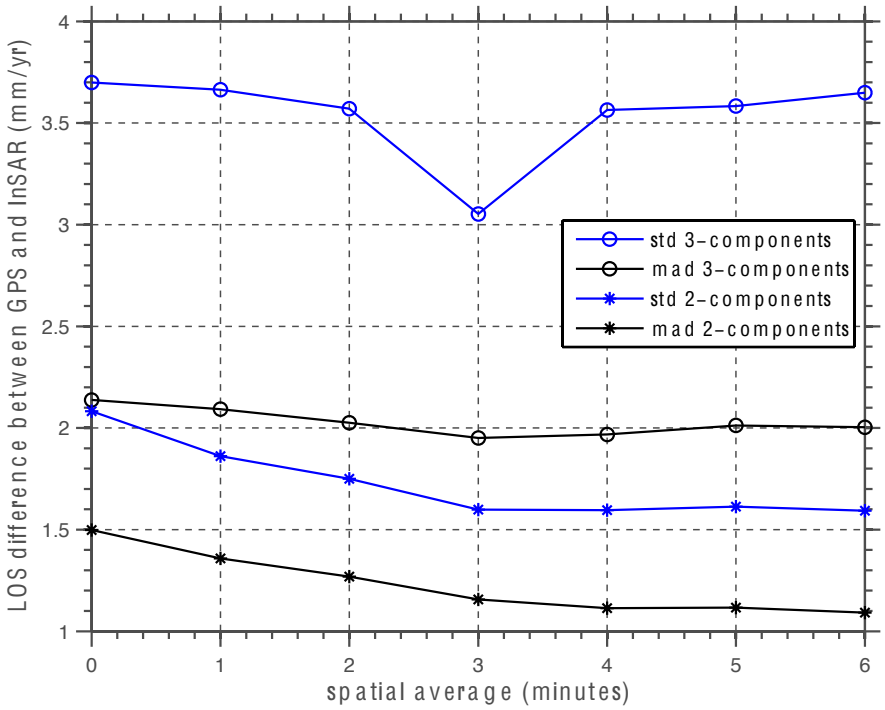

Figure 4.15: The standard deviations of $V_{diff}(x) = V_{GPS}(x) - V_{InSAR}(x)$ as a function of spatial averaging. "std" means the standard deviations and "mad" means the median absolute deviations. The horizontal axis is in arcminutes. One arcminute is approximately 2 km in distance. In the legend, 3-components represents both horizontal and vertical displacements while 2-components represents horizontal displacements only.

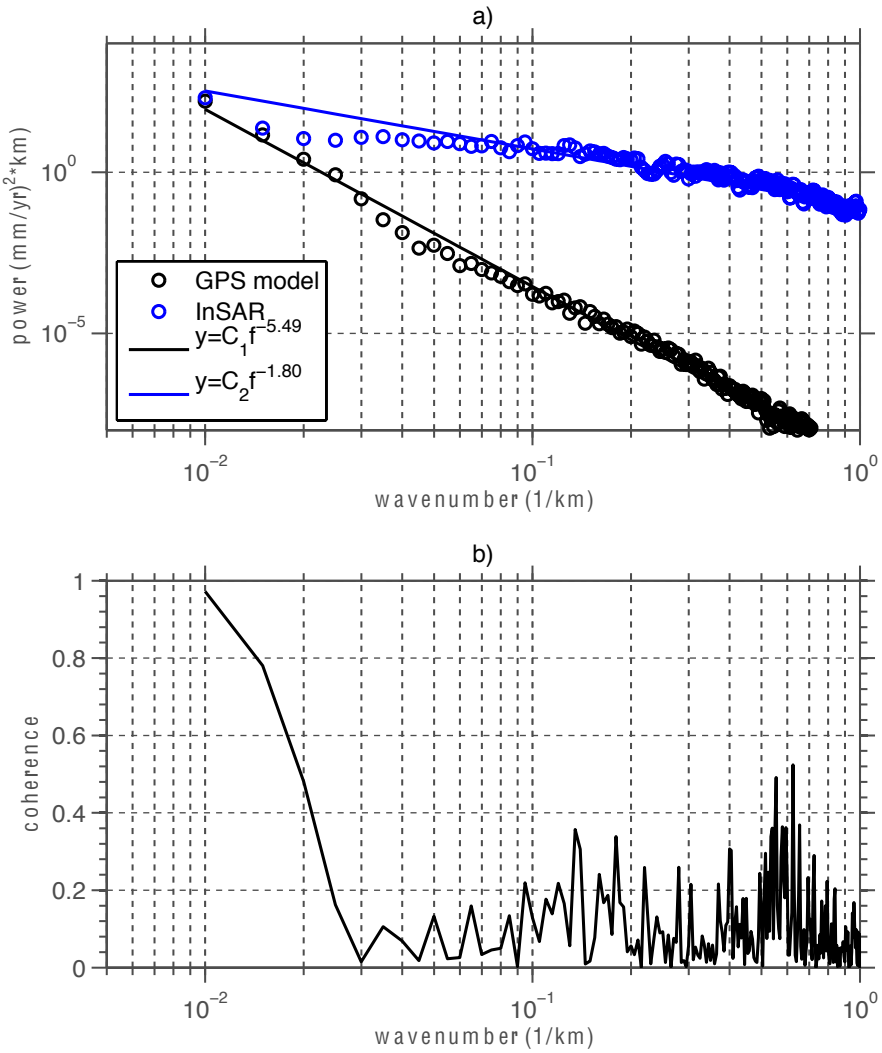

Figure 4.16: a) Power spectrum of the GPS model and the InSAR LOS velocity data with their power law fitting curves. b) Coherence spectrum between GPS model and the InSAR LOS velocity data.

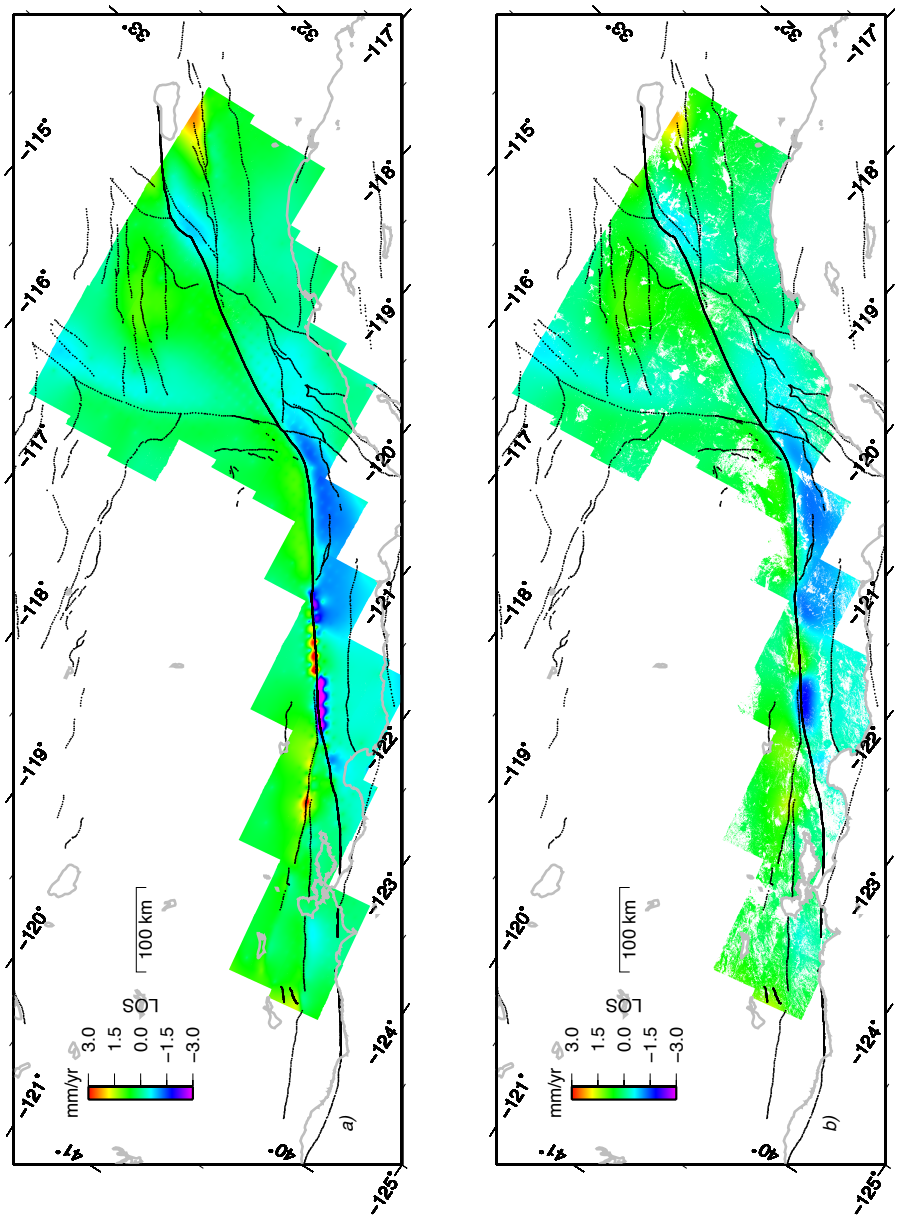

Figure 4.17: a) The difference between the S-model and Z-model. The color represents the difference in LOS velocity. b) The difference between the recovered high-resolution LOS velocity data using S-model and Z-model. The coverage of the LOS velocity map is smaller due to slightly smaller coverage of the Z-model.

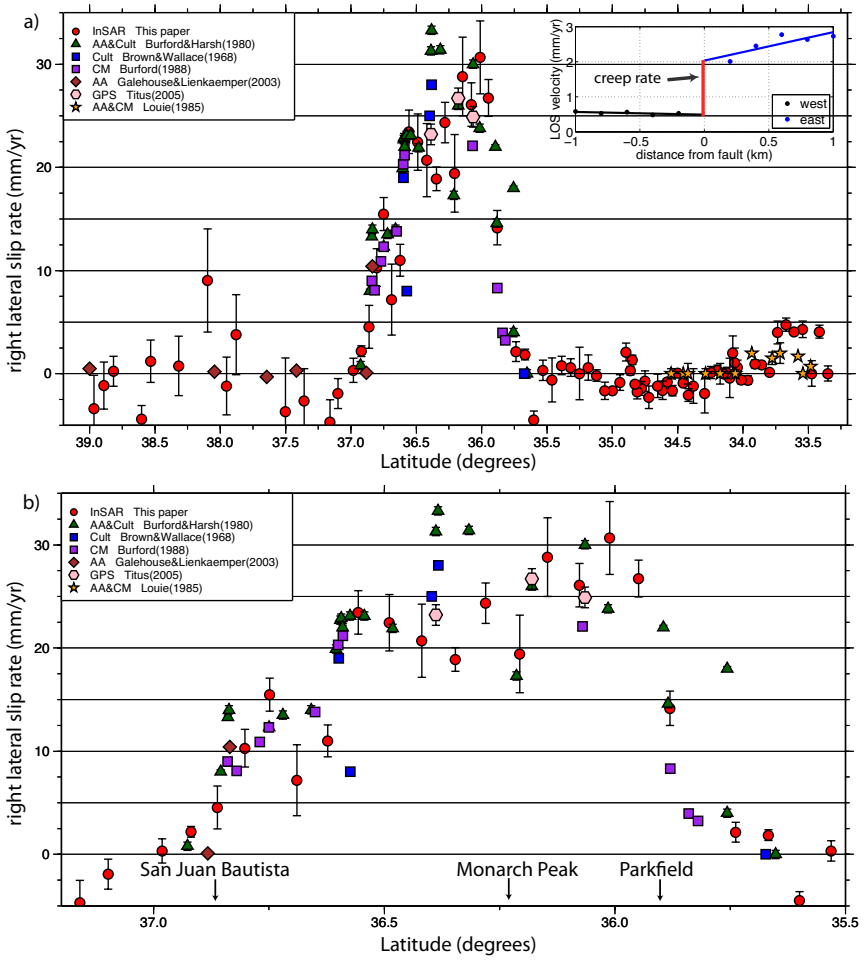

Figure 4.18: Creep rate comparison with an independent data set compiled by UCERF2. The red circles are the creep rate from InSAR in the period from 2006.5 to 2010 (this study). The error bars show the 1σ (σ is the standard deviation) uncertainty. The triangles and other symbols are independent creep measurements compiled by UCERF2. AA means alignment array; CM means creep meters; Cult means cultural offset. a) Creep rate along the entire SAF from north to south. The inset on the upper right corner shows the linear regression method to determine the surface creep rate across fault. b) A zoomed-in view at the creeping section in central California. See text for details.

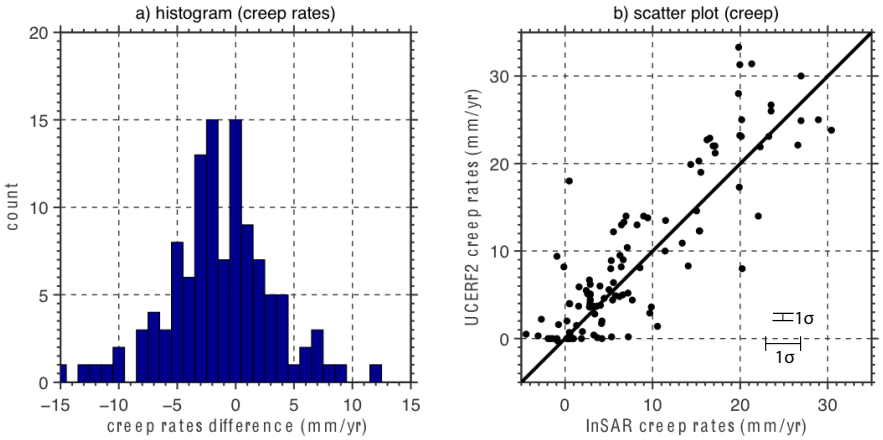

Figure 4.19: Creep rates estimates from InSAR and from ground-based instruments compiled by UCERF2 (alignment arrays, GPS, creepmeters, cultural offsets). a) Histogram of the creep rates difference between InSAR and UCERF2 creep rate datasets. b) Scatter plot of the creep rate data from InSAR versus UCERF2.

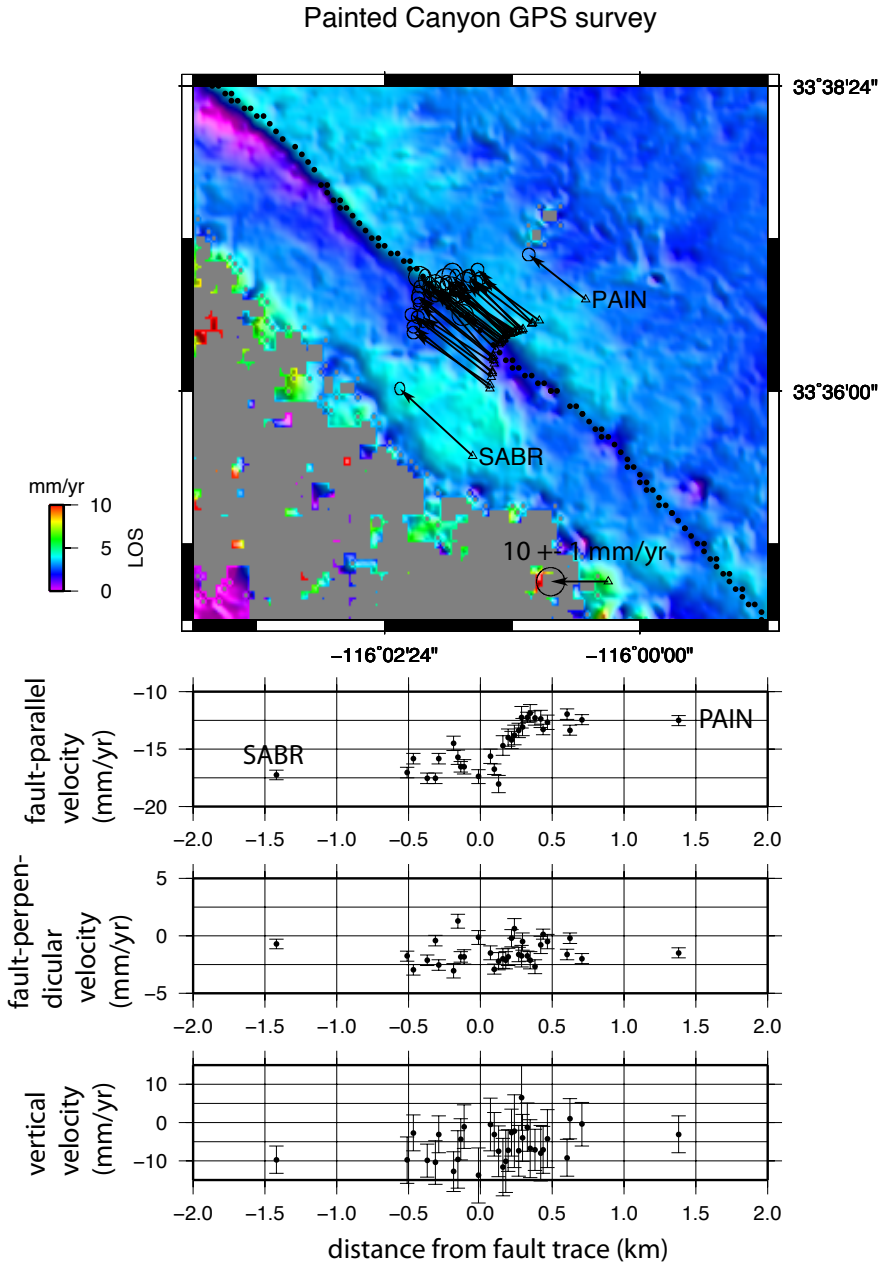

Figure 4.20: Campaign GPS survey at Painted Canyon at 2007 and 2010. The vectors in the top subplot show the horizontal GPS velocity, with 95% confidence ellipses. The black dots mark the SAF. The background is the recovered high-resolution LOS velocity map. Two base stations PAIN and SABR are labeled. The 3 bottom subplots show the fault parallel velocity, fault perpendicular velocity and vertical velocity, respectively, across the fault trace.

Chapter 5

Earthquake cycle model of the San Andreas Fault constrained by GPS and ALOS radar interferometry

Most slip-rate inversions for the San Andreas Fault System (SAFS) use elastic models assuming constant velocities. The viscoelastic relaxation effect is usually neglected. In this study we inverted for the slip rate on 51 major faults of the SAFS using Green's functions for a 3-dimensional earthquake cycle model that includes kinematically prescribed slip events for the past earthquakes since 1000 AD. 1989 present-day velocity measurements from GPS provide accurate constraints on the geodetic slip rate. High-resolution interseismic velocity data from ALOS PALSAR is incorporated to resolve near fault deformation. A thin plate (30 km) and a thick plate (60 km) both having half-space viscosity of $10^{19} Pa{\cdot}s$ were tested in the inversion. The best-fitting slip rates from these plate models were compared against the elastic half-space model. We found that the 60 km thick plate model provides the best fit to the geodetic data and geological constraints.

[0]This chapter is going to be submitted to *Journal of Geophysical Research*. At this point we have preliminary results and we plan to refine them over the next few weeks. The suggestion from the committee is welcome.

Moreover the half-space model provides an adequate fit. A more detailed model of the creeping section in Central California shows evidence for significant asperities at depths of 5-10 km. These asperities at the creeping section has implications to the earthquake hazard analysis in California.

5.1 Introduction

Geodesy has become an increasingly important tool for recovering crustal strain rates and moment accumulation rates in tectonically active regions. In California the high-accuracy GPS velocity from continuous and campaign networks, such as the Plate Boundary Observatory (PBO) and Southern California Integrated GPS Network (SCIGN) are used to estimate the fault slip rates along the San Andreas Fault System (SAFS) (*Mccaffrey*, 2005; *Meade and Hager*, 2005; *Smith-Konter and Sandwell*, 2009; *Zeng and Shen*, 2010) especially for those faults where geological estimation is lacking or inaccurate. The fault slip rates on these major faults are an important component in the earthquake hazard analysis.

The common approach to invert for the fault slip rates is through elastic block models. In this approach the observed velocity field is attributed to rigid block rotation, which lead to kinematically consistent fault slip rates, and fault locking in the interseismic period. This approach has been successfully applied to tectonically complex regions such as Tibet, Japan, Italy, Sumatra and Western Unites States. In California detailed block models are constructed based on geological and geodetic observations.

There are emerging problems with this block modeling approach: first, the block boundaries are not well determined in many regions, leading to uncertainties in the slip rates estimates. It is debated whether block representation of the surface velocity is valid in some regions such as Tibet and West Turkey (*Aktug et al.*, 2009; *Thatcher*, 2007). The block bounding faults presume strain concentration near the block boundaries and the off-fault deformation is usually difficult to quantify. Secondly the interseismic locking doesnt account for the viscoelastic effect in the lower crust and upper mantle (*Nur and Mavko*, 1974). It has been

observed that following large earthquakes the steady state motion is perturbed by the viscoelastic response in the lower crust and upper mantle. The surface strain rate will increase immediately following an event and decreases slowly over years or decades. The significance of this viscoelastic effect depends on the plate thickness and underlying viscosity structure. There have been efforts to explore the viscoelastic effect using geodetic data (*Hearn et al.*, 2002; *Takeuchi and Fialko*, 2012; *Pollitz*, 2001; *Freed et al.*, 2007). Thirdly the resolution of the current block models is limited over the creeping sections. This is partly due to oversimplified model parameterization, and partly due to lack of high-resolution geodetic data. The newly derived high resolution interseismic velocity data from L-band InSAR mission (ALOS) can provide tight constraints on the shallow portion (i.e. < 10 km) of the faults, such as the asperities of the creeping section of the San Andreas Fault (SAF) (*Tong et al.*, 2013).

This study is to improve the earthquake cycle model from previous work (*Smith-Konter and Sandwell*, 2009) by refining the parameters of their model using an inverse method. In their model (*Smith and Sandwell*, 2006) the fault locking depth is obtained by inverting GPS velocity data with a presumed fault slip rate adopted from a compilation of quaternary slip rates. (*Smith-Konter and Sandwell*, 2009) found that the stress accumulation rate of major faults is inversely proportional to the earthquake recurrence interval. Recently *Smith-Konter et al.* (2011) made quantitative comparison between the geodetic derived locking depth with seismogenic depth in southern California and found a general agreement between them. We are interested in addressing the following questions: What is the effect of earthquake cycle on the fault slip rates in the SAFS? How are the slip rates from the viscoelastic models different from the elastic models? What is the moment accumulation rate along major faults? Is the creeping section partially locked?

In this paper we incorporate GPS velocity and InSAR line-of-sight (LOS) velocity data and geological data including quaternary fault slip rates, historical and prehistorical earthquakes and earthquake recurrence interval to construct a high resolution deformation model of the SAFS, starting from Cerro Prieto fault to the south to the Maacama fault to the north. We simultaneously solve for the

fault slip rates of 51 major faults and detailed creep distribution at the creeping faults in an over-determined least squares problem for a 3-dimensional viscoelastic earthquake cycle model. This model can be used to estimate moment accumulation rate and stress accumulation rate along the SAFS.

5.2 Data

5.2.1 GPS velocity

The GPS data used in this study include totally 1989 horizontal velocity vectors covering major faults along the SAFS. 1871 velocity vectors were selected from the GPS velocity solutions (T. Herring, personal communications) of the entire Western United States. These measurements include the UNAVCO Plate Boundary Observatory (PBO) GPS sites and continuous and campaign GPS sites from Crust Motion Model (CMM4) (*Shen et al.*, 2011). In addition we added 8 campaign sites in Central California (*Rolandone et al.*, 2008) which cover the central portion of the creeping section. A new velocity field from 110 campaign sites near Salton Trough in Southern California (*Crowell et al.*, 2013) were included to provide a dense coverage of the near-fault deformation near the Imperial fault. Both of the campaign GPS results were rotated into the same reference frame as the continuous GPS sites to yield a consistent velocity field. Figure 5.1 shows the location of the GPS sites in an oblique Mercator projection with projection pole (lon $-74.4°$, lat $50.1°$). This pole is determined based on the pole of rotation analysis from *Wdowinski et al.* (2007). Only the horizontal components of the GPS velocity vectors were used in this study.

5.2.2 L-band ALOS InSAR LOS velocity

InSAR can retrieve a high-resolution map of the velocity field so that it is ideal tool to resolve accurately the gradient of the velocity field. This InSAR data is obtained through L-band radar, which can maintain good temporal coherence in vegetated areas compared to C-band radar. One of the limitations of the

InSAR is that it only measures the velocity in the line-of-sight direction which is a combination of the vertical and horizontal velocity. The InSAR data in this study is acquired along the ascending orbits and the LOS velocity is approximately $V = -0.55V_e - 0.1V_n + 0.78V_u$ (assume 351° flight direction in azimuth with 37° look angle) where Ve Vn and Vu are the east, north, up velocity. High-resolution modeling would be greatly improved if a second LOS direction along descending orbits (the second LOS velocity would be approximately $V = 0.55V_e + 0.1V_n + 0.78V_u$) were available to distinguish the horizontal motion from the vertical motion. The ALOS-2 mission that is going to launch by the end of 2013 will equip a radar with two look directions so its possible that the future mission will resolve this ambiguity issue.

Our InSAR LOS velocity data is derived from integration of the radar interferogram stacking and GPS velocity (*Tong et al.*, 2013). In that study the long wavelength of the InSAR LOS velocity field is constrained by the GPS therefore the only new information added by InSAR is on the short wavelength (< 40 km) on the deformation spectrum. The main contribution of the InSAR data is to reveal details of the fault creep distribution such as the creeping section of the SAF and the faults in Northern California.

We first made a mask for the InSAR LOS velocity data to isolate non-tectonic effects. We identified 47 anomalous areas that exhibit anthropogenic-related ground motion, most likely caused by ground water exaction, along the major faults in California. The data within these anomalous areas were not used. The remaining LOS velocity data were down sampled to 53,791 points based on the second invariant of the strain rates. This subsampled data provide full resolution in high velocity gradient area near the faults and lower resolution in areas of low strain rate away from the faults. The 3-component look vectors and the standard deviations for each LOS velocity data point were sampled accordingly. The sampled LOS velocity is shown in Figure 5.1.

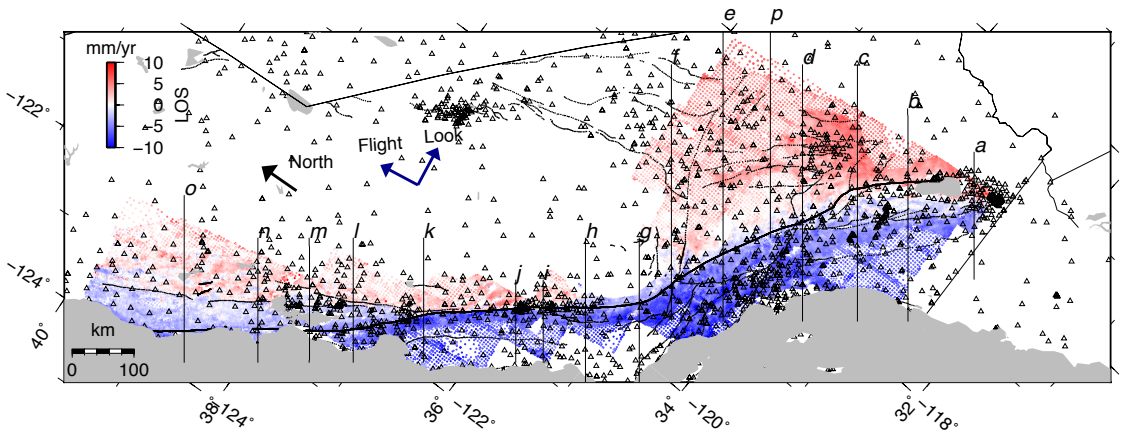

Figure 5.1: GPS (triangles) and InSAR LOS velocity data (colored grid) used in the slip-rate inversion (Oblique Mercator projection). InSAR data are derived from 1100 ALOS radar interferograms (2006.5-2010). The radar flight direction and look direction are provided. Positive velocities (red) represent ground motion away from the satellite. The geological fault traces are shown as black lines. The thin black lines with alphabet letters are the profiles in Figure 5.7.

5.2.3 Geological data

The fault slip rates of closely-spaced parallel faults such as the Elsinore, San Jacinto, San Andreas fault in Southern California and the San Andreas, Maacama, Green Valley fault in Northern California are difficult to resolve using geodesy alone. To make a kinematically consistent model we introduced three types of geological constraints. This approach is similar to what used in the block models on the SAFS (*Mccaffrey*, 2005; *Meade and Hager*, 2005).

First, we used quaternary fault slip rates to further constrain our model. The underlying assumption is that the present-day deformation can represent the tectonic process over geological time scale. The quaternary fault slip rates used in this study are from the Working Group on California Earthquake Probabilities (WGCEP) (*Field et al.*, 2009). We assigned each estimate with an uncertainty of 10 mm/yr to account for the variability in quaternary fault slip rate derived by different investigators. Second, we introduced the triple junction closure criterion such that when two fault strands join into a single strand the sum of the two

strand rates should match the single strand rate. This condition has analog to the classic triple junction closure criteria at the plate intersections, except that all the faults in this case are approximately parallel to each other. Third, we required that the sum of slip rates on parallel strands should approximately match the overall relative slip rate along the plate boundary (e.g., $\sim$ 45 mm/yr).

5.3 3-Dimensional earthquake cycle model

We used a fully 3-dimensional, time-dependent earthquake cycle model (*Smith-Konter and Sandwell*, 2009) to calculate the surface velocity. The model comprises an elastic plate overlying a viscoelastic half-space. The earthquake cycle effect produces time-dependent deformation by visco-elastic relaxation of the asthenosphere. This model assumes a linear (Newtonian) rheology of the viscous behavior corresponding to diffusion creep in the laboratory derived flow law. In this model the SAFS system is divided into 51 inter-connected fault segments each having uniform slip rate, locking depth, and earthquake history. Each segment is further sub-divided into smaller patches (1-5 km) to follow the curvature of the fault. The fault geometry and segmentation was adopted from previous study (*Smith-Konter and Sandwell*, 2009). Each fault segment slips freely at a steady velocity from its locking depth to the base of the elastic plate. The coseismic rupture is assumed to extend from the surface to the locking depth prescribed for each fault segment. The locking depth of each fault is estimated by GPS observations and the seismicity (*Smith-Konter et al.*, 2011). The model is set up in Cartesian coordinates thus we projected the GPS and InSAR data and the fault model into Pole of Deformation (PoD) coordinates with projection pole (lon: $-74.4°$, lat: $50.1°$) (*Wdowinski et al.*, 2007). The efficiency of the model computation is greatly improved by solving the equations in the Fourier Transform domain. (See *Smith and Sandwell* (2006) for a detailed description of this model.)

There are well-known trade-offs between the plate thickness and effective viscosity of the underlying asthenosphere (*Watts*, 2010). We used a constant effective viscosity of $10^{19} Pa \cdot s$ (20 year Maxwell time) and varied elastic plate thickness

to simulate three scenarios: an elastic half-space model with a very thick plate (9999 km, effectively infinite compared to the horizontal dimension of the model), a thick-plate model (60 km) and a thin-plate model (30 km). The half-space model has fault-localized slip from the locking depth to infinite depth. In contrast, the plate models have slip from the locking depth to the base of the elastic layer. The thick-plate model has a deep fault zone that may be controlled by localized ductile shear of the lower crust and upper mantle or by a brittle creep fault zone. The thin plate model has a deep fault zone that is a smaller fraction of the total plate thickness. The deformation beneath the elastic plate is more or less distributed viscously through the bulk of the lower crust and upper mantle. Another important difference between the plate model and half-space model is that the elastic strain in the interior of the plate is much greater than the elastic strain in the interior of the half-space blocks.

Our model used realistic earthquake sequences based on a recent compilation of all the historical and prehistorical earthquakes dated from 1000 AD to present (*Smith and Sandwell*, 2006; *Field et al.*, 2009). Prior to known earthquake sequences we prescribed 10 additional elementary earthquake cycles according to the estimated earthquake recurrence interval (*Field et al.*, 2009) to spin up the earthquake cycle. Note that the magnitude of the slip along each segment for each event is usually not known so we assume that the slip for each earthquake is equal to the slip rate on the fault times the time since the last earthquake. The shallow slip events "catch up" with the deep slip over an earthquake cycle to satisfy block motion on the fault.

Before performing inversions we validated our model with 2-dimensional analytic solutions from Savage *Savage and Prescott* (1978). We prescribed a long vertical strike-slip fault that extends through our model domain. The fault is slipping at plate rate V_0 from the locking depth (15 km) to the bottom of the elastic plate. We prescribed 10 earthquakes with recurrence interval of 100 years. The Maxwell time is set to 20 years ($\tau_0 = 5$ to be comparable to the formula from *Savage and Prescott* (1978)). We considered two scenarios: a thick plate (60km) and a thin plate (30km) in this comparison. The cross-sections of the fault parallel

velocity at surface were compared against those from the analytic solutions as shown in Figure 5.2. It is clear that the numerical model reproduces the analytical solution at different times within an earthquake cycle.

The deep-dislocation earthquake cycle model can't accurately resolve the surface velocity due to fault creep in the upper plate. We augmented this model using shallow dislocations in a layered elastic half-space (*Wang et al.*, 2003). It is generally thought that the fault creep is confined within the shallowest sedimentary layer of the crust (1 or 2 km depth). However it has been found that fault creep can occur in the brittle upper crust in several major faults in Central and Northern California. Asperities along these creeping faults are suggested by recent dense geodetic observations (*Funning et al.*, 2007; *Rolandone et al.*, 2008; *Ryder and Burgmann*, 2008). These asperities could reveal heterogeneous interseismic coupling along the SAF, which has important implications to seismic hazard.

The creep rates could be biased if we apply a homogeneous elastic model to the deformation that has occurred over a sedimentary layer with low rigidity (*Wang et al.*, 2003). A realistic layered elastic structure was derived from a recent seismic tomography study of California (*Lin et al.*, 2010). The P-wave velocity increases from 3.5 km/s at the surface to 8 km/s below 45 km depth and the S-wave velocity increases from 2 km/s at the surface to 4.4 km/s below 45 km. From the seismic wave velocity structure we found that the rigidity (i.e. shear modulus) increase monotonically from 8 GPa near surface to 58 GPa below the Moho depth. In this initial combined model, we only included the shallow dislocation patches on the creeping section in Central California. The creeping fault extending from the surface to 12 km depth was divided into 15 rectangular. The size of the creeping patches increases with depth to accommodate lower resolution at deeper depth in the geodetic inversion. We jointly solved for the creep rates of these 15 fault patches along with 51 fault slip rates.

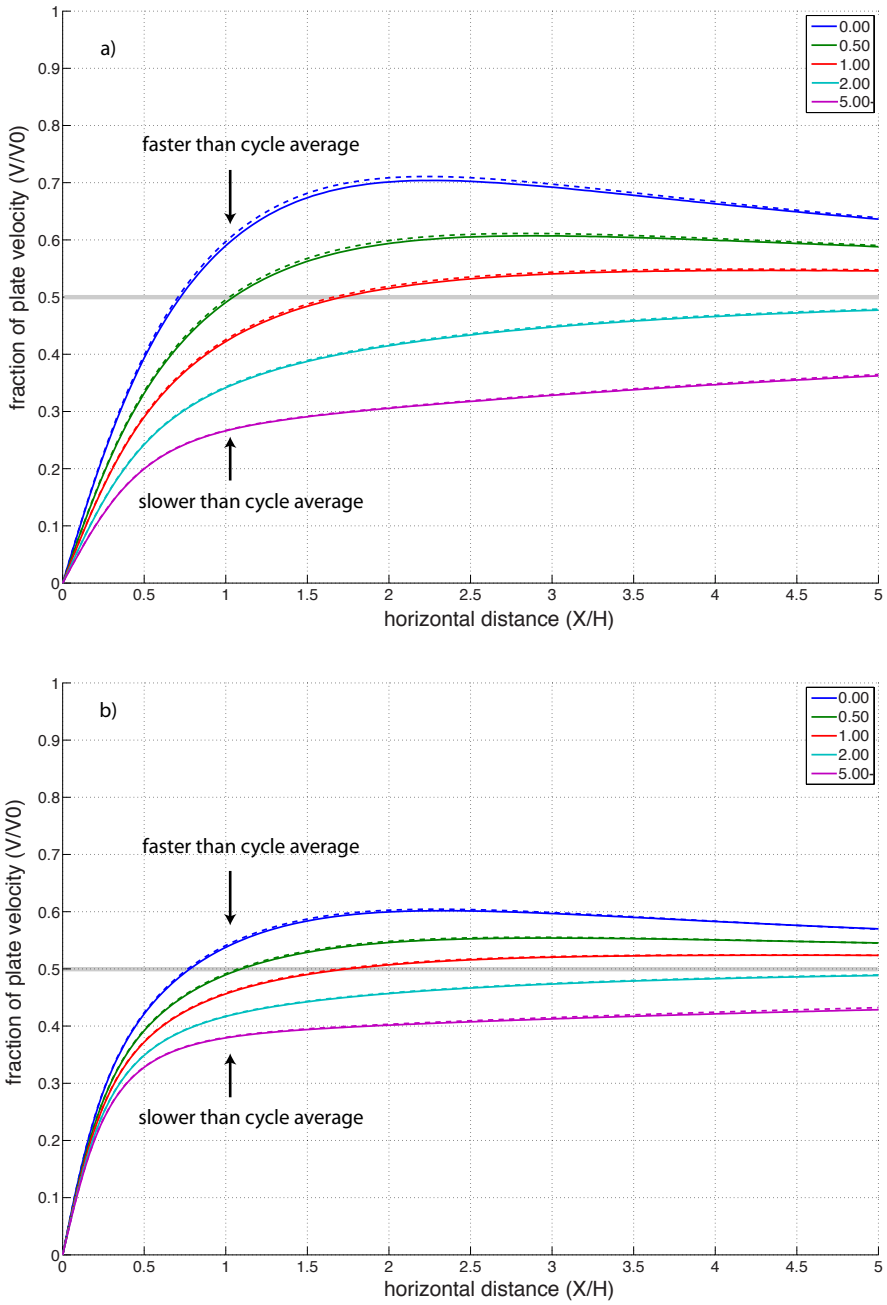

Figure 5.2: Comparison between our earthquake cycle model (solid lines) with 2D analytic models (dash lines) for two cases: thin plate 2a) and thick plate 2b). The color lines represent different time period during the earthquake cycle. The time is normalized by the Maxwell time (see (*Savage and Prescott*, 1978) for details). At times less than about 1 Maxwell time, the velocity is generally higher than the cycle average (grey line) while for greater times, the velocity is generally lower than the cycle average.

5.4 Slip rate inversion

We describe in this section the system of linear equations used for estimating slip rate on 51 fault segments $\overline{s}$ and 15 creep rate $\overline{p}$ from a combination of 1989 GPS vector velocity measurements $\overline{v_g}$, 53,791 line-of-sight (LOS) InSAR measurements $\overline{l}$ and geologic constraints on the overall velocity change $\overline{s_{geol}}$ across the plate boundary. The overview of the systems of equations is

$$\begin{bmatrix} \overline{\overline{G_g}} & \overline{\overline{E_g}} \\ \overline{\overline{G_i}} & \overline{\overline{E_i}} \\ \overline{\overline{C}} & 0 \\ 0 & \overline{\overline{S}} \end{bmatrix} \begin{bmatrix} \overline{s} \\ \overline{p} \end{bmatrix} = \begin{bmatrix} \overline{v_g} \\ \overline{l} \\ \overline{s_c} \\ 0 \end{bmatrix} \tag{5.1}$$

where G and E are the Green's function for modeled surface velocity. The subscripts g and i refer to GPS and InSAR data, respectively. G is derived from the earthquake cycle model and it depends on the plate thickness, effective viscosity, locking depth of the fault, and the earthquake sequence of the segment. E is derived from the patch dislocation model depending on the elastic property of the material. C is the constraint matrix, which includes the geologic slip rate estimates, the triple junction closure constraint, and the far-field velocity constraint. S is the smoothing matrix applied only to the patch dislocations on the creeping section.

We can decompose this system into four subsystems. The first subsystem represents the velocities from the GPS data,

$$\begin{bmatrix} \overline{\overline{G_g}} & \overline{\overline{E_g}} \end{bmatrix} \begin{bmatrix} \overline{s} \\ \overline{p} \end{bmatrix} = \begin{bmatrix} \overline{v_g} \end{bmatrix} \tag{5.2}$$

expanding this into east and north components of GPS velocities, we got

$$\begin{bmatrix} G_{11}^{east} & G_{12}^{east} & ... & G_{1n}^{east} & 1 & 0 & E_{11}^{east} & E_{12}^{east} & ... & E_{1r}^{east} \\ G_{21}^{east} & G_{22}^{east} & ... & G_{2n}^{east} & 1 & 0 & E_{21}^{east} & E_{22}^{east} & ... & E_{2r}^{east} \\ ... & ... & ... & ... & ... & ... & ... & ... & ... & ... \\ G_{m1}^{east} & G_{m2}^{east} & ... & G_{mn}^{east} & 1 & 0 & E_{m1}^{east} & E_{m2}^{east} & ... & E_{mr}^{east} \\ G_{11}^{north} & G_{12}^{north} & ... & G_{1n}^{north} & 0 & 1 & E_{11}^{north} & E_{12}^{north} & ... & E_{1r}^{north} \\ G_{21}^{north} & G_{22}^{north} & ... & G_{2n}^{north} & 0 & 1 & E_{21}^{north} & E_{22}^{north} & ... & E_{2r}^{north} \\ ... & ... & ... & ... & ... & ... & ... & ... & ... & ... \\ G_{m1}^{north} & G_{m2}^{north} & ... & G_{mn}^{north} & 0 & 1 & E_{m1}^{north} & E_{m2}^{north} & ... & E_{mr}^{north} \end{bmatrix} \begin{bmatrix} s_1 \\ s_2 \\ ... \\ s_n \\ s_{east} \\ s_{north} \\ p_1 \\ p_2 \\ ... \\ p_r \end{bmatrix} = \begin{bmatrix} v_1^{east} \\ v_2^{east} \\ ... \\ v_m^{east} \\ v_1^{north} \\ v_2^{north} \\ ... \\ v_m^{north} \end{bmatrix}$$

(5.3)

where v_i^{east} and v_i^{north} is the i^{th} vector GPS measurement and G_{ij}^{east} and G_{ij}^{north} is the model vector velocity for i^{th} GPS due to a unit of slip rate s_j along the j_{th} fault segment. E_{ij}^{east} and E_{ij}^{north} are the modeled surface velocity for i_{th} GPS due to a unit creep rate p_j along the j_{th} creep patch. s_{east} and s_{north} are two unknowns representing the constant adjustment to the whole GPS velocity data.

The second subsystem represents the line-of-sight (LOS) InSAR velocity measurement, in direction $\overline{n} = (n^{east}, n^{north}, n^{up})$

$$\begin{bmatrix} \overline{\overline{G_i}} & \overline{\overline{E_i}} \end{bmatrix} \begin{bmatrix} \overline{s} \\ \overline{p} \end{bmatrix} = \begin{bmatrix} \overline{l} \end{bmatrix} \tag{5.4}$$

we can write it as

$$\begin{bmatrix} G_{11}^{east}n_1^{east} + G_{11}^{north}n_1^{north} & G_{12}^{east}n_1^{east} + G_{12}^{north}n_1^{north} & ... & G_{1n}^{east}n_1^{east} + G_{1n}^{north}n_1^{north} & 1 & E_{11}^{east}n_1^{east} + E_{11}^{north}n_1^{north} & E_{12}^{east}n_1^{east} + E_{12}^{north}n_1^{north} & ... & E_{1r}^{east}n_1^{east} + E_{1r}^{north}n_1^{north} \\ G_{21}^{east}n_2^{east} + G_{21}^{north}n_2^{north} & G_{22}^{east}n_2^{east} + G_{22}^{north}n_2^{north} & ... & G_{2n}^{east}n_2^{east} + G_{2n}^{north}n_2^{north} & 1 & E_{21}^{east}n_2^{east} + E_{21}^{north}n_2^{north} & E_{22}^{east}n_2^{east} + E_{22}^{north}n_2^{north} & ... & E_{2r}^{east}n_2^{east} + E_{2r}^{north}n_2^{north} \\ ... & ... & ... & ... & ... & ... & ... & ... & ... \\ G_{m1}^{east}n_m^{east} + G_{m1}^{north}n_m^{north} & G_{m2}^{east}n_m^{east} + G_{m2}^{north}n_m^{north} & ... & G_{mn}^{east}n_m^{east} + G_{mn}^{north}n_m^{north} & 1 & E_{m1}^{east}n_m^{east} + W_{m1}^{north}n_m^{north} & E_{m2}^{east}n_m^{east} + E_{m2}^{north}n_m^{north} & ... & E_{mr}^{east}n_m^{east} + E_{mr}^{north}n_m^{north} \end{bmatrix} \begin{bmatrix} s_1 \\ s_2 \\ ... \\ s_n \\ s_{los} \\ p_1 \\ p_2 \\ ... \\ p_r \end{bmatrix} = \begin{bmatrix} l_1 \\ l_2 \\ ... \\ l_m \end{bmatrix}$$

(5.5)

where l_i is the i^{th} InSAR LOS velocity measurement. This equation is similar to the equation 5.3. Variable look vectors defined by n_i^{north} and n_i^{east}, are used to

project the east and north component of velocity into radar line of sight. s_{los} is the unknowns representing the constant adjustment to the whole InSAR LOS velocity.

The third subsystem $\overline{\overline{C}}\overline{s} = \overline{s_c}$ represents three types of geological constraints represented by the following three matrix: $\overline{\overline{I}}$, $\overline{\overline{C_{tot}}}$ and $\overline{\overline{C_{tri}}}$ respectively. 1) The a-priori estimates of slip rate from the geologic data on 56 segments $\overline{s_{geol}}$. 2) The constraint that the sum of slip rate on sub-parallel fault strands must equal the total slip rate across the plate boundary ($\overline{s_{tot}}$ = 45 mm/yr). 3) At the fault junctions (9 fault junctions) where two or more sub-parallel faults connects and converge into one main fault, the slip rate on the main fault must equal to the sum of the sub-parallel faults ($\overline{s_{tri}} = 0$). We wrote it as:

$$\begin{bmatrix} \overline{\overline{I}} \\ \overline{\overline{C_{tot}}} \\ \overline{\overline{C_{tri}}} \end{bmatrix} \bar{s} = \begin{bmatrix} \overline{s_{geol}} \\ \overline{s_{tot}} \\ \overline{s_{tri}} \end{bmatrix} \tag{5.6}$$

The fourth subsystem $\overline{\overline{S}}\overline{p} = 0$ represents the smoothness constraints on the dislocation patches. The smoothness matrix penalize the first derivative of the fault creep rate distribution.

The equations 5.2 and 5.4 were normalized by the uncertainty in each component of the geodetic measurement. In addition we introduced four weighting constants to the four sub-systems of equations to have a sense of control on the slip rates solutions. The relative weights were determined by grid-search method on the RMS misfit to the GPS and InSAR data (Figure 5.3).

Before applying the real data to this inversion problem, we carried out two synthetic tests to validate the computer code. In the first test we generated synthetic GPS and InSAR velocity data using a known set of fault slip rates. Then we inverted for the slip rates to confirm the recovered slip rates match the input slip rates to within uncertainties even for the case when the constraint matrix C is down weighted. In the second test we checked the consistency of the constraint matrix C. We lowered the weights to make the GPS and InSAR data negligible

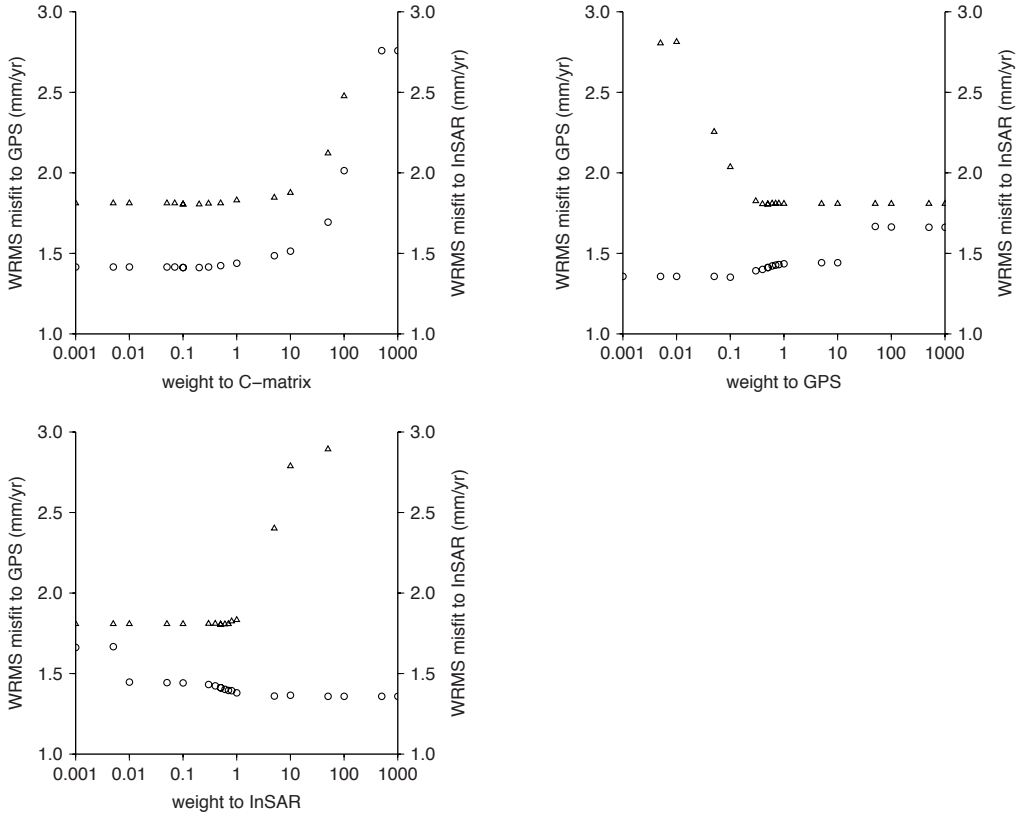

Figure 5.3: Determine the relative weighting factors. The triangles are the weighted RMS misfit to GPS data and the circles are the weighted RMS misfit to InSAR data. Good relative weights are around 0.1 to 1 in this case.

in the inversion matrix. Thus the fault slip rates should depend only on the constraint matrix C. If the three conditions required by the constraint matrix are self-consistent, the solution should be close to the a-prior fault slip rates regardless the weight to the constraint matrix C. The test result verifies that the constraint matrix is designed consistently.

We added Gaussian random noise to the input data and repeated the inversions for 50 times. The amplitude of the random noise was set according to the standard deviations of the measurements. Then we computed their mean and the standard deviations as the final fault slip rates result.

5.5 Results

The quality of fit to the GPS and InSAR data are summarized in Table 5.1. Table 5.1 shows the statistics of the misfits for three different models: half-space models (hereafter HS), the thick-plate viscoelastic model (hereafter TK), and the thin-plate viscoelastic model (hereafter TN) respectively. The χ^2 misfit is defined as the squared sum of the residuals normalized by the standard deviation for each velocity measurement $\chi^2 = \frac{1}{N}\sum_{i=1}^{N}\left(\frac{o_i - m_i}{\sigma_i}\right)^2$ where o_i is the data, m_i is the model, and σ_i is the uncertainties for N measurements. Unlike other studies (*Mccaffrey*, 2005) we chose not to scale the formal uncertainties of the GPS data before calculating the χ^2 misfit. The χ^2 misfit to GPS is 24.3, 23.2 and 26.3 for the HS, the TK, and the TN model respectively. Our χ^2 misfit to GPS is not unreasonable given rather small formal uncertainties of the GPS velocity ($\sim$ 0.3 mm/yr). If we increase the formal uncertainties of the GPS by a factor of 5, we would get a χ^2 misfit smaller than 1. The formal uncertainties of InSAR data are quite large ($\sim$ 5 mm/yr), reducing the χ^2 misfit to InSAR to be about 0.3.

Another measure of the quality of the fit is through the weighted RMS defined as $WRMS = \sqrt{\frac{\sum_{i=1}^{N}\left(\frac{o_i - m_i}{\sigma_i}\right)^2}{\sum_{i=1}^{N}\frac{1}{\sigma_i^2}}}$. The weighted RMS may be better than the χ^2 misfit since it does not depend on possible errors in the reported uncertainties. The TK model yields the smallest misfit with weighted RMS residual of GPS being 1.57 mm/yr compared to 1.61 mm/yr for the HS model and 1.67 mm/yr for the TN model. The weighted RMS residual to InSAR, which is 1.42 mm/yr for HS, 1.35 mm/yr for TK and 1.33 mm/yr for TN seem less sensitive to different plate thickness. From Table 5.1 the HS model and TN model give a larger misfit to GPS, which indicates that the thick plate model is more appropriate over a large scale covering the SAF. We will focus on discussing the result from the thick plate model in the following sections.

5.5.1 Fault slip rate

Figure 5.4 and Table 5.2 provide the fault slip rates constrained by GPS and InSAR after the inversion. There are 51 fault segments labeled by the index

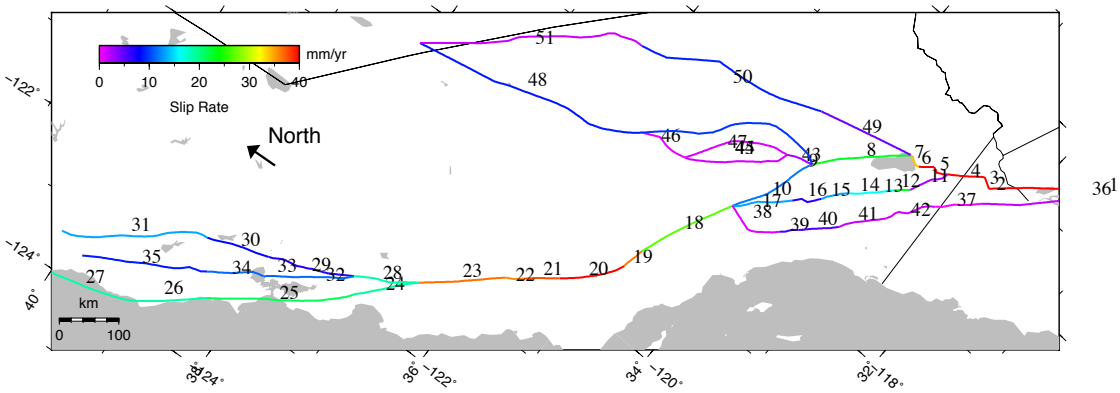

Figure 5.4: Fault slip rates constrained by GPS and InSAR. The slip rates for the thick plate earthquake cycle model are shown by the color lines. The numbers on each fault line are their index in Table 5.2

in 5.4. A detailed summary of the fault slip rates for the HS, TK and TN model and the a-prior geological slip rates are shown in Table 5.2. The information on the locking depth and the earthquake recurrence interval is also included in Table 5.2.

Table 5.1: Data misfits to three different models.

	Half-space	Thick-plate	Thin-plate
χ^2 misfit to GPS	24.3	23.2	26.3
WRMS to GPS (mm/yr)	1.61	1.57	1.67
χ^2 misfit to InSAR	0.32	0.29	0.28
WRMS to InSAR (mm/yr)	1.42	1.35	1.33

Table 5.2: Parameters for the earthquake cycle model of the SAF.

Index	Name	s_{geol}	T_{rec}(year)	D(km)	$s_{elastic}$	$\sigma_{elastic}$	s_{thick}	σ_{thick}	s_{thin}	σ_{thin}
1	S_Cerro_Prieto	40	200	5.1	39.9	2.1	43.6	1.3	52	0.6
2	Cerro_Prieto	40	200	5.1	43.6	1.7	43.3	1.2	46.4	0.2
3	Geothermal_stepover	40	200	5.1	41.4	0.8	44.7	0	44.6	0
4	Imperial	40	200	5.9	56.8	2.5	45.5	0.4	47.3	0.4
5	Imerial_stepover	25	200	5.9	25.3	3.1	42.6	1.2	45	0.5
6	Brawley	25	200	15.3	23.2	3	41.2	1	45.4	0.5
7	SaltonSea_stepover	25	200	15.3	25.7	1.8	33.9	1.1	36	0.6
8	Coachella	24.9	200	11.5	21.6	0.9	22.9	2.3	24.7	2.4
9	Palm_Springs	23	2000	16.4	21	1.9	24.2	2.7	23.2	2.2
10	San_Bernardino	16	200	17.8	11.8	1.6	11.8	2.9	4.5	2.6
11	Superstition_Hills	15	600	10.8	5.6	2.4	2.6	1.3	1.5	0.5
12	Borrego_Mountain	15	550	10	12.6	1.8	23.1	1.3	25	0.9
13	Coyote_Creek	15	500	10	13.9	1.8	16.2	1.5	16.6	0.9
14	Anza	15	300	10	13.4	3.2	16.4	1.8	17.5	1.1
15	Clark	15	300	12	15.7	2.7	13.2	2.1	13.4	1.2
16	SJ_Valley	12	450	15	13.9	3.7	6.8	2.4	12.1	2.2
17	SJ_Mountains	12	500	15	6.9	2.5	13.2	2.3	25.8	1.8
18	Mojave	33	220	15	26.4	1.5	26.8	1.1	30.9	1.3

Table 5.2 – Continued

Index	Name	s_{geol}	T_{rec}(year)	D(km)	$s_{elastic}$	$\sigma_{elastic}$	s_{thick}	σ_{thick}	s_{thin}	σ_{thin}
19	S_Carrizo	36	250	15	36.8	2.3	36.2	0.7	36.5	0.7
20	N_Carrizo	36	200	15	43.4	1.8	40.7	0.7	42.8	0.7
21	Cholame	36	200	12	38.9	2.4	37.6	0.6	39.2	0.7
22	Parkfield	36	20	12	34.1	2.2	35.5	0.8	36.1	0.8
23	Creeping	36	400	12	33.1	2	36.5	0.6	39.4	0.6
24	Santa_Cruz_Mt	21	150	6.3	16.5	1.3	19.1	1	22	1
25	SA_Peninsula	21	230	16.2	21.9	1.4	21.2	0.7	22.7	0.8
26	SA_N_Coast	25	230	15.5	10.2	2.5	18.8	1.4	22.2	1.4
27	N_SA_N_Coast	25	270	13.2	25.5	2.4	18.5	1.2	19.8	1.3
28	S._Calaveras	19	300	1.2	18.9	1	18.5	0.7	19.1	0.7
29	N._Calaveras	7	550	0.3	6.8	1.6	6.7	0.9	6.1	0.9
30	Concord	7	5000	0.8	7.7	1.1	8.3	1.3	9.2	1.2
31	Green_Valley	5	500	12	14	1.7	13.2	1.6	12.1	1.9
32	S._Hayward	12	200	5.1	8.5	2.4	11.4	1	13.4	1
33	N._Hayward	12	300	4.4	10.8	2	11.2	1.1	13	1.1
34	Rodgers_Creek	12	400	4.5	12.8	2	11.3	1.1	12.6	1.1
35	Maacama	10	250	1.6	8.7	1.2	8.8	0.9	11.1	0.9
36	S_Laguna_Salada	5	1000	9	1.5	1.4	1.8	1.2	0	0
37	Laguna_Salada	5	1000	9	1.1	1.7	0	0	0	0

Table 5.2 – Continued

Index	Name	s_{geol}	T_{rec}(year)	D(km)	$s_{elastic}$	$\sigma_{elastic}$	s_{thick}	σ_{thick}	s_{thin}	σ_{thin}
38	Elsinore_Chino	5	2000	10	0.2	0.5	0.9	1	0	0
39	Elsinore_GlenIvy	5	1000	10	4.6	2.8	5.8	1.5	6.6	1
40	Elsinore_Temecula	5	1000	10	3	2.6	5.4	1.4	4.5	0.8
41	Elsinore_Julian	5	1500	10	2.6	2.4	1.7	1.6	0.2	0.5
42	Elsinore_Coyote_Mt	5	1500	10	0.6	1.3	1.4	1.5	0	0
43	Connector1	6	5000	15	1.2	1.9	2.7	1.3	6.4	1.1
44	Lenwood	5	3000	7.9	2.3	1.1	1.2	1.1	0.4	0.9
45	Helendale	1	3000	4.2	0.7	0.8	1.3	1.1	3.5	1.3
46	Connector2	6	3000	15	0.5	0.8	0.7	0.8	0.2	0.4
47	Calico	1	3000	10	8.9	1.1	9.7	0.8	10.8	0.7
48	Owens_Valley	4	3000	11.5	9.8	0.8	8.7	0.6	7.8	0.7
49	ECSZ_South	0.1	3000	10	1.7	2	4.6	2	4.9	2.2
50	ECSZ_East	5	1000	10	9.2	1.1	9	1	6.3	1.1
51	Death_Valley	5	1000	1.5	3.4	0.8	1.6	0.5	2.8	0.5

Note s_{geol} is the geological slip rate. T_{rec} is the recurrence interval. D is the fault locking depth. $s_{elastic}$, $\sigma_{elastic}$, s_{thick}, σ_{thick}, s_{thin} and σ_{thin} are the geodetic fault slip rates with uncertainties. The slip rate is in mm/yr.

5.5.2 Data, model and residuals

Figure 5.5 shows the horizontal GPS velocity vectors and the velocity predicted by the thick plate model. The model captures the majority of the right-lateral shear due to interseismic locking across the Pacific-North America plate boundary. The map projection in Figure 5.5 is chosen to highlight the velocity component parallel to the far-field plate motion and the velocity component perpendicular to the plate motion. We are interested in examining the velocity field decomposed into these two components separately. The far-field plate motion is aligned with the long edge of the Figure 5.5, defined as an Euler pole. And the velocity aligned with the short edge of Figure 5.5, shows the deviation of the velocity field from the direction of plate motion. Extension or compression motion can be seen clearly in some regions along the SAFS. As shown in Figure 5.5, the "big bend" of the SAF produces pronounced rotation of the velocity vectors toward Northwest direction. This is because that the north-south compression at the big bend produced east-west extension. Our model is able to match the amount of extension quite well over the "big bend". In Central California, the rotation of the local GPS vectors near the creeping section can be associated with the asperities in the shallow crustal layer near Parkfield. A significant extension of the East California Shear zone can be seen in the GPS velocity vectors. It is not clear what caused the compression between the Maacama fault and the Green Valley fault in Northern California.

The difference between the model and the observed GPS velocities is best illustrated in the residual velocity field as shown in Figure 5.5. We can learn a great deal from this residual velocity field. We found that most residual velocities are perpendicular to the plate motion, and the velocity residual parallel to the plate motion is generally small (< 2mm/yr). It indicates that our model did reasonably well in matching the right lateral shear of the strike-slip faults. There are two places that are exceptions: The first one is shown as the velocity vectors of the islands west of the coast of California. It seems that our model underestimates the shear motion of these islands. The second one is that the GPS data west of Cholame-Carrizo section of the SAF shows an evident asymmetry. This asymmetry of the strain

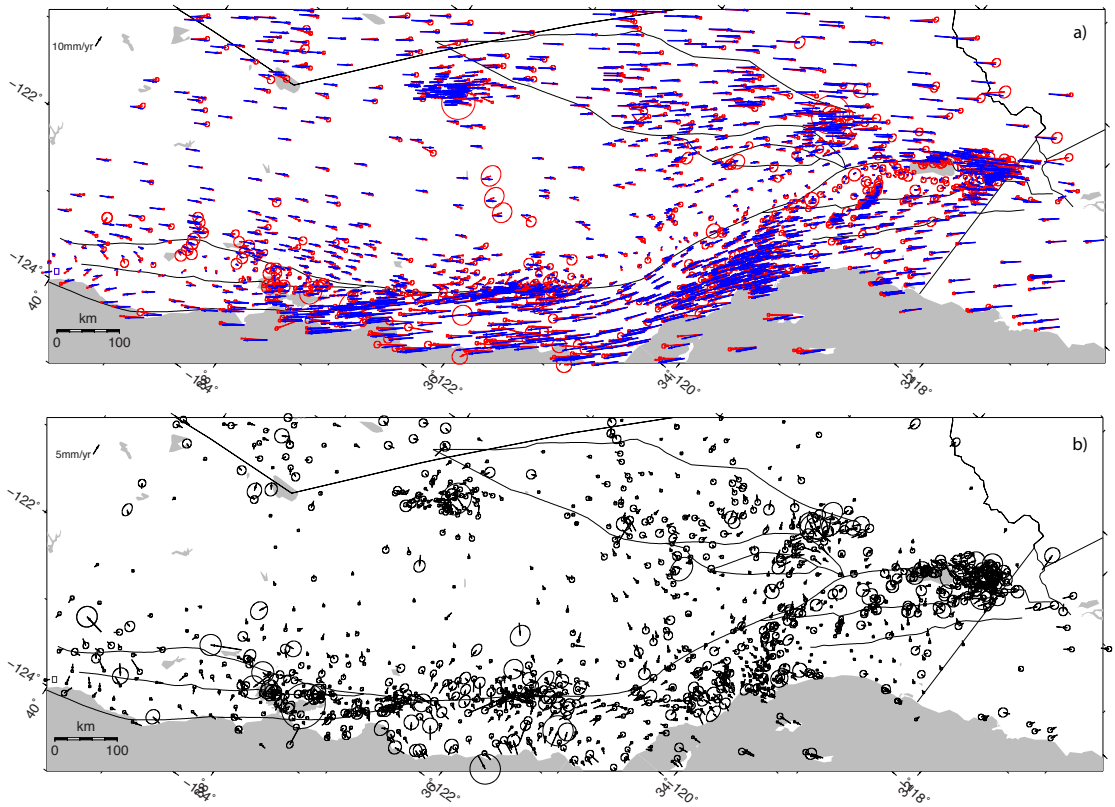

Figure 5.5: The fit to GPS data for the thick plate model. In the upper panel a) the red arrows show the observed GPS horizontal velocity with 1σ uncertainties. The blue arrows show the predicted horizontal velocity from our model. The bottom panel b) shows the residual (observation - model) velocity vectors. Note the different scales used in the two figures.

rates has been noticed before (*Lisowski et al.*, 1991). *Schmalzle et al.* (2006) has attribute this asymmetry to laterally varying crustal properties. We investigated whether the dipping fault geometry can explain the asymmetric surface velocity at the Carrizo segment in the discussion section.

The InSAR observation added in the inversion provides improved resolution at shallow depth (< 10 km). As shown in Figure 5.6 our model matches the InSAR LOS velocity data well at the creeping section. The model can reproduce the broad deformation measured by the InSAR. Significant ($> 0.5\sigma$) residuals (observation - model) are shown in Figure 5.6. There are residuals north of the creeping section near the Bay area, which could be fixed after we include more creeping faults. The residual near the Maacama fault and the Green Valley fault in Northern California is probably due to a combined effect of fault creep and inaccurate locking depth. There are also residuals near the Imperial fault at the southern tip of Salton Sea.

5.5.3 Profiles

The profiles of the GPS velocity and InSAR LOS velocity and the predicted surface velocity show that our model can accurately reproduce the interseismic deformation across the SAFS (Figure 5.7 and 5.8). The locations of the profiles are shown in Figure 5.1, labeled by the alphabet letter in the upper right corner. The left side of the profiles is on the Pacific side and the right side of the profiles is on the North American side. The velocity measurements are decomposed into two components: parallel to the plate motion and perpendicular to the plate motion in order to reveal details of the transcurrent, transpression, and transtension motion. The GPS velocity vectors are decomposed into two components: parallel to the plate motion shown as the triangles comparing to the model velocity (solid line) and perpendicular to the plate motion shown as the squares comparing to the model velocity (dashed line). Note the zero-level of the plate perpendicular velocities is shifted to -25 mm/yr for display. At Mojave segment we can see a good agreement between the observation and the predicted surface velocity in both magnitude and direction (Figure 5.5). The velocity profiles are in consistence with the far-field plate motion as required by the inversion.

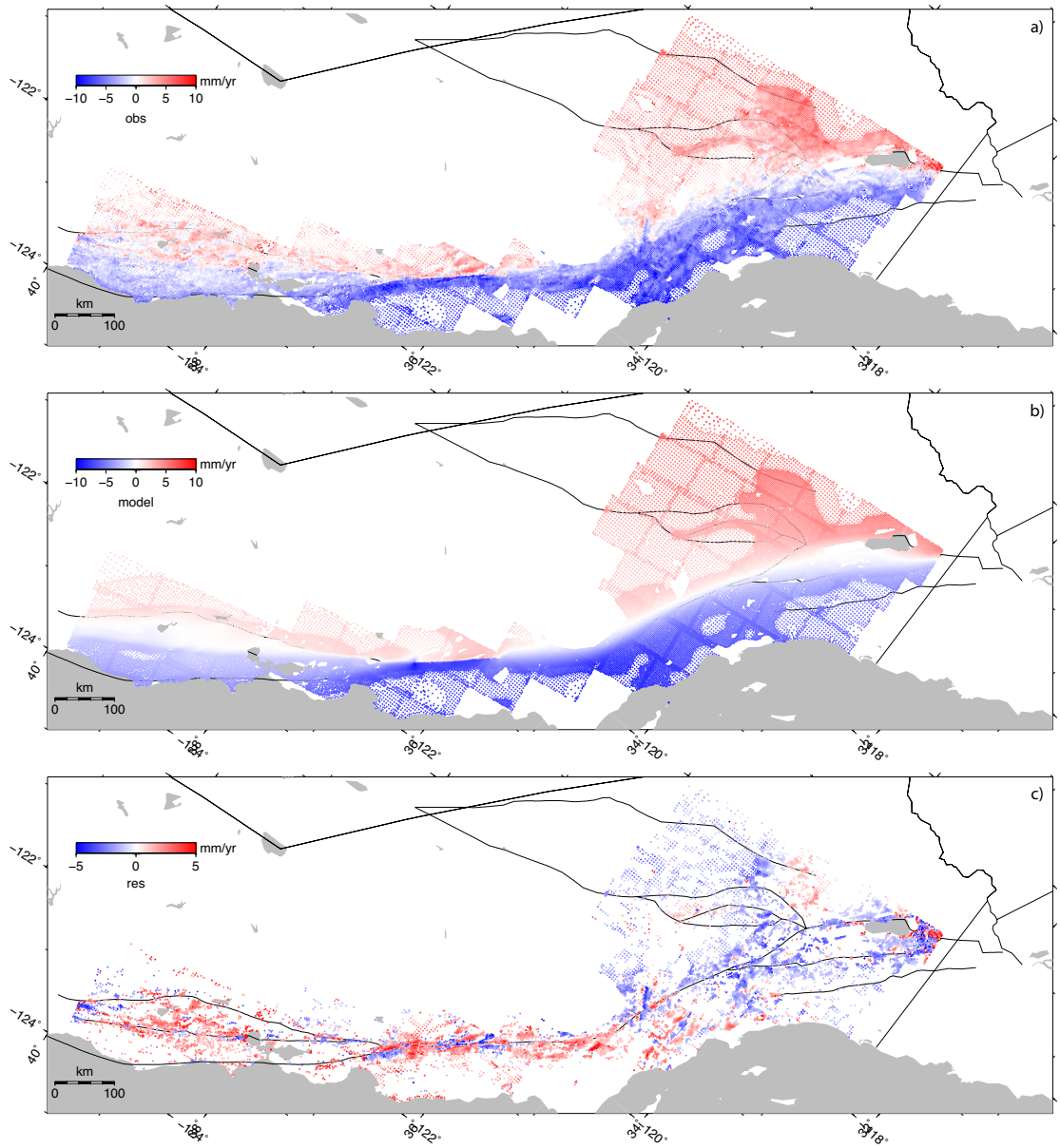

Figure 5.6: The fit to the InSAR LOS velocity data. a) Observed InSAR LOS velocity data. b) Predicted InSAR LOS velocity data. c) Significant ($> 0.5\sigma$) residuals (observation - model) of the InSAR LOS velocity data.

We compared three different models: elastic half-space model (blue line), thick-plate earthquake cycle model (green line) and thin-plate earthquake cycle model (red line) with the geodetic data. The difference between these models is subtle but we indeed can distinguish them using GPS velocity measurements. We found that in many places the thin plate model predicts a smaller velocity step in the far field. This could be due to the current situation where many faults of the SAF are late in their earthquake cycle so, as shown in Figure 5.2, the far-field velocities are smaller than the cycle average. In order to fit the observed GPS and InSAR velocities, the inversion must increase the fault slip rates. For this thin-plate solution, the sum of the slip-rate across parallel faults commonly exceeds the 45mm/yr constraint. It seems that the thin-plate model can't satisfy the far-field condition and the viscoelastic coupling effect simultaneously. One conclusion from this result is that the thin-plate model is not appropriate and a thicker plate must be used to better match the geologic slip rates and the far-field motion.

5.5.4 Slip-rate comparison

To further investigate the viscoelastic effect on the slip rate estimation we have plotted the recovered slip rates for the plate model versus the recovered slip rates for the half-space model. The results are shown in Figure 5.9. The slip rates estimation is contaminated by noise in the data and it's not easy to determine if the earthquake cycle effect is significant. To quantify the relationship between the slip rate results we performed linear regression using the weighted total least squares method. This method takes into account the noise of both variables to produce uncertainties of the linear regression. The slope of the best-fitting line indicates whether the two slip rates are different. We found that the best-fitting slope is 1.09 ± 0.02 for the thin plate model case. The slope reduced to 1.04 ± 0.02, much closer to 1 for the thick plate model. In this statistic test we disregarded fault 5 and 6 because their slip rates are poorly resolved. When we included them in the linear regression, the slopes increased slightly: 1.12 ± 0.02 for the thin plate case and 1.07 ± 0.02 for the thick plate model. From Figure 5.9 we found that the slip rate from the viscoelastic models are in general higher than the half-space rates.

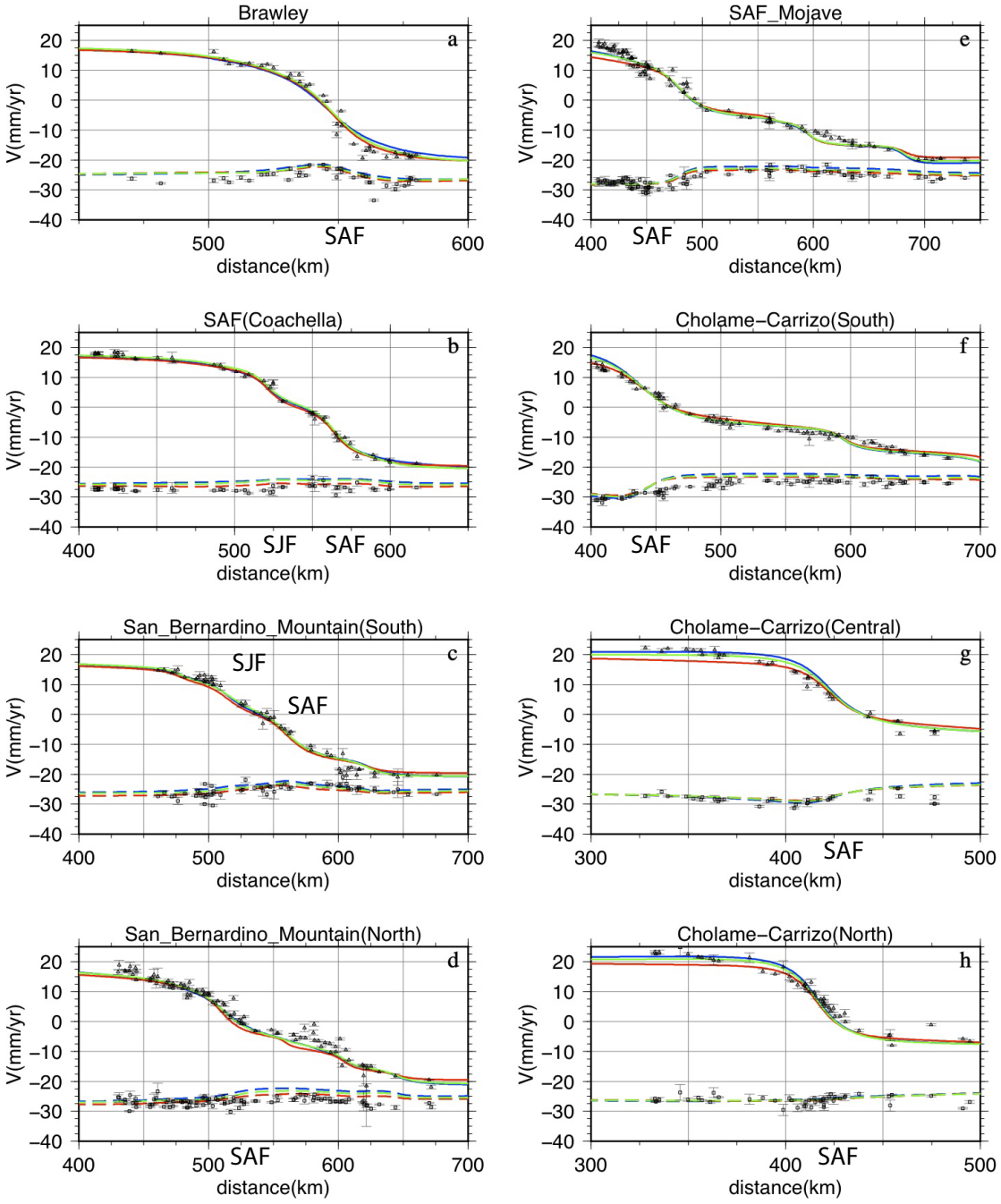

Figure 5.7: Cross-sections showing the GPS data and its fit to the 3 models: elastic half-space model (blue line), thick-plate earthquake cycle model (green line) and thin-plate earthquake cycle model (red line). The GPS velocity vectors are decomposed into two components: parallel to the plate motion shown as the triangles comparing to the model velocity (solid line) and perpendicular to the plate motion shown as the squares comparing to the model velocity (dashed line). The main faults are labeled on the figures with explanations below: SAF-San Andreas fault, SJF-San Jacinto fault, Hay-Hayward fault, GRV-Green Valley fault, Ma-Maacama fault, BS-Bartlett Springs fault, Cala-Calaveras fault, Rog-Rodgers Creek fault.

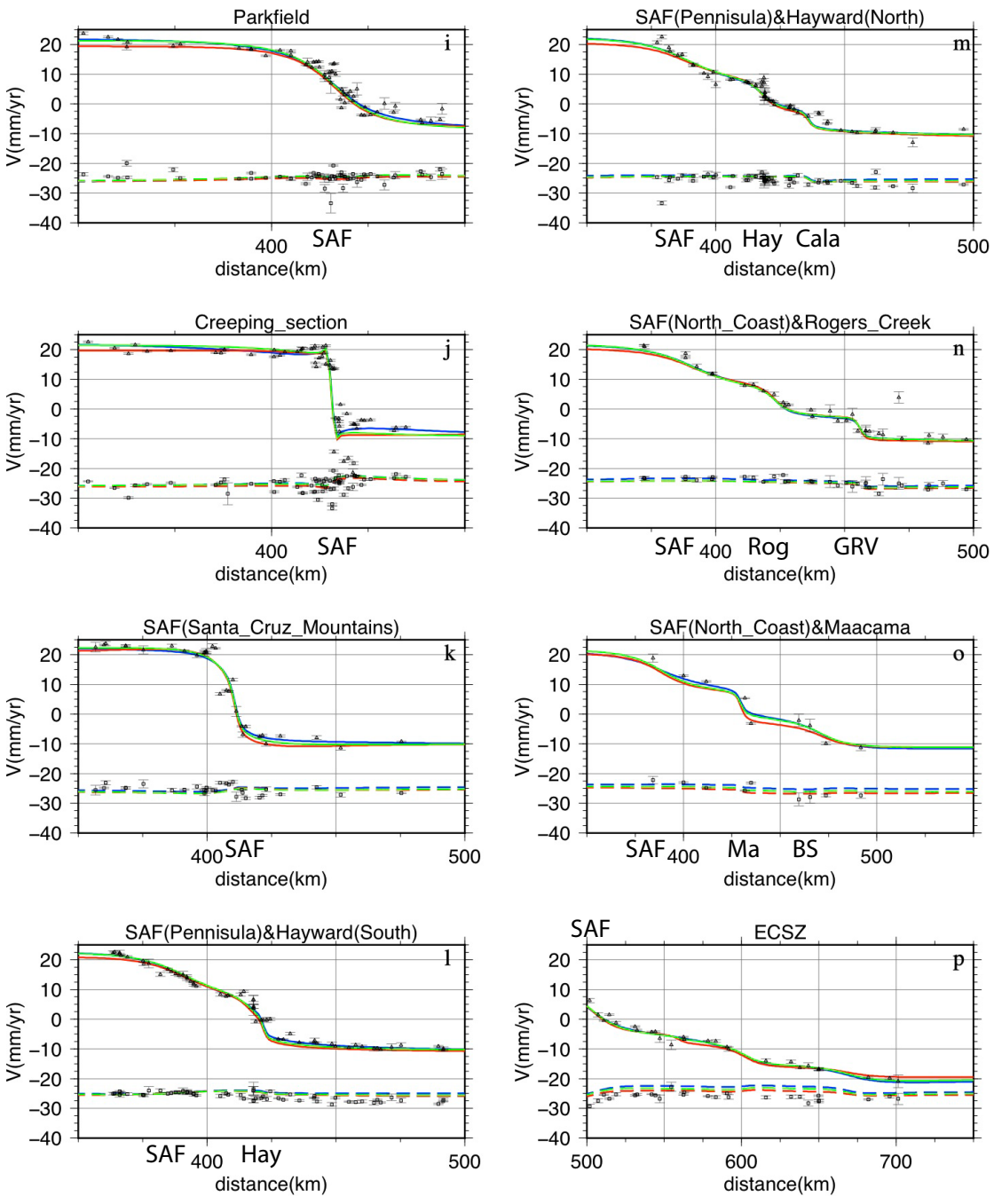

Figure 5.8: Cross-sections showing the GPS data and its fit to the models – Figure 5.7 continued.

This increase is more evident for the thin plate case. For instance on the Mojave section (Fault 18), the inverted slip rate is 30.9 mm/yr for the thin plate model much higher than 26.4 mm/yr from the half-space model. The thick plate model predicts 26.8 mm/yr which is not very different from the elastic model prediction. This comparison result implies that the half-space model can be approximated to the thick-plate model to first order.

5.6 Discussions

5.6.1 Northern SAF

The fault model north of the Bay area in California consists of the SAF to the west, the Rodgers Creek - Maacama fault in the center, and the Green Valley - Bartlett Spring fault to the east. The elastic deformation caused by closely spaced parallel faults overlap each other making it difficult to accurately resolve the fault slip rate on individual fault. Moreover the deformation might be influenced by aseismic slip, which is not well resolved by the sparse GPS data. The dense coverage of the L-band InSAR data used in this study may help distinguish different models. Previous fault slip rate results from geodetic data *Freymueller et al.* (1999); *Mccaffrey* (2005); *Savage et al.* (1998) imply consistent high slip rates on the SAF of 18-21 mm/yr. Our estimate of the slip rate of the SAF is 19 mm/yr. The Rodgers Creek - Maacama fault is less well constrained: the estimated slip rates vary from 7-15 mm/yr from previous studies. We found evidence that the Rodgers-Creek fault is creeping at surface (*Tong et al.*, 2013) so those models didnt appropriately account for aseismic creep is likely biased. It is not clear whether creeping occurred on the Maacama fault and what is the depth extent of the aseismic creep. The Green Valley - Bartlett Spring fault in general has smaller slip rate of 7 mm/yr. *Freymueller et al.* (1999) infer the that the Bartlett Spring fault is creeping at all depth although we didnt find convincing evidence of surface creep on that fault from InSAR. Our model infers that the slip rate of Maacama fault is 9 mm/yr and the slip rate of Rodgers-Creek fault to be 11 mm/yr. We found a high slip rate of 13 mm/yr on the Bartlett Spring fault and lower slip rate

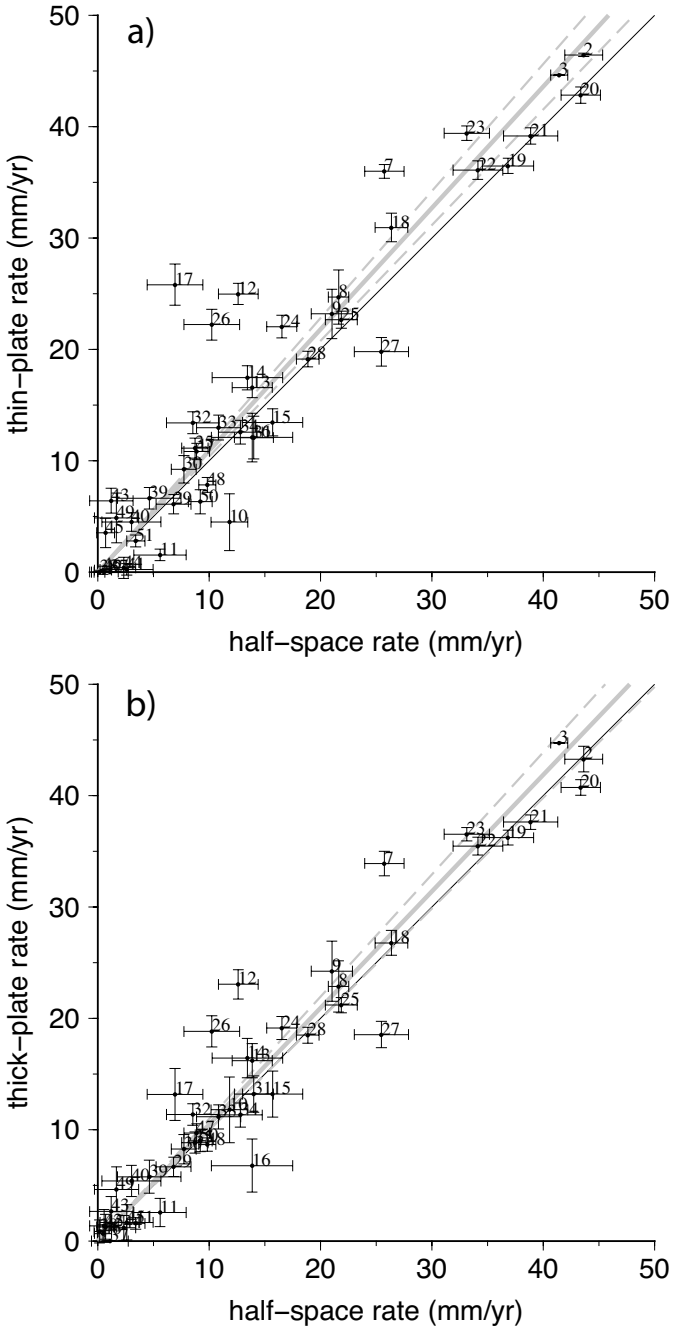

Figure 5.9: Plots of slip rates recovered from the best-fitting plate model versus the slip rates recovered from the half-space model. a) is for the thin plate and b) is for the thick plate model. The index for each fault segment corresponds to the ones provided in Table 2. The thin black line shows the line with slope 1. The solid gray line shows the linear regression using total least squares method. The dashed gray lines are the bounds (3σ) of the linear regression. The thin-plate estimates are significantly higher than the half-space rates.

of 8 mm/yr on the Green Valley fault.

To the south of the Bay area, our fault model consists of the SAF (Santa Cruz Mountain section) and the Calaveras fault. The central and southern Calaveras fault branches into Southern Hayward fault and Northern Calaveras - Concord fault. Abundant geodetic observation including GPS and InSAR is available over the Bay area. The broad deformation as well as the small-scale creep distribution of the faults in the Bay area has been studied extensively (*Burgmann et al.*, 2000; *Johanson and Burgmann*, 2005). Even though the slip rate estimates of these close spacing parallel faults such as the SAF (Santa Cruz Mountain section) and the Southern and Central Calaveras fault are still in discrepancy, perhaps due to the differences in the fault geometry and modeling approach. Our model inferred the slip rates of 19-21 mm/yr on the SAF and 18 mm/yr on the Southern Calaveras fault. The high slip rate on the Southern Calaveras fault is probably because our model doesn't include subsidiary faults offshore. In our model the Hayward fault has a slip rate of 11 mm/yr and the Northern Calaveras has a slip rate of 7 mm/yr in good agreement with the geological slip rate.

5.6.2 Creeping section

The creeping section of the SAF is deemed as a section that is devoid of significant earthquake hazard. Due to low effective friction coefficient and friction stability (*Moore and Rymer*, 2007) the tectonic stress is released by aseismic creep in the upper crust instead of major earthquakes. The moment released by seismicity recorded by modern instruments at the creeping section is usually negligible compared to aseismic creep. Recent studies at the creeping section (*Rolandone et al.*, 2008; *Titus et al.*, 2006; *Ryder and Burgmann*, 2008) suggests that the creeping section is partially locked and may accumulate seismic moment at shallow depth. This is the first time that the L-band ALOS InSAR data image the creeping section with clear signals. Our creep model is tightly constrained by the near-fault InSAR and GPS data. As shown in Figure 5.10, the creep model can reproduce the surface creep rate measurements (0-3 km depth) reasonably well. We found that the long-term fault slip beneath the brittle crust (below 12 km)

at the creeping section is 36 mm/yr and the distribution of the creeping rate at the brittle crust (between 3 km to the 12 km) is heterogeneous ranging from 10 mm/yr underneath Parkfield to 30 mm/yr in the center of the creeping section to 22-25 mm/yr in the northern portion of the creeping section. Our finding on the slow creep rates confirms previous models based on independent GPS data and C-band radar interferograms. There are several possible implications of the deficit of the creep rate in comparison to the long-term slip rate. One of the possibilities is that there are small asperities at the creeping section. These asperities may be small patches with high friction or friction instability to resist the shear stress over decadal scales. They may fail along with adjacent earthquakes that have enough shear stress perturbation (*Beeler et al.*, 2001). The second explanation is that the aseismic creep is in response to the shear stress rate due to viscoelastic relaxation of the asthenosphere (*Ben-Zion et al.*, 1993): right after an earthquake the creep rate will increase and late in the cycle the creep rate will decrease. In the northern section the Pacines segment of the Calaveras fault lies at 4 km east and it may be creeping as well.

5.6.3 Carrizo segments

We noticed that the slip rate of the north Carrizo segment (index 20) is anomalously high ($\sim$ 40 mm/yr). It's curious whether the slip rate inversion could be biased by inaccurate fault geometry. It has been proposed that the geometry of the SAF is significantly different from vertical. In the southern SAF near Coachella valley the fault is dipping toward northeast and near the "big bend" region the fault is dipping toward southwest (*Fuis et al.*, 2012). The overall shape of the fault surface is similar to a "propeller". The dipping geometry can be further tested using the deformation models because a dipping fault will shift the center of the strain concentration, which is observable in geodetic data. This hypothesis is tested by *Lindsey and Fialko* (2013) at the Coachella section of the SAF. The gravity and electromagnetic data suggest that the Carrizo segment maybe dipping to the west at 60°. We tested this dipping fault hypothesis using local GPS velocity data and the elastic half-space model. Only the GPS data within 30 km from profile

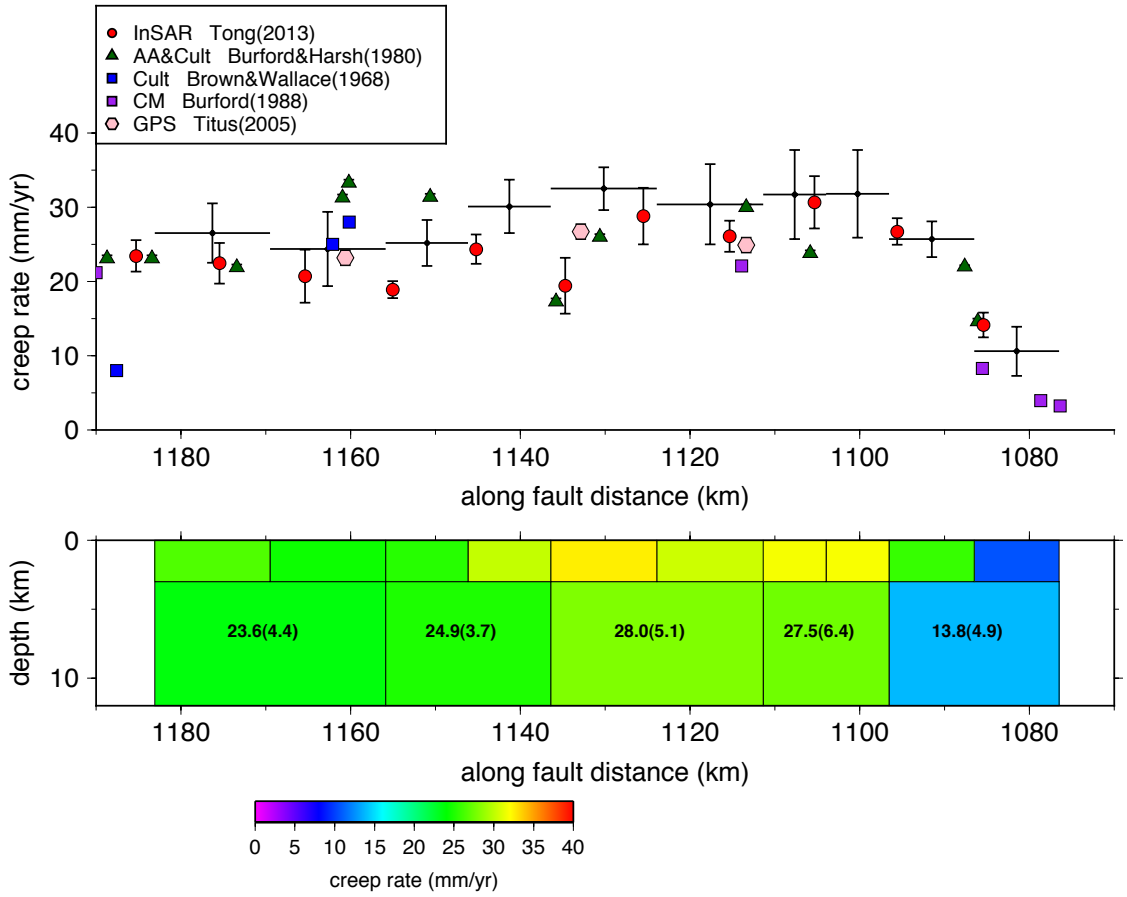

Figure 5.10: Creep rates on the creeping section of the SAF in Central California. In the upper panel the color dots show the surface creep rate measurements from independent observations such as alignment array, creepmeter, GPS and InSAR. The black horizontal lines show the creep rate near the surface (0-3 km depth) predicted by our model. In the bottom panel shows the along-strike variations of the creep rate in the upper crust (3-12 km depth). The numbers inside the creeping patches show the creep rates with uncertainties in the parenthesis.

g shown in Figure 5.1 is used in evaluating the model misfit. As shown in Figure 5.11 the deformation model with the SAF dipping to the west significantly reduces the RMS misfit of the GPS data from 2.2 mm/yr to 1.3 mm/yr. This simple model comparison suggests that the dipping SAF hypothesis is supported by the geodetic data. However the dipping geometry produces similar slip rate results as the non-dipping fault. The dipping fault geometry we incorporated was approximated by an horizontal offset of the dislocation source and we kept the locking depth the same as before. The locking depth would be sufficiently smaller if we assume the width of the fault plane constant. A model with a reduced locking depth is expected to predict a smaller slip rate. We haven't done further analysis on this segment yet. An alternative explanation of the asymmetric strain at the Carrizo segment is through laterally varying crustal properties (*Schmalzle et al.*, 2006). A weak zone with 10-25 km width to the northeast of the SAF is required to explain the observed GPS velocity.

5.7 Conclusions

In order to forecast the absolute magnitude of future earthquakes, we need an accurate estimation on the the slip budget on a particular fault in a given time window. Since the long-term slip rate estimated from geology is subject to uncertainties, present-day velocity measurement such as GPS, has been employed to estimate slip rate. In the elastic models, the influence of the viscoelastic relaxation from past earthquakes on the present-day velocity field is usually not taken into account. The viscoelastic coupling model predict faster velocity in the early earthquake cycle and slower velocity in the late earthquake cycle. According to the historical earthquake record and the estimated earthquake recurrence interval many faults in California are late in their earthquake cycle. As expected our inversion infers the slip rate to be, on average, higher than the elastic model prediction. Since the moment accumulation rate is proportional to the slip rate, the seismic hazard inferred from the earthquake cycle model would be slightly higher than those from the elastic model.

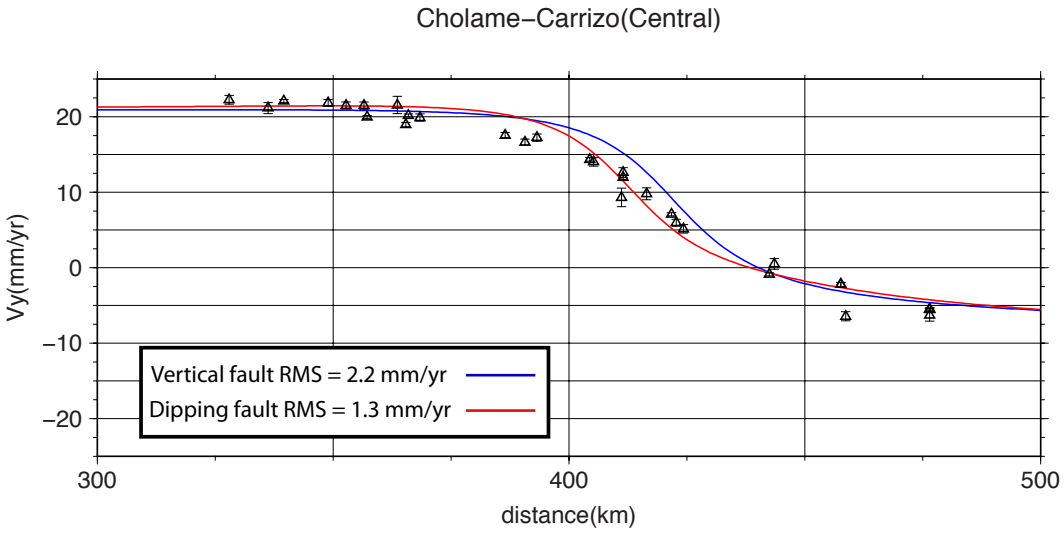

Figure 5.11: Cross-section of the Carrizo section showing the GPS fit to the vertical fault in an elastic half-space model (blue line), and the dipping fault in an elastic half-space model (red line). GPS velocity data are shown as triangles. The RMS misfit clearly shows that the dipping fault model is preferred according to the geodetic data.

However the earthquake cycle effect on the fault slip rate depends on the rheology structure of the earth. A large viscosity ($\sim 10^{21} Pa \cdot s$) of the underlying mantle or a thick elastic plate would produce negligible earthquake cycle effect. Conversely, the earthquake cycle effect would be magnified for a thin plate or low half-space viscosity. We tested two models with different plate thickness assuming a reasonable half-space viscosity of $10^{19} Pa \cdot s$. Based on the horizontal velocity from GPS we found that overall the plate is relatively thick (60 km) for the San Andreas Fault System. Consequently we infer that the slip rate from the viscoelastic coupling model is not significantly different from the elastic model. Future work should include the vertical velocity measurements to put a stronger constraint on the plate thickness and the underlying rheology structure.

An accurate estimation of the moment and strain rate also replies on quantifying the aseismic slip. It is necessary to use high resolution deformation data from InSAR to resolve accurately the aseismic factors. A failure to account for the aseismic motion may lead to an over-estimation of the slip budget on one fault and under-estimation on the adjacent fault. There are abundant aseismic observations in Central and Northern California.The creeping section of the San Andreas Fault is one of these examples. In this study the deep slip and the aseismic slip are simultaneously determined in the inversion and we found that the aseismic slip is slower than the deep slip by as much as 6 mm/yr in the middle of the creeping section. From a pure kinematic point of view the creeping section is partially locked. This result confirms our approach and will leads us to explore more creeping faults in Northern California in the future.

References

Aktug, B., et al. (2009), Deformation of western turkey from a combination of permanent and campaign gps data: Limits to block-like behavior, *Journal of Geophysical Research: Solid Earth (1978–2012)*, *114*(B10).

Beeler, N. M., D. L. Lockner, and S. H. Hickman (2001), A simple stick-slip and creep-slip model for repeating earthquakes and its implication for microearthquakes at parkfield, *Bulletin of the Seismological Society of America*, *91*(6), 1797–1804, doi:10.1785/0120000096.

Ben-Zion, Y., J. R. Rice, and R. Dmowska (1993), Interaction of the san andreas fault creeping segment with adjacent great rupture zones and earthquake recurrence at parkfield, *Journal of Geophysical Research: Solid Earth (1978–2012)*, *98*(B2), 2135–2144.

Burgmann, R., D. Schmidt, R. M. Nadeau, M. D'Alessio, E. Fielding, D. Manaker, T. V. Mcevilly, and M. H. Murray (2000), Earthquake potential along the northern hayward fault, california, *Science*, *289*(5482), 1178–1182, doi:10.1126/science.289.5482.1178.

Crowell, B., Y. Bock, D. T. Sandwell, and Y. Fialko (2013), Geodetic investigation into the deformational makeup of the salton trough, *Journal of Geophysical Research: Solid Earth*, *submitted*.

Field, E. H., et al. (2009), Uniform california earthquake rupture forecast, version 2 (ucerf 2), *Bulletin of the Seismological Society of America*, *99*(4), 2053–2107.

Freed, A. M., S. T. Ali, and R. Burgmann (2007), Evolution of stress in southern california for the past 200 years from coseismic, postseismic and interseismic stress changes, *Geophysical Journal International*, *169*(3), 1164–1179, doi:10.1111/j.1365-246X.2007.03391.x.

Freymueller, J. T., M. H. Murray, P. Segall, and D. Castillo (1999), Kinematics of the pacific-north america plate boundary zone, northern california, *Journal of Geophysical Research: Solid Earth (1978–2012)*, *104*(B4), 7419–7441.

Fuis, G. S., D. S. Scheirer, V. E. Langenheim, and M. D. Kohler (2012), A new perspective on the geometry of the san andreas fault in southern california and its relationship to lithospheric structure, *Bulletin of the Seismological Society of America*, *102*(1), 236–251.

Funning, G. J., R. Burgmann, A. Ferretti, F. Novali, and A. Fumagalli (2007), Creep on the rodgers creek fault, northern san francisco bay area from a 10 year ps-insar dataset, *Geophysical Research Letters*, *34*(19), doi:10.1029/2007GL030836.

Hearn, E. H., R. Bürgmann, and R. E. Reilinger (2002), Dynamics of izmit earthquake postseismic deformation and loading of the düzce earthquake hypocenter, *Bulletin of the Seismological Society of America*, *92*(1), 172–193.

Johanson, I. A., and R. Burgmann (2005), Creep and quakes on the northern transition zone of the san andreas fault from gps and insar data, *Geophysical Research Letters*, *32*(14), doi:10.1029/2005GL023150.

Lin, G., C. H. Thurber, H. Zhang, E. Hauksson, P. M. Shearer, F. Waldhauser, T. M. Brocher, and J. Hardebeck (2010), A california statewide three-dimensional seismic velocity model from both absolute and differential times, *Bulletin of the Seismological Society of America*, *100*(1), 225–240.

Lindsey, E., and Y. Fialko (2013), Geodetic slip rates in the southern san andreas fault system: Effects of elastic heterogeneity and fault geometry, *Journal of Geophysical Research: Solid Earth*.

Lisowski, M., J. Savage, and W. Prescott (1991), The velocity field along the san andreas fault in central and southern california, *Journal of Geophysical Research: Solid Earth (1978–2012)*, *96*(B5), 8369–8389.

Mccaffrey, R. (2005), Block kinematics of the pacific-north america plate boundary in the southwestern united states from inversion of gps, seismological, and geologic data, *Journal of Geophysical Research-Solid Earth*, *110*(B07401), doi:10.1029/2004jb003307.

Meade, B. J., and B. H. Hager (2005), Spatial localization of moment deficits in southern california, *Journal of Geophysical Research-Solid Earth*, *110*(B4), B04,402, doi:10.1029/2004JB003331.

Moore, D. E., and M. J. Rymer (2007), Talc-bearing serpentinite and the creeping section of the san andreas fault, *Nature*, *448*(7155), 795–797.

Nur, A., and G. Mavko (1974), Postseismic viscoelastic rebound, *Science*, *183*(4121), 204–206.

Pollitz, F. F. (2001), Viscoelastic shear zone model of a strike-slip earthquake cycle, *Journal of Geophysical Research*, *106*(B11), 26,541–26.

Rolandone, F., R. Burgmann, D. C. Agnew, I. A. Johanson, D. C. Templeton, M. A. D'alessio, S. J. Titus, C. Demets, and B. Tikoff (2008), Aseismic slip and fault-normal strain along the central creeping section of the san andreas fault, *Geophysical Research Letters*, *35*(14), doi:10.1029/2008GL034437.

Ryder, I., and R. Burgmann (2008), Spatial variations in slip deficit on the central san andreas fault from insar, *Geophysical Journal International*, *175*(3), 837–852, doi:10.1111/j.1365-246X.2008.03938.x.

Savage, J., and W. Prescott (1978), Asthenosphere readjustment and the earthquake cycle, *Journal of Geophysical Research: Solid Earth (1978–2012)*, *83*(B7), 3369–3376.

Savage, J. C., R. W. Simpson, and M. H. Murray (1998), Strain accumulation rates in the san francisco bay area, 1972-1989, *Journal of Geophysical Research-Solid Earth*, *103*(B8), 18,039–18,051, doi:10.1029/98JB01574.

Schmalzle, G., T. Dixon, R. Malservisi, and R. Govers (2006), Strain accumulation across the carrizo segment of the san andreas fault, california: Impact of laterally varying crustal properties, *Journal of Geophysical Research: Solid Earth (1978–2012)*, *111*(B5).

Shen, Z.-K., R. King, D. Agnew, M. Wang, T. Herring, D. Dong, and P. Fang (2011), A unified analysis of crustal motion in southern california, 1970–2004: The scec crustal motion map, *Journal of Geophysical Research: Solid Earth (1978–2012)*, *116*(B11).

Smith, B. R., and D. T. Sandwell (2006), A model of the earthquake cycle along the san andreas fault system for the past 1000 years, *Journal of Geophysical Research-Solid Earth*, *111*(B1), B01,405, doi:10.1029/2005JB003703.

Smith-Konter, B., and D. Sandwell (2009), Stress evolution of the san andreas fault system: Recurrence interval versus locking depth, *Geophysical Research Letters*, *36*(L13304), doi:10.1029/2009GL037235.

Smith-Konter, B. R., D. T. Sandwell, and P. Shearer (2011), Locking depths estimated from geodesy and seismology along the san andreas fault system: Implications for seismic moment release, *Journal of Geophysical Research: Solid Earth (1978–2012)*, *116*(B6).

Takeuchi, C. S., and Y. Fialko (2012), Dynamic models of interseismic deformation and stress transfer from plate motion to continental transform faults, *Journal of Geophysical Research: Solid Earth (1978–2012)*, *117*(B5).

Thatcher, W. (2007), Microplate model for the present-day deformation of tibet, *Journal of Geophysical Research: Solid Earth (1978–2012)*, *112*(B1).

Titus, S. J., C. Demets, and B. Tikoff (2006), Thirty-five-year creep rates for the creeping segment of the san andreas fault and the effects of the 2004 parkfield earthquake: Constraints from alignment arrays, continuous global positioning system, and creepmeters, *Bulletin of the Seismological Society of America*, *96*(4), S250–S268, doi:10.1785/0120050811.

Tong, X., D. Sandwell, and B. Smith-Konter (2013), High-resolution interseismic velocity data along the san andreas fault from gps and insar, *J. Geophys. Res. Solid Earth*, *118*, doi:10.1029/2012JB009442.

Wang, R., F. L. Martın, and F. Roth (2003), Computation of deformation induced by earthquakes in a multi-layered elastic crust—fortran programs edgrn/edcmp, *Computers & Geosciences*, *29*(2), 195–207.

Watts, A. B. (2010), *Crust and Lithosphere Dynamics: Treatise on Geophysics*, vol. 6, Elsevier.

Wdowinski, S., B. Smith-Konter, Y. Bock, and D. Sandwell (2007), Diffuse interseismic deformation across the pacific–north america plate boundary, *Geology*, *35*(4), 311–314.

Zeng, Y., and Z.-K. Shen (2010), A kinematic fault network model of crustal deformation for california and its application to the seismic hazard analysis, *Tech. rep.*, U.S. Geological Survey.

Appendix A

ScanSAR to ScanSAR interferometry

The systematic observation strategy of ALOS PALSAR provides strip-mode SAR imagery along every ascending orbital track and ScanSAR imagery along every third descending orbital track. Therefore to obtain a second look direction of PALSAR interferometry usually requires processing ScanSAR to ScanSAR mode interferograms. Since this mode of processing is rather new for ALOS, and there are few examples, we provide an overview of the method used to compute the interferogram shown in Figure 2.3 and Figure 3.1. The method is based on the proposal by *Bamler and Eineder* (1996) that, with proper pre-processing, standard strip-mode software can be used to construct phase-preserving SAR images and ultimately interferograms. The main advantage of using the standard strip-mode approach, instead of the traditional SPECAN approach (*Sack et al.*, 1985), is that existing and well tested, strip-mode InSAR processing software can be used. The main disadvantage of this approach is that the zero-padding between the bursts wastes considerable disk space and computer time. Nevertheless the two approaches should provide equivalent results.

Our preprocessor was developed and tested using data along a descending orbital track (T538) over southern California. This track contains two permanently installed radar corner reflectors that are used by JAXA to provide radiometric and geometric calibration for ALOS for the lifetime of the mission. JAXA has

collect PALSAR data over these reflectors in a variety of modes on both ascending and descending tracks. In a previous study (*Sandwell et al.*, 2008) we used the data along the ascending orbit T213 to develop a preprocessor for strip-mode interferometry including FBD to FBS interfrometry. In addition we examined the noise characteristics of all combinations of FBD and FBS strip-mode interferometry and compared this noise with C-band interferometry. Our main conclusion was that although the wavelength of PALSAR is 4 times longer than ERS, the rms of the phase noise in terms of line-of-sight displacement is only 1.6 times worse (3.3 mm versus 2.1 mm). In both cases the atmospheric contribution to the phase noise dominates.

Here we extend the ALOS preprocessing software to first perform ScanSAR to FBD mode interferometry and second to perform the more challenging ScanSAR to ScanSAR interferometry where a significant burst overlap is needed. Indeed both luck and accuracy are required to achieve a full swath-width ScanSAR to ScanSAR interferogram. The ScanSAR acquisition geometry and parameters for PALSAR are provided in Figure A1 and Table A1. The 5 subswaths cover an area $\sim$ 350 km wide. Following *Bamler and Eineder* (1996) the ScanSAR data are zero-padded to construct swath type data. The original WB1 file contains the burst of all 5 sub-swaths as consecutive rows. The preprocessor separates the data into 5 separate files where missing lines between the bursts are filled with zeros. Zeros are also added to the end of each echo to match the length of a standard FBD data file. In addition, the first 12 lines of each burst are zero-padded because these data are incorrect [Masanobu Shimada, personal communication, 2008]. Since the subswaths are processed independently and their amplitude and interferometric phase are recombined in the latitude-longitude co-ordinate system, an accurate geometric model, precise orbit, and consistent set of processing parameters is required to achieve a seamless recombination. The pre-processing code is rather complex because the pulse repetition frequency (PRF) of the PALSAR echoes varies in three ways. First as shown in Table A1, each sub-swath has its own PRF optimized to reduce crosstalk. Second, the PRF can change along the satellite track on any one of the sub-swaths. A PRF change on any sub-swath changes the time interval and

number of zero-pad lines needed on all the other sub swaths. Finally, when considering reference and repeat images for interferometry, the PRFs on a matching sub-swath can be different causing the burst alignment to change along the swath as we find in the example below. In addition each sub-swath has its own rear range which, varies along the track so rows must be shifted to align the rear range to the common prescribed value. Any small error in the preprocessing could result in a poorly focused image and/or low interferometric coherence.

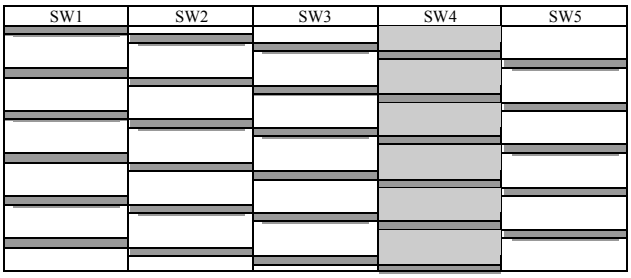

Figure A.1: Pattern of bursts for the 5 sub swaths of PALSAR in WB1 mode. Sub swath 4 corresponds to the nominal FBD and FBS strip-mode imagery.

Table A.1: Nominal radar parameters for each sub swath. The number of echoes in a burst *nburst* is the only fixed parameter.

	SW1	SW2	SW3	SW4	SW5
near range (m)	730097	770120	806544	848515	878195
PRF (Hz)	1692	2370	1715	2160	1916
nburst	247	356	274	355	327
D_t (s)	0.146	0.150	0.160	0.164	0.171
nsamples	4976	4720	5376	4432	4688
off nadir ($\circ$)	20.1	26.1	30.6	34.1	36.5

The first step in the software development was to focus the raw sub-swath data to form seamless amplitude imagery. We found that the best image quality (i.e. minimal scalloping) was achieved by setting the length of the synthetic

aperture to be exactly 6 bursts. This corresponds to setting the time ($\sim$ 4.7 s) and along-track distance of synthetic aperture to be exactly the same for each sub swath. We have found that by processing the SAR image to zero Doppler, the position of the radar corner reflectors in the image matches the position predicted from the orbit (zero range rate) to within 1 pixel in range and 4 pixels in azimuth. This good match provided confidence that the code is geometrically accuracy.

The second step in the software development was to construct ScanSAR to swath mode interferometry. This combination should always provide interference fringes because there is 100% overlap between the sparse bursts of the ScanSAR and the complete coverage of the swath (*Ortiz and Zebker*, 2007). The ALOS track 538 over Los Angeles has two FBD acquisitions and 3 ScanSAR WB1 acquisitions. The swath of the FBD data (34.3 incidence angle) overlaps with sub-swath 4 of the WB1 data. We experimented with three interferometric mode combinations, FBD to FBD, FBD to ScanSAR, and ScanSAR to ScanSAR. The FBD to FBD interferogram had a 10 m baseline and 46 day time span resulting in excellent overall coherence (*Zebker and Villasenor*, 1992) of 0.67. The FBD to ScanSAR interferogram had a somewhat longer baseline 121 m and 181 day time span resulting in a rather low average coherence of 0.24. An additional reason for the low coherence is that, because of limitations in our software, we did not zero the rows in the raw FBD swath data that were aligned with the zero-padded rows in the ScanSAR data (*Ortiz and Zebker*, 2007).

The third step in the software development was to construct ScanSAR to ScanSAR interferometry. The major issue here is that there is only a 20% chance of having along-track alignment of the bursts between reference and repeat orbits. There is a question of how much overlap of the bursts is needed to obtain interpretable interference fringes. We were very fortunate that two of the ScanSAR images along track 538 have significant burst overlap (up to 78%) and a moderate baseline of 450 m. An interesting aspect of this interferometric pair is that they have different PRF. This produces a gradual change in burst alignment along the track from 78% at the start of the acquisition to 0% overlap after 18 bursts. The phase and coherence of sub-swath 4 of this interferogram are shown in Figure

A2. Phase recovery and coherence are best at the top of the swath and gradually worsen toward the bottom. A plot of row-averaged coherence versus first overlap fraction (Figure A2c) illustrates that a maximum coherence of about 0.35 occurs where the burst overlap is greater than 50%. The coherences diminish to below 0.2 at a burst overlap of 18%. The results show that good interfrometric results can be achieved when the burst overlap is greater than about 50%. Assuming there is no control on the burst alignment of reference and repeat images there is a 1 in 5 chance of this occurring from any two ScanSAR images. We apply probability theory to show that 5 repeat SAR images will be needed to have a 90% chance of getting half burst overlap for at least one pair interferogram (Table A2). One successful alignment with half burst is called an event, of which the probability is 20%. We know these events are independent but not disjoint with each other. The probability for multiple SAR images can be generalized with calculation on probability of the union.

Table A.2: The probability analysis on getting half burst alignment.

Number of SAR images	Number of interferometry pairs	Probability of getting at least one pair with half burst alignment
2	1	0.2
3	3	0.488
4	6	0.7379
5	10	0.8926
6	15	0.9648
7	21	0.9908
8	28	0.9981

In the case of the track 124 spanning the Wenchuan earthquake there are 7 ScanSAR acquisitions. We were very fortunate that there is 80% burst alignment between the reference and repeat images most closely bracketing the earthquake (Figure 2.3). The time interval of this pair is 138 days and the baseline is rather

long (657 $\sim$ 844 m for perpendicular baseline) so removal of topographic phase was problematic, especially in the mountainous areas. The program used to pre-process the WB1 data into pseudo-strip-mode data is available as part of an ALOS pre-processing package available at `http://www-rohan.sdsu.edu/~mellors`.

References

Bamler, R., and M. Eineder (1996), ScanSAR processing using standard high precision SAR algorithms, *IEEE Transactions on Geoscience and Remote Sensing*, *34*(1), 212–218.

Ortiz, B., and H. Zebker (2007), ScanSAR-to-stripmap mode interferometry processing using ENVISAT/ASAR data, *IEEE Transactions on Geoscience and Remote Sensing*, *45*(11).

Sack, M., M. Ito, and I. Cumming (1985), Application of efficient linear fm matched filtering algorithms to synthetic aperture radar processing, *IEE Proceedings (Communications, Radar and Signal Processing)*, vol. 132, pp. 45–57, IET.

Sandwell, D. T., D. Myer, R. Mellors, M. Shimada, B. Brooks, and J. Foster (2008), Accuracy and resolution of ALOS interferometry: Vector deformation maps of the Father's day intrusion at Kilauea, *IEEE Transactions on Geoscience and Remote Sensing*, *46*(11), 3524–3534.

Zebker, H. A., and J. Villasenor (1992), Decorrelation in interferometric radar echoes, *IEEE Transactions on Geoscience and Remote Sensing*, *30*(5), 950–959.

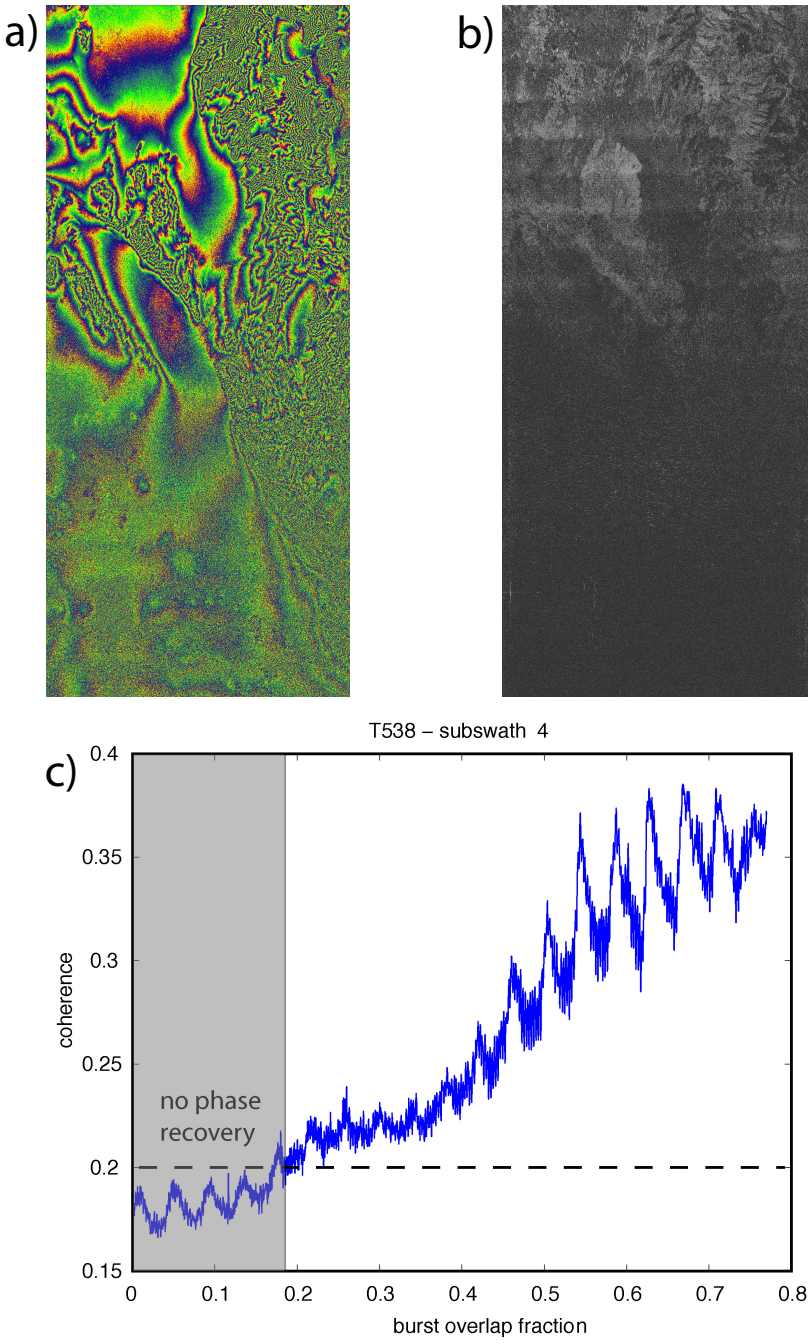

Figure A.2: ScanSAR to ScanSAR interferogram for subswath 4 of track 538 across the Los Angeles basin. The perpendicular baseline is 450 m and the time interval is 92 days. No topographic phase has been removed. (a) interferometric phase is high at top of swath where burst overlap is large and lower toward the bottom. (b) coherence also decreases from top to bottom as burst overlap decreases. (c) row-averaged coherence versus burst overlap.